HYBRID IMPROPER FERROELECTRICITY AND MAGNETOELECTRIC EFFECTS IN COMPLEX OXIDES

BY YAZHONG WANG

A dissertation submitted to the

School of Graduate Studies

Rutgers, The State University of New Jersey

in partial fulfillment of the requirements

for the degree of

Doctor of Philosophy

Graduate Program in Physics and Astronomy

Written under the direction of

Sang-Wook Cheong

and approved by

_____

_____

_____

_____

_____

New Brunswick, New Jersey

May, 2018

ABSTRACT OF THE DISSERTATION

Hybrid improper ferroelectricity and magnetoelectric effects in complex oxides

by Yazhong Wang

Dissertation Director: Sang-Wook Cheong

This thesis contains several investigations of ferroelectricity and magnetoelectric effects in complex oxides. We start by reviewing the history and mechanisms of ferroelectricity and multiferroics, then give a brief introduction to proper ferroelectricity, improper ferroelectricity, hybrid improper ferroelectricity and polar magnets. In the hybrid improper ferroelectricity section, several major systems are explained in detail including $(AA')B_2O_6$ double perovskites, $(ABO_3)_2/AO$ Ruddlesden-Popper (RP) phase and $A'(AB_2O_7)$ Dion-Jacobson (DJ) phase. Next, our investigations are divided into two parts. The first half focuses on the study of ferroelectricity and domain wall (ferroelectric vs. ferroelastic, charged vs. noncharged) motion in $Sr_3Sn_2O_7$ system (n=2, RP phase). We discover that layered $Sr_3Sn_2O_7$ exhibits switchable polarization at room temperature, demonstrating that $Sr_3Sn_2O_7$ is the first room-temperature insulating ferroelectric containing Sn^{4+}. The in situ poling results on $Sr_3Sn_2O_7$ using focused electron beams in transmission electron microscopy unveil the intriguing ferroelectric domain switching kinetics: ferroelectric noncharged domain walls move fast while ferroelectric charged domain walls do not move, probably due to octahedral rotation switching is easier along the $c-axis$. Furthermore, due to small coercivity, we could erase (shrink) and re-generate (expand) orthorhombic twin domains using different direction strains. The corresponding ferroelectric-ferroelastic domain patterns are observed

under transmission polarized optical microscope (TPOM) and in-plane piezo-response force microscope (IP-PFM). These discoveries reveal the rich scientific nature of the Sn-containing ferroelectric and provide potential application opportunities of it. In the second half of the thesis, we focus on the study of $M_2Mo_3O_8$ (M=Fe, Mn, Zn, Ni, Co) polar magnets. In polar magnets, the absence of poling requirements due to the polar nature makes possible utilization of giant ME coefficients as necessary for applications. Our works unveil the magnetic properties and the ME coupling inside this system, especially the largest ME coefficient in $Fe_2Mo_3O_8$ among all discovered polar magnets and the in-plane magnetic ordering in $Ni_2Mo_3O_8$ for the first time. In $Fe_2Mo_3O_8$, hidden ferrimagnetism of the Fe-O layers strongly enhances the magnetic response in the transition field, providing an explanation for the observed giant differential ME coefficients. Our results demonstrate the promise of polar magnets as ME system and indicate that their functional properties could be further enhanced by presence of a local ("hidden") magnetic moment that can be easily converted to macroscopic magnetization by an applied field.

Acknowledgements

I just do not realize it has been six years since I came to Rutgers. The memory of my excitation and all kinds of imagination of the future on the way from Newark airport to Rutgers in 2012 is still fresh in my mind. On the other hand, lots of changes, including new buildings on Bush campus and many friends' leaving for graduation, keep reminding me the passage of time. There are many people in my mind that I want to acknowledge.

First and foremost, I would like to express the deepest appreciation to my advisor professor Sang-Wook Cheong for his enthusiasm and continuous inspiration and support on my way pursuing the Ph.D.. The first time I met him was on a workshop in South Korea during my internship at POSTECH when I was a junior student. I was attracted by his broad knowledge and keen sense of science. It has been such an honor for me to be his Ph.D. student. His rigorous, gentle, modest and scrupulous attitude guided me from every aspect about how to be a physicist and a respectful person. I have learned and benefited more than I could ever imagine from him.

A special thank you is owed to my committee members, professor Karin M. Rabe, professor Saurabh W. Jha, professor Frank Zimmermann and professor Trevor A. Tyson. Their advises and active feedback guided me through my research toward this thesis. I also owe the sincere gratitude to professor Weida Wu, professor Valery Kiryukhin, professor Andrei Sirenko and professor Sang-Hyuk Lee for all the valuable discussions and help.

In addition, my heartfelt thanks go to Yoon Seok Oh for all the techniques and prudent attitude I learned from him. I also express my thanks to former and current group members: Yoichi Horibe, Namjung Hur, Choongjae Won, Hee Taek Yi, Seung Chul Chae, Fei-ting Huang, Rongwei Hu, Kai Du, Seong Joon Lim, Jae Wook Kim, Junjie Yang, Xuan Luo, Lunyong Zhang, Xueyun Wang, Bin Gao, Xiaochen Fang, Xianghan Xu, Alemayehu Solomon Admasu, Wei Cai, Fei Fan, Yue Liu, Yanbin Li, Meixia Wu, David Fan and Brian

Wesley Casas. I benefit a lot from the discussions and enjoyable time with them. I would also like to thank my colleagues, Lucian Pascut, Jixia Dai, Wenbo Wang, Yuanjun Zhou, Can Xu, Wei Dai, Qiang Han, Chen Chen, Wenhan Zhang, Wenyuan Zhang, He Chen and Ming Huang for the joyful moments. My special thanks also go to Yanan Geng, Yi Zhang and Yuanzhen Chen for all the advices and help to my career.

Last but not least, I sincerely express my loving thanks to my wife Yuanqi Wang, who has always been encouraging and believing in me. I could not imagine how my life will be without her. I also want to thank my parents and parents in law for all the loves and supports. Without them, this dissertation would not have been possible.

Dedication

To my parents for their endless love and support

Table of Contents

Abstract . . . ii

Acknowledgements . . . iv

Dedication . . . vi

List of Tables . . . x

List of Figures . . . xi

1. Prologue . . . 1

1.1. Ferroelectricity and multiferroicity . . . 1

1.2. Proper and improper ferroelectricity . . . 4

1.3. Hybrid improper ferroelectricity . . . 7

1.3.1. Introduction . . . 7

1.3.2. Antiferroelectric ABO_3 perovskite with octahedral rotations . . . 7

1.3.3. Ferroelectric $(AA')B_2O_6$ double perovskites . . . 11

1.3.4. Ferroelectric $(ABO_3)_2/AO$ Ruddlesden-Popper phase . . . 13

1.3.5. Ferroelectric $A'(AB_2O_7)$ Dion-Jacobson phase . . . 14

1.4. Polar magnets . . . 15

2. First room temperature ferroelectric Sn insulator ($Sr_3Sn_2O_7$; n=2 RP phase) and its polarization switching kinetics . . . 17

2.1. Introduction: importance of finding ferroelectric Sn materials . . . 17

2.2. Debate on the ground state of $Sr_3Sn_2O_7$ . . . 18

2.3. Sample Growth and XRD results . . . 20

2.4. Ferroelastic twin structure . . . 21

2.5. Unveiling ferroelectricity from $P(E)$ loop and TEM images . . . 22

2.6. Direct observation of domain wall movement in electric field 25
2.7. The polarization switching kinetics and 3D FE domain configuration 27
2.8. Summary and outlook 27

3. Tunable ferroelastic domain walls in $Sr_3Sn_2O_7$ single crystals with low coercivity 30
3.1. Introduction 30
3.2. Crystal growth 31
3.3. Polarization hysteresis loop with small coercive field 33
3.4. Tunable ferroelastic domain walls under stress 34
3.5. Ferroelectric domain patterns and charged domain walls 36
3.6. Summary and outlook 40

4. Polar magnets: $M_2Mo_3O_8$ (M=Fe, Mn, Ni, Co, Zn) 41
4.1. Introduction 41
4.2. Crystal structure and sample growth 42
4.3. Hidden ferrimagnetism and giant magnetoelectricity in $Fe_2Mo_3O_8$ 44
4.3.1. Antiferromagnetic ground state 46
4.3.2. Structural transition associated with the magnetic order 46
4.3.3. Magnetically-induced electric polarization and metamagnetic transition 49
4.3.4. Magnetoelectric effect and the associated ionic shifts 49
4.3.5. Reproducible magnetoelectric control of the electric polarization and magnetization 53
4.4. Ferromagnetism in $(Fe, Zn)_2Mo_3O_8$ 55
4.5. Ferrimagnetism in $Mn_2Mo_3O_8$ 58
4.6. Antiferromagnetism in $Co_2Mo_3O_8$ 59
4.7. Antiferromagnetism in $Ni_2Mo_3O_8$ 62
4.8. Summary and outlook 64

5. Epilogue 67

5.1. Review of results 67
5.2. Future research 69

Appendix A. Measurement Method 70
A.1. Dielectric properties 70
A.2. Polarization hysteresis loop 70
A.3. Magnetic properties 71

Appendix B. First principles calculation 74

List of Tables

1.1. Classification of ferroelectrics, which is from reference [1]. 6

2.1. The refinement result of $Sr_3Sn_2O_7$ using the structural model of $A2_1am$ (# 36), obtained using powder XRD. Amam structural adopts from reference [2]. 20

2.2. The refinement result of $Sr_3Sn_2O_7$ using the structural model of $Amam$ (# 63), obtained using powder XRD. Amam structural adopts from reference [2]. 21

4.1. a- and c- lattice constants in $M_2Mo_3O_8$. All distances in Å. 42

4.2. Calculated ionic shifts (in Å) for the paramagnetic to AFM transition (2^{nd} column), and for the AFM to FRM transition (3^{rd} column). See Figure 4.7 for atomic labeling. Error bars reflect the impact of the multiple low-energy solutions characteristic to the GGA-PBE+U method. This table is from reference [3] 52

List of Figures

1.1. **Classification of 32 crystal point groups.** 2

1.2. **History of multiferroics and magnetoelectric effect.** Number of papers per year on magnetoelectric effect and multiferroics. 3

1.3. **Crystal structure and behavior of energy of $PbTiO_3$, a archetypal proper ferroelectric perovskite. This figure is from reference [4]** (a) Paraelectric $Pm\bar{3}m$ structure of $PbTiO_3$. (b) Ground state ferroelectric $P4mm$ structure of $PbTiO_3$. A displacement of the Ti and Pb cations against the oxygen anions gives rise to a spontaneous polarization and relates the ground state to the nonpolar $Pm\bar{3}m$ structure that $PbTiO_3$ is found in above $\sim$ 760 K. The cell also undergoes a spontaneous strain from cubic to tetragonal. (c) The behavior of the energy as a function of the polarization when the temperature, T, is above and below the Curie temperature (T_c) of the primary order parameter for a proper ferroelectric transition. 5

1.4. **Crystal structure and behavior of energy of $YMnO_3$, an improper ferroelectrics. This figure is from reference [4]** (a) Structure of the paraelectric phase of the improper ferroelectric $YMnO_3$. (b) Structure of the ferroelectric phase and direction of the polarization, P. (c) The behavior of the energy as a function of the polarization when the temperature, T, is above and below the Curie temperature (T_c) of the primary order parameter for an improper ferroelectric transition. 6

1.5. **The crystal structure and octahedral distortion in ABO_3 perovskite oxides, which is from reference [5]** (a) The crystal structure of ABO_3 perovskite oxide in $Pm\bar{3}m$ (cubic) phase. (b) The same structure as in (a) but showing the BO_6 octahedral network. (c) Schematic illustration of the $a^0b^+b^+$ structure, indicating the adjacent octahedrons in the same plane rotate in opposite sense to maintain corner connectivity. (d, e) Schematic illustration of the $a^0a^0c^+$ and $a^0a^0c^-$ rotation patterns. The in-phase rotations and out-of-phase rotations of the octahedron about the z-axis are discernible in (d) and (e), respectively. (Note that for clarity the A-site cations and the oxygen atoms are omitted from panels (c-e)). 8

1.6. **Energies (in meV/f.u.) of different phases of $SrZrO_3$ after full structural relaxations in comparison to that of the cubic phase taken as reference, which is from reference [6]**. One formula unit (f.u.) consists in a five-atom ABO_3 unit. Arrows indicate the type of additional title component (R_5^- or M_3^+) appearing from one structure to another. Glazer's notations clarity along which direction this tilt component appears. 9

1.7. **Three different normal modes in $Pnma$ structure. This figure is from Reference [7]**. (a) Octahedral rotation about [001]. (b) Rotation about [110] with A-site displacement (c) Antipolar A-site displacement without rotation 9

1.8. **Octahedral rotations induced atom movements in the AO layer**. The red dots indicate the A-site cation, while other color dots refer to the position of oxygen atoms, which lay on the same layer with A-cite cation, after different lattice distortions. (a) Black dots represent the position of oxygen when there is no tilting. They move to the pink position when each BO_6 octahedron rotates under $a^-a^0a^0$ mode. They continue moving to blue positions when each B_6 octahedron rotates in $a^-a^-a^0$ mode. (b) Red arrows indicate the moving direction of A-site cation resulting from the symmetry breaking. (c) Gray dots denote the final position of oxygen after all $a^-a^-c^+$ rotation. (d) Black arrows indicate another moving of the A-site cation after the BO_6 octahedron's rotation along the [001] direction. 10

1.9. **The intralayer polarization of (a) $LaGaO_3$ and (b) $YGaO_3$ in the $Pnma$ ground state.** The right of each figure represents the amplitude of the layer-resolved polarization from first-principles calculations. These figures are taken from reference [7] 11

1.10. **Net electric polarization in $(A/A')B_2O_6$ double perovskites** (a) In $(A/A')B_2O_6$, cation ordering lifts the inversion centers on the B-site, which supports the form of hybrid improper ferroelectricity. (b) In $A_2(B/B')_2O_6$, net polarization is still zero due to the same amplitude and opposite direction intralayer polarization in the nearby AO layers. (c) Intralayer polarization in $LaYGa_2O_6$ from first principles calculation. Figures are taken from reference [7]. 12

1.11. **Polarization hysteresis loop of 3/3 PTO/STO superlattice** (a) Schematic of the 3/3 PTO/STO superlattice structure. (b) Polarization vs. electric field hysteresis loop. (c) Current as a function of time for different sequences in the PUND measurements. Figures are taken from reference [8]. 13

1.12. **Schematic structure of $(ABO_3)_nAO$ RP phase and calculated polarization in $(CaMnO_3)_2CaO$.** (a) Crystal Structure of $(ABO_3)_nAO$, n=1, 2, 3. (b) Intralayer polarization in $(CaMnO_3)_2CaO$ from first principles calculation. Figures are from reference [7] and [9]. 14

1.13. **Crystallographic structure and intralayer polarization of $RbBiNb_2O_7$.** Top view (a) and side view (b) of the polar displacement from each cation shown by arrows. (c) Estimated intralayer polarization from first principles calculations. Figures are from reference [10]. 15

2.1. **The proposed ferroelectric $a^-a^-c^+$ distortions and intralayer polarization in $Sr_3Sn_2O_7$.** (a) The c-direction view. (b) The b-direction view. The blue and green arrows indicate the Sr displacements along the a-direction. 18

2.2. **X-ray powder diffraction pattern of $Sr_3Sn_2O_7$ at 285 K.** Crosses represent experimental data points. The calculated ($A2_1am$) and difference intensities are shown as red, and green ($A2_1am$)/ blue ($Amam$) curves, respectively. The two sets of vertical bars indicate the Bragg conditions for $A2_1am$ (green) and $Amam$ (blue) space groups. 19

2.3. **Orthorhombic twin domains in $Sr_3Sn_2O_7$.** (a) and (b) are both POM images of the polished surface of a polycrystalline of $Sr_3Sn_2O_7$ specimen in a transmission mode. The white bar with P (A) represents the direction of the polarizer (analyzer). 22

2.4. **Ferroelectric domains and domain wall motion with focused electron beam-induced poling in $Sr_3Sn_2O_7$.** (a) An $a-b$ plane DF-TEM image taken using the superlattice $g+ = (120)$ spot. (b) A DF-TEM image taken using the superlattice $g- = (\bar{1}\bar{2}0)$ spot. The reversed contrast in (a,b), especially near the yellow square dotted line demonstrates the presence of ferroelectric 180° domains, consistent with the $A2_1am$ space group. The electron diffraction patterns in twin A and twin B are shown by the inserts of (a) and (b), respectively. (c, d) The evolution of these ferroelectric domains under focused electron beam-induced poling. The black arrows in (c, d) depict the poling electric field induced by the focused electron beam. The yellow square dotted lines in (a)-(d) indicate the original position of FE 180° DW. A new dark circular spot around the yellow square dotted line is due to the surface damage by the focused electron beam. 23

2.5. **Polarization hysteresis loop of $Sr_3Sn_2O_7$ at 285 K.** Electric polarization (P) and compensated current (I) versus electric field (E) hysteresis loop of a polycrystalline $Sr_3Sn_2O_7$ specimen, measured with a PUND method in oil at frequency $f = 270.27HZ$. 24

2.6. **Polarization hysteresis loops of polycrystalline $Sr_3Sn_2O_7$ measured at room temperature.** (a) In different electric fields. (b) At different frequencies. 25

2.7. **Direct observation of domain wall movement in $Sr_3Sn_2O_7$.** (a) DF-TEM image taken in the $a-c$ plane of $Sr_3Sn_2O_7$. With a focused electron beam, an in-plane electric field is induced as shown by the black arrow with a white edge. (b-e) DF-TEM images taken 0, 5.4, 10.8 and 16.2 s after removing the focused electron beam, respectively. (f) Final state after all the induced charges dissipate away. Purple (blue) dotted line depicts a FE charged DW (FE noncharged DW). Green solid line indicates a disordered region. 26

2.8. **Octahedral tilting distortions across different FE walls and the speed of FE wall moving.** (a) Octahedral tilting across the FE CDW(purple dotted line) and the FE NCW (blue dotted line). The red arrows indicate the bulk polarization in each domain. (b) Displacements of a FE CDW and 2 FE NDWs in Figure 2.7 (b-f) as a function of time after the focused beam was removed. 28

2.9. **A schematic diagram of the 3D FE domain configuration.** 28

3.1. **A photograph of the as-grown $Sr_3Sn_2O_7$ single crystal boule.** . . . 32

3.2. **Switchable electric polarization at room temperature with smallest coercive field among all HIF bulk materials.** (a,b) The $c-direction$ and $b-direction$ views of the ferroelectric $a^-a^-c^+$ distortions in $Sr_3Sn_2O_7$. The green and blue arrows represent Sr antipolar displacements along the $a-axis$ in the perovskite block and rocksalt block, respectively. The red (grey) dots depict oxygen (Sn) atoms. (c, d) Electric polarization (P) and compensated current density (J) versus electric field (E) hysteresis loop of a $Sr_3Sn_2O_7$ single crystal, measured along two different crystallographic directions with a PUND method in oil at frequency $f = 270HZ$. The electric field was applied parallel (45°) with the twin boundaries for the measurement represented by the blue (red) curve. (e) High-temperature resistivity (ρ) as a function of temperature (T) measured using four-probe methods. The current was applied in the $a-b$ plane along the structural twin boundaries. The red (black) curve represents the data taken during the heating (cooling) process with a sweeping rate of $5°C/minute$. (f) The normalized $P(E)$ loops of $Sr_3Sn_2O_7$ single crystal (blue along [110] and red along [100]), $Ca_3Ti_2O_7$ single crystal (yellow, along [110]) and $Sr_3Sn_2O_7$ poly sample (black). . . . 35

3.3. **The derivative of $log(\rho(T))$ to T.** The $\rho(T)$ was shown in Figure 3.2 (e). The red (black) curve records the data during warming (cooling). The temperature sweeping rate is $5°/minute$. 36

3.4. **Erase and re-generate orthorhombic twins in $Sr_3Sn_2O_7$ single crystal.** (a) A schematic geometry of the experiment. One $a-b$ plane cleaved thin piece is polished into a square shape with boundaries along the crystal [100] ([010]) directions. (b-e) Transmission polarized optical microscope (TPOM) images of it. The dark-bright contrast in (b, d, e) indicates the orthorhombic twin domains. (b) is the initial state and (c-d) present the evolution of twin domains under two different direction uniaxial stress, as shown by the blue arrows in each figure. The colorful squares in (c-e) indicate the corresponding scanned regions, whose PFM images will be shown in Figure 3.5. In (b-e), the white bar with P (A) presents the direction of the polarizer (analyzer). (f) $a-b$ plane crystallographic cartons, the black dotted lines indicate the ferroelastic domain walls. The blue (green) arrows indicate the atom displacement in different domains. The dark yellow (light yellow) dotted lines indicate the longer (shorter) orthorhombic $a-axis$ ($b-axis$). 37

3.5. **Observation of ferroelectric-ferroelastic domains.** (a-b) In-plane piezoresponse force microscope (IP-PFM) images of the cleaved (001) surface of $Sr_3Sn_2O_7$ crystal at room temperature. Orthorhombic twin boundaries are oriented along the diagonal direction of the xy scanning axes. In (a) and (b), the long axis of the AFM cantilever is oriented along the horizontal and vertical direction respectively, as shown by the carton on the left bottom corner. (c) Illustration of polar domains in $80\mu m \times 80\mu m$ area, obtained from (a) and (b). The black and white arrows in (a-b) indicate the direction of the electric polarization inside each domain. 38

3.6. **Effect of stress on ferroelectric-ferroelastic domains and charged domain walls.** (a-c) TPOM images of the squared regions in Figure 3.5 (c-e). (e-g) The corresponding IP-PFM images with white and black arrows indicate the polarization direction in each domain. (h) A schematic picture depicts the density of bound charges of all the FA DWs and FE DWs in (g). For the FA DWs, there are found different DWs with three different charge density (0, $\pm\sqrt{2}P$) as shown by the top figure in (d). For FE DWs around the two island FE domains in (g), the charge density change continuously from $2P$ to $-2P$. The bottom picture in (d) depicts possible charge density of FE DWs with respect to the polarization direction (black arrows). The boundary color in (d) is consistent with the color bar in (h), representing the charge density from $2P$ to $-2P$. 39

4.1. **Crystal structure and optical images of $M_2Mo_3O_8$** (a) Crystal structure of $M_2Mo_3O_8$. Vertical lines connect the nearest M ions along the c axis (blue lines are longer than the red ones). (b) The Mo-O layer in the ab crystallographic plan. This Mo kagome-like layer is trimerized. The Mo trimers are in the singlet state. (c) The M-O layer in the ab crystallographic plane. Thick line depicts the largest M-M magnetic coupling J. (d) Optical image of a piece of $Fe_2Mo_3O_8$. The distance between the two lines on the ruler is 1mm. 43

4.2. **Magnetic susceptibility, heat capacitance and spin configuration of $Fe_2Mo_3O_8$, which is from rearrangement of figures in reference [3]** (a) Temperature dependence of DC magnetic susceptibility χ_{DC} in zero field-cooled (ZFC) and field-cooled (FC) processes along two crystallographic directions, parallel and perpendicular to the c axis, in $\mu_0 H$=0.2T. (b) Specific heat anomaly at the Neel temperature. Red line represents the double Debye model fit discussed in the text. Insert: the image of as-grown Fe_2Mo_3O8 single crystal. (c) The AFM order, together with the calculated largest ionic shifts associated with the paramagnetic to AFM transition. The direction of the magnetically-induced ΔP is shown with a thick arrow. (d) Schematic view of the AFM and FRM orders. Pink arrows represent the ferrimagnetic moments of the individual Fe-O layers. 45

4.3. **Dielectric $\varepsilon(T)$ and magnetic $\chi_{DC}(T)$ susceptibilities in the vicinity of T_N, which is from reference [3].** The magnetic susceptibility was measured on cooling in applied magnetic field H=0.2 T(blue line), and on subsequent warming in the same field (red line). 46

4.4. **Magnetically-induced electric polarization, and the metamagnetic transition, which is from reference [11].** (a) Temperature dependence of the c-axis dielectric constant $\varepsilon(T)$, f=44 kHZ. (b) Variation of the c-axis electric polarization ΔP with temperature. (c,d) Magnetic field dependence of magnetization $M(H)$ and polarization $\Delta P(H)$ at various temperatures. In (d), solid (open) circles depict the data obtained upon sweeping the magnetic field up (down). 47

4.5. **Pyroelectric current density, magneto-current, and the differential ME coefficient dP/dH at different temperatures, which are from the supplementary information of reference [3]** (a) Loss tangent as a function of temperature. (b) Pyroelectric current density as a function of temperature, measured upon warming. (c) Isothermal magnetocurrent as a function of magnetic field. (d) Differential magnetoelectric coefficient dP/dH calculated using the data shown in panel (c). Arrows indicate the field sweeping direction. All the measurements are along the crystallographic c axis. 48

4.6. **Magnetoelectric effect, and the associated ionic shifts, which is from reference [3].** (a,b) Magnetic field dependence of magnetization $M(H)$ and polarization $\Delta P(H)$ at $T = 55K$. Numbers and arrows indicate the measurement sequence. The insert in (b) shows the magnetic orders and the ferrimagnetic moments of the Fe-O layers for the phases involved. (c) The calculated ionic shifts for the paramagnetic to AFM transition. The thick arrow represents the corresponding change of the electric polarization, ΔP. (d) the same as (c), but for the AFM to FRM transition. 50

4.7. **Ionic Labels, which is from reference [3].** These labels are used in Table 4.2 51

4.8. **Reproducible magnetoelectric control of the electric polarization and magnetization with giant ME coefficients, which is from reference [3].** (a) Periodic modulation of electric polarization (blue) induced by a magnetic field linearly varying between 3.25 T and 3.5 T (black) at 55 K. (b) Periodic modulation of magnetization (green) induced by an electric field (red) linearly varying between ±16.6 KV/cm, for T=55 K and $\mu_0 H$=3.345 T. (c) Phase diagram of $Fe_2Mo_3O_8$. Black dots determined from $M(H)$, and red diamonds - from $\chi(T)$ curves. (d) Electric field dependence of magnetization for $Fe_2Mo_3O_8$ (from panel (b), averaged), and for Ni_3TeO_6 (×10). The insert illustrates the experimental setup, with directions of the applied fields shown. In all figures, the magnetization, polarization, and the applied fields are along the c axis. 54

4.9. **Reversal of the differential magnetoelectric coefficient in $Fe_2Mo_3O_8$ by changing the direction of the bias magnetic field, which is from the supplementary of reference [3].** (a) Periodic modulation of magnetization (green) induced by an electric field (red) linearly varying between ±16.6 KV/cm, for T= 55K and $\mu_0 H$=-3.345 T. These data differ from those shown in Figure 4.8(b) only by the direction of the applied magnetic field. Note the change of the sign of dM/dE. (b) Electric field dependence of magnetization for two opposite bias magnetic fields, +3.345 T, and -3.345 T. All the measurements are along the c axis. 55

4.10. **Magnetic properties of $(Fe_{1-x}Zn_x)_2Mo_3O_8$ (x=0.125, 0.25, 0.5) poly samples.** (a) Temperature dependence of DC magnetic susceptibility in zero field cooled process. (b) Magnetic field dependence of magnetization at 2K. 56

4.11. **Temperature dependence of DC magnetic susceptibility of $(Fe_{1-x}Zn_x)_2Mo_3O_8$ (x=0.07, 0.08, 0.09, 0.1) single crystals.** $\chi_{DC}(T)$ in zero field-cooled (ZFC) and field-cooled (FC) processes along the crystallographic c-axis of $(Fe_{1-x}Zn_x)_2Mo_3O_8$ (x=0.07 in (a), 0.08 in (b), 0.09 in (c), 0.1 in (d)) single crystals. All these measurements are done on hexagonal shape single crystals, similar to the one shown in Figure 4.2 (b). 57

4.12. **Magnetic field (H) dependence of magnetization (M) for $(Fe_{1-x}Zn_x)_2MO_3O_8$ (x=0.09 and 0.1) single crystals.** (a) $M(H)$ curves measured at 15 K and 51 K in a field along the $c-axis$ for x=0.09 single crystal. (b) Anisotropic $M(H)$ curves measured at 10 K and 20 K for x=0.1 single crystal. 58

4.13. **Magnetic and electric property of $Mn_2Mo_3O_8$ single crystal** (a) Temperature dependence of magnetization for $Mn_2Mo_3O_8$ in field H parallel and perpendicular to the c axis, respectively. (b) Magnetic field dependence of magnetization at 28 K in field parallel and perpendicular to the c axis, respectively. The insert of (b) is the zoom in view of the red curve. (c)The pyroelectric current density (J) and the integrated electric polarization (ΔP) as a function of temperature. The current was measured during warming along the $c-axis$ at a sweeping rate of 5K/min. 59

4.14. **Magnetic properties and the change of electric polarization of $Co_2Mo_3O_8$ single crystal.** (a) Temperature dependence of magnetization in field parallel and perpendicular to the $c-axis$ after zero field cooling process. (b) Magnetic field dependence of magnetization in field parallel to the $c-axis$ at 25 K, 36 K, 38 K and field perpendicular to the $c-axis$ at 36 K. 60

4.15. **The variance of DC magnetization as a function of temperature of $CoZnMo_3O_8$ single crystal in fields along two different directions, parallel and perpendicular to the $c-axis$.** 61

4.16. **Magnetic transitions in $(Ni,Zn)_2Mo_3O_8$ single crystals.** (a) Temperature dependence of DC magnetic susceptibility χ_{DC} in zero field-cooled (ZFC) process along two crystallographic directions, parallel and perpendicular to the $c-axis$. The insert is the zoom-in of the low temperature part. (b) Specific heat anomaly at the Neel temperature of $Ni_2Mo_3O_8$ single crystal. Red line represents the double Debye model fit. Insert: the data during warming and cooling around the transition. 63

4.17. **Temperature-induced electric polarization in $Ni_2Mo_3O_8$ single crystal.** (a, b) The measured pyroelectric current density and integrated change of polarization during warming after zero field cooling along two different directions, parallel and perpendicular to the $c-axis$. (c, d) Temperature dependence of the $c-axis$ dielectric constant $\epsilon(T)$ and loss tangent, $f = 44kHZ$. 63

4.18. **Metamagnetic transition and magnetically-induced electric polarization in $Ni_2Mo_3O_8$ at 2K.**Magnetic field dependence of magnetization ,$M(H)$ in (c) and $dM/dH(H)$ in (d), and electric polarization, $\Delta P(H)$ in (b) and $J(H)$ in (a). 64

4.19. **Metemagnetic transition and magnetically-induced electric polarization in $Ni_2Mo_3O_8$ at 4.5K.** Magnetic field dependence of pyroelectric current density in (a) and derivative of magnetization in (b). 65

A.1. **Logic 1 Loop Construction** Logic 1 Hysteresis Loop Construction: Response Contains Remanent + Non-Remanent Polarization Components . . 72

A.2. **Logic 0 Loop Construction** Logic 0 Hysteresis Loop Construction: Response Contains Only Non-Remanent Polarization Components 73

Chapter 1

Prologue

1.1 Ferroelectricity and multiferroicity

Ferroelectricity is a characteristic of certain materials that have a spontaneous electric polarization, which can be reversed by the application of an external electric field [12]. This reversibility of polarization makes ferroelectrics being a subgroup of the pyroelectrics. Out of a total of 32 crystal point groups, 21 are non-centrosymmetric *i.e.* crystals not having a center of symmetry. Out of these 21, 10 belong to polar *i.e.* crystals which possess a unique polar axis showing different properties at the two ends as shown in Figure 1.1. Polar crystals are also called pyroelectrics since they will act as an electric dipole during heating or cooling, in which the external or internal conduction often cannot yield enough current to compensate for the change of the dipole moment. The reversibility of polarization in ferroelectrics is a consequence of the fact that the polar structure of a ferroelectric is a slightly distorted non-polar structure.

Ferroelectricity, involving as it does the complex interplay of dielectric and elastic behavior in highly nonlinear, anisotropic, polarizable crystals, is perhaps even now almost as much an art as a science [13–16]. The first discovery of these unusual properties was reported in Rochelle salt by Pockels in Gottingen as early as 1894 [17]. After 1930 the interest in Rochelle Salt revived simulating research by a number of scientists in Russia, Switzerland, Great Britain, United States and Japan. From 1940 to 1950, the major experimental features of barium titanate were first studied and the capacitor and transducer applications for ceramic $BaTiO_3$ were firmly established [18]. In 1960, Cochran [19] and Anderson simultaneously and independently discovered the formulation of the elegant soft-mode description of the ferroelectric transition, which perhaps be the most significant theoretical development

Crystal class	Centro symmetric Point groups		Noncentrosymmetric Point groups				
			Polar		Non-polar		
Cubic	m3	m3m	none		432	$\bar{3}$ m	23
Tetragonal	4 or m	4 or mmm	4	4mm	$\bar{4}$	$\bar{4}$ 2 m	22
Orthorhombic	mmm		mm2		222		
Hexagonal	6 or m	6 or mmm	6	6mm	$\bar{6}$	$\bar{6}$2m	622
Trigonal	$\bar{3}$	$\bar{3}$ m	3	3m	32		
Monoclinic	2 or m		2	m	none		
Triclinic	$\bar{1}$		1		none		
Total Number	11 groups		10 groups		11 groups		

Figure 1.1: **Classification of 32 crystal point groups.**

in ferroelectricity. Following the wide success of the simple $BaTiO_3$-based ceramic transducer, it was rather natural that people started to examine other ferroelectric perovskite compounds for potential applicability in the early 1950s. The very early discoveries of the ferroelectricity in pure $PbTiO_3$ and $PbTiO_3 : PbZrO_3$ (PZT) were carried out in Japan by Shirance and Takeda [20], Shirane et al. [21], and Sawaguchi [22] in the 1950s. Later on, Jaffe and coworkers' studies [23] established the PZT system as exceptionally suitable for the formulation of piezoelectrics in this composition system. Until today, ferroelectric materials keep offering a wide range of useful properties, including ferroelectric hysteresis (used in nonvolatile memories), high permittivity (used in capacitors), high piezoelectric effects (used in sensors, actuators and resonant wave devices such as radio-frequency filters), high pyroelectric coefficient (used in infra-red detectors), strong electro-optic effects (used in optical switches) and anomalous temperature coefficients of resistivity (used in electric-motor overload protections circuits).

Multiferroics are defined as materials that exhibit more than one of the primary ferroic properties, ferromagnetism (a magnetization that is switchable by an applied magnetic field) , ferroelectricity (an electric polarization that is switchable by an applied electric

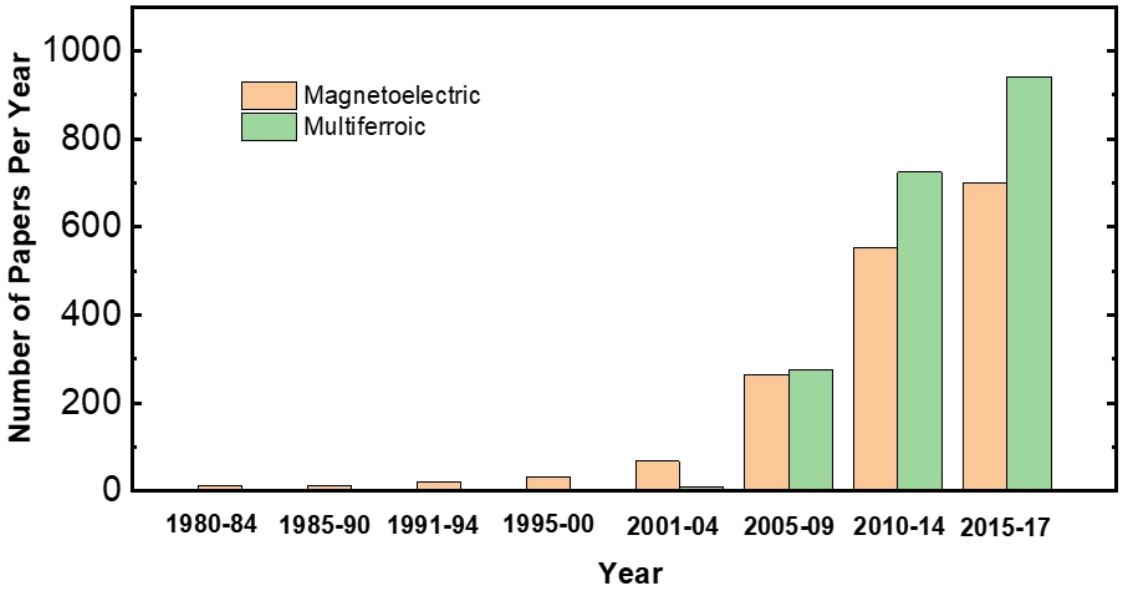

Figure 1.2: **History of multiferroics and magnetoelectric effect.** Number of papers per year on magnetoelectric effect and multiferroics.

field) and ferroelasticity (a deformation that is switchable by an applied stress) in the same phase [24–27]. The earliest result of a search of 'multiferroic' on Web of Science yields the paper "Why are there so few magnetic ferroelectrics?" from Nicola A. Hill published on 2000 [28]. However, the interplay between electricity and magnetism was first observed by Hans Christian Oersted noticed in 1820, that a magnetic compass needle deflected when he switched the current in a nearby battery on or off. In the 1860s, a systematic mathematical expression of electromagnetism was built by James Clerk Maxwell. Although this interaction is well studied for centuries, finding real materials consisting the magnetoelectric coupling is not easy due to the contradiction between the origin of the magnetism and ferroelectricity [28]. Nevertheless, multiferroics have attracted lots of attentions not only due to the scientific interest in their physical properties, also the potential capabilities for applications as actuators, switches, magnetic field sensor or new types of electronic memory devices [29–33]. Intense activities were stimulated from the discovery of the availability to creating multiferroic materials using practical methods from 2000 [28]. Figure 1.2 shows the number of papers per year on multiferroic and magnetoelectric from a Web of Science search until 2017.

1.2 Proper and improper ferroelectricity

Proper ferroelectrics refer to systems, in which the structural instability toward the polar lattice distortion is the main driving force of the ferroelectric transition [1, 34]. In other words, the polar lattice distortion is the primary order parameter. Based on the Landau theory, we can write down the free energy of a proper ferroelectric system as:

$$f(T) = f_0(T) + \alpha(T - T_c)\mathcal{P}^2 + \frac{1}{2}\beta\mathcal{P}^4 + \frac{1}{3}\gamma\mathcal{P}^6 + O(\mathcal{P}^8) \tag{1.1}$$

where $\mathcal{P}$, the polar lattice distortion, is the primary order parameter. In proper ferroelectrics, the polarization is proportional to the amplitude of the polar lattice distortion ($P \approx \mathcal{P}$) . Only even order terms of $\mathcal{P}$ appear in the free energy because f(T) should be conserved under the spatial inversion symmetry operation. The system undergoes a first order phase transition if $\alpha > 0$, $\beta < 0$ and $\gamma > 0$, i.e. the first derivative of the free energy with respect to the primary order parameter at T_c is not continuous. When $\beta > 0$, the $\mathcal{P}^6$ and higher order terms can be neglected resulting in a second-order phase transition. The free energy as a function of the order parameter $\mathcal{P}$ is shown in Figure 1.3(c). When the temperature is above the ferroelectric Curie temperature (T_c), the zero polarization minimizes the energy, corresponding to a paraelectric state. The Landau free energy has a double-well shape when the temperature is below T_c, which allows finite non-zero polarization in the ground state.

$PbTiO_3$ [35–39] and $BaTiO_3$ [40, 41] are the archetypal ferroelectric perovskites and the ground state (lowest energy) structure is shown in Figure 1.3(a) [4]. The origin of ferroelectricity in $PbTiO_3$ and $BaTiO_3$ is hybridization between the formally empty Ti $3d$ states and filled O $2p$ states [38]. In a complementary picture, ferroelectricity in $PbTiO_3$ arises from the condensation of the polar lattice distortion, the displacement of the Ti and Pb cations against the oxygen anions as shown in Figure 1.3(b), which breaks all symmetries (including inversion symmetry) that would otherwise forbid the appearance of ferroelectricity [4].

Unlike the proper ferroelectrics, in which the polar lattice distortion is the main driving force of the transition, the polarization, in improper ferroelectrics, is only part of a more complex lattice distortion or it appears as an accidental by-product of some other

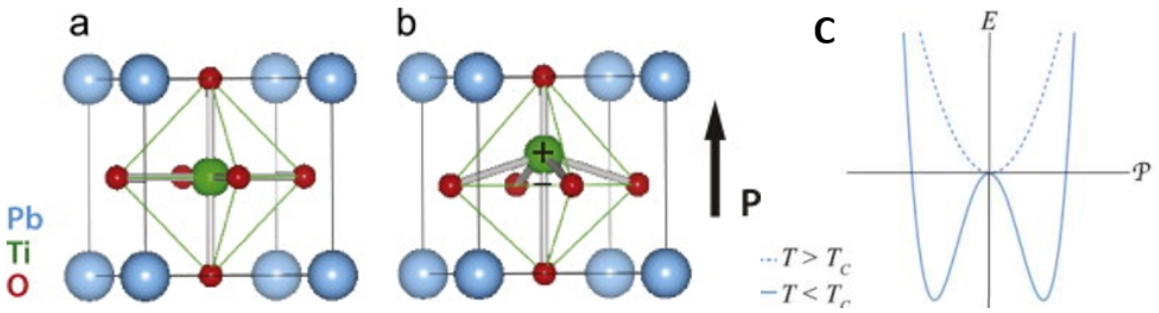

Figure 1.3: **Crystal structure and behavior of energy of $PbTiO_3$, a archetypal proper ferroelectric perovskite. This figure is from reference** [4] (a) Paraelectric $Pm\bar{3}m$ structure of $PbTiO_3$. (b) Ground state ferroelectric $P4mm$ structure of $PbTiO_3$. A displacement of the Ti and Pb cations against the oxygen anions gives rise to a spontaneous polarization and relates the ground state to the nonpolar $Pm\bar{3}m$ structure that $PbTiO_3$ is found in above $\sim$ 760 K. The cell also undergoes a spontaneous strain from cubic to tetragonal. (c) The behavior of the energy as a function of the polarization when the temperature, T, is above and below the Curie temperature (T_c) of the primary order parameter for a proper ferroelectric transition.

ordering [1, 42]. The Landau free energy has an extra term in addition to Equation 1.1 [42]:

$$f(T) = f_0(T) + \alpha\mathcal{P}^2 + \beta\mathcal{P}^4 + f(\mathcal{Q}^2, \mathcal{Q}^4) + \delta\mathcal{Q}^n\mathcal{P} + O(\mathcal{P}^6) \qquad \alpha > 0, \beta > 0 \qquad (1.2)$$

where $\mathcal{P}$ indicates the polar lattice distortion and $\mathcal{Q}$ is the primary distortion (i.e., the primary order parameter). To minimize the free energy, the polarization appears below T_c only when $\mathcal{Q}$ is nonzero as shown in Figure 1.4(c). This implies the polar lattice distortion $\mathcal{P}$ is a by-product of the primary lattice distortion $\mathcal{Q}$.

Hexagonal manganites ($REMnO_3$) belong to improper ferroelectrics with structure transitions resulting from the size mismatch between RE (rare earth element) and Mn atoms [43]. In $YMnO_3$ [44, 45], the primary distortion is a single unstable mode with $q = (\frac{1}{3}, \frac{1}{3}, 0)$ (the K mode) consisting of a rotation of the MnO_5 trigonal-bipyramids and a buckling of the yttrium planes, which results in a tripling of the unit cell volume, as shown in Figure 1.4(a,b). Due to the symmetry-allowed coupling between $\mathcal{P}$ and $\mathcal{Q}$, the primary order distortion must be switched to flip the polarization in improper ferroelectrics. In this case, n=3 in the Landau free energy expressed by equation 1.2. In $YMnO_3$, $\mathcal{Q}$ implies the MnO_5 polyhedron buckling, therefore the buckling orientation must change when the polarization is reversed by an external electric field. More difference between proper and improper ferroelectrics can be seen in Table 1.1.

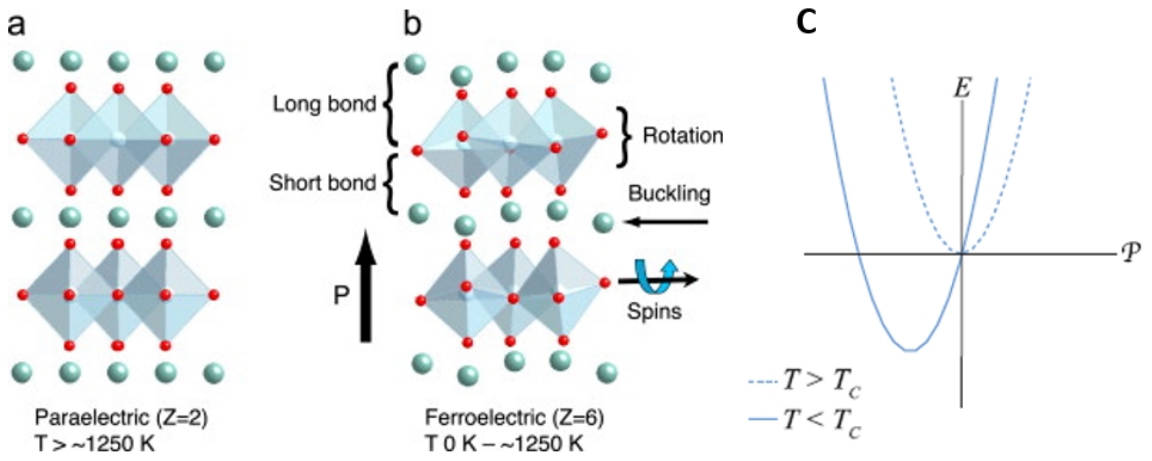

Figure 1.4: **Crystal structure and behavior of energy of $YMnO_3$, an improper ferroelectrics. This figure is from reference** [4] (a) Structure of the paraelectric phase of the improper ferroelectric $YMnO_3$. (b) Structure of the ferroelectric phase and direction of the polarization, P. (c) The behavior of the energy as a function of the polarization when the temperature, T, is above and below the Curie temperature (T_c) of the primary order parameter for an improper ferroelectric transition.

	Mechanism of inversion symmetry breaking	Materials
Proper	Covalent bonding between $3d^0$ transition metal (Ti) and oxygen	$BaTiO_3$
	Polarization of $6s^2$ lone pair of Bi or Pb	$BiMnO_3$, $BiFeO_3$, $Pb(Fe_{\frac{2}{3}}W_{\frac{1}{3}})O_3$
Improper	Structural transition "Geometric ferroelectrics"	K_2SeO_4, Cs_2CdI_4, hexagonal $REMnO_3$
	Charge Ordering "Electron ferroelectrics"	$LuFe_2O_4$
	Magnetic ordering "Magnetic ferroelectrics"	Orthorhombic $REMnO_3$, $REMn_2O_5$, $CoCr_2O_4$

Table 1.1: Classification of ferroelectrics, which is from reference [1].

On the other hand, $YMnO_3$ is not multiferroic material, even though an electric field would switch the MnO_5 polyhedron buckling direction, this distortion does not affect the magnetic properties in any meaningful way [4]. An interesting question is whether or not

we can design a kind of improper ferroelectrics, in which the polarization and magnetization both result from the same lattice distortion. In this case, the cross-coupling must be impressive.

1.3 Hybrid improper ferroelectricity

1.3.1 Introduction

Hybrid improper ferroelectrics (HIF) are the improper ferroelectrics with a peculiar trilinear lattice coupling or higher term in the free energy [46]. For example, the presence of the term $\gamma\mathcal{Q}_{R_4^+}\mathcal{Q}_{M_3^+}\mathcal{P}$, suggests that $\mathcal{P}$ is the by-product of two symmetry inequivalent lattice distortions, $\mathcal{Q}_{R_4^+}$ and $\mathcal{Q}_{M_3^+}$. In such a case, the polarization can be reversed by switching either R_4^+ or M_3^+ distortion and will keep the same if both of them are switched [6]. Consequently, the magnetic property linked to one or the two distortions can be controlled by an external electric field, which makes HIF being promising candidates for multiferroics.

The most studied hybrid improper ferroelectrics are the A-site ordered double perovskites and Ruddlesden-Popper (RP) phase system, in which both the ferroelectricity and ferromagnetism are induced by the same octahedral rotations [7]. In the hybrid improper ferroelectric system discussed by N.A. Benedek and C.J. Fennie [46], the electric polarization is induced by the inversion symmetry breaking through $a^-a^-c^+$ (Glazer Notation) octahedral rotation. In the Glazer Notation system, three components with superscripts imply rotations along three different Cartesian directions. The lower case letters represent the rotation amplitude, "+" ("-") implies in-phase (out-of-phase) rotation along a specific axis.

1.3.2 Antiferroelectric ABO_3 perovskite with octahedral rotations

The ideal cubic unit cell, which belong to $Pm\bar{3}m$ space group, in the simplest ABO_3 perovskite is shown in Figure 1.5(a,b). In real materials, there always exists some lattice distortions to minimize the system's free energy. Theoretical calculations on $SrZrO_3$ is shown in Figure 1.6. The ground state is orthorhombic $Pnma$ instead of the ideal cubic $Pm\bar{3}m$ by going through $a^-b^+a^-$ octahedral rotation. The symmetry of the $Pnma$ phase

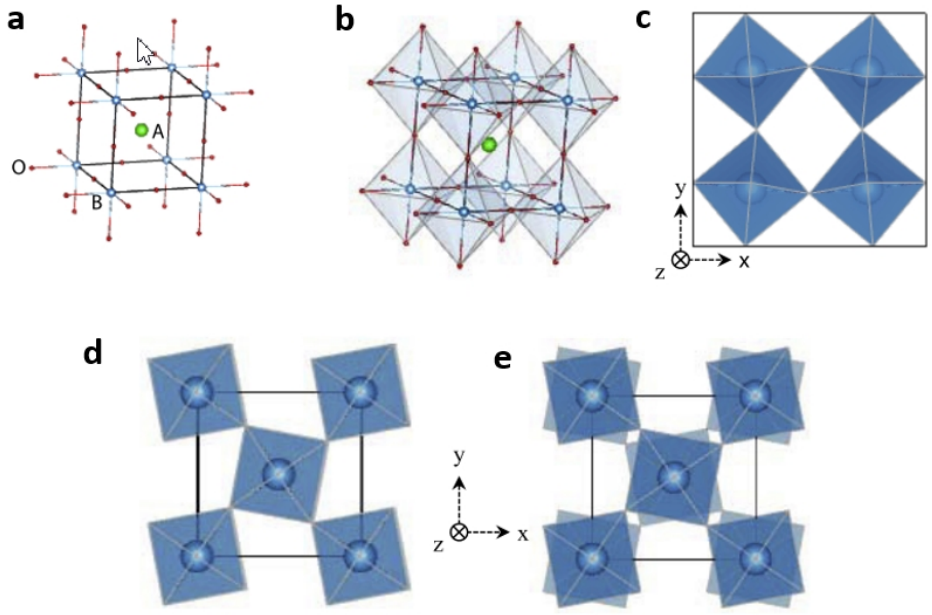

Figure 1.5: **The crystal structure and octahedral distortion in ABO_3 perovskite oxides, which is from reference [5]** (a) The crystal structure of ABO_3 perovskite oxide in $Pm\bar{3}m$ (cubic) phase. (b) The same structure as in (a) but showing the BO_6 octahedral network. (c) Schematic illustration of the $a^0b^+b^+$ structure, indicating the adjacent octahedrons in the same plane rotate in opposite sense to maintain corner connectivity. (d, e) Schematic illustration of the $a^0a^0c^+$ and $a^0a^0c^-$ rotation patterns. The in-phase rotations and out-of-phase rotations of the octahedron about the z-axis are discernible in (d) and (e), respectively. (Note that for clarity the A-site cations and the oxygen atoms are omitted from panels (c-e)).

is caused by two octahedral rotations, R_4^+ and M_3^+, as well as two kinds of A-site cation displacements. In fact, the antipolar A-site cation displacement shown in Figure 1.7(c) is the key to the interior layered polarization, which is allowed by the symmetry lowering due to the oxygen rotations. For instance, the $Cmcm$ and $Pnma$ phases arise from the condensation of M_3^+ and R_4^+ rotational modes which transform like X_5^+. It means X_5^+ antipolar distortions will appear when there are two types of rotations condensed simultaneously. This originates from the trilinear coupling term $\gamma \mathcal{Q}_{R_4^+} \mathcal{Q}_{M_3^+} \mathcal{P}$ in the free energy expansion [47]. A similar coupling tern can be used to explain the A-site cation displacement in the $Imma$ structure shown in Figure 1.7(b).

Figure 1.8 shows how the simultaneous condensation of R_4^+ and M_3^+ distortions creates

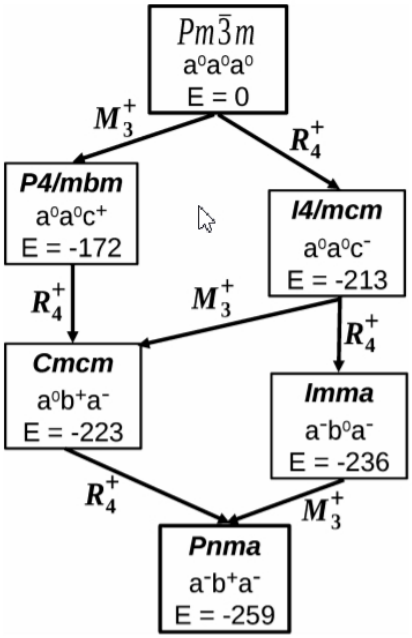

Figure 1.6: **Energies (in meV/f.u.) of different phases of $SrZrO_3$ after full structural relaxations in comparison to that of the cubic phase taken as reference, which is from reference [6].** One formula unit (f.u.) consists in a five-atom ABO_3 unit. Arrows indicate the type of additional title component (R_5^- or M_3^+) appearing from one structure to another. Glazer's notations clarity along which direction this tilt component appears.

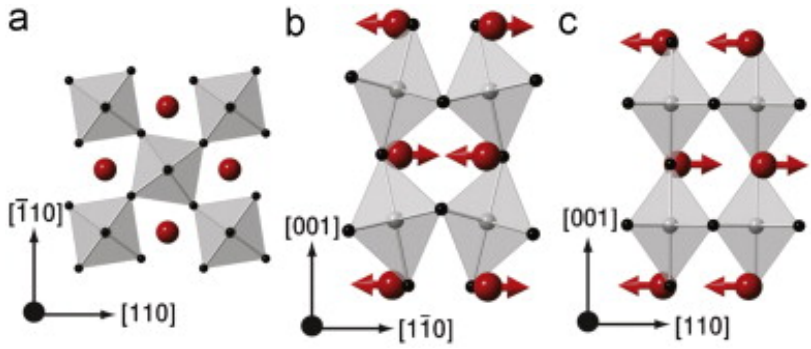

Figure 1.7: **Three different normal modes in *Pnma* structure. This figure is from Reference [7].** (a) Octahedral rotation about [001]. (b) Rotation about [110] with A-site displacement (c) Antipolar A-site displacement without rotation

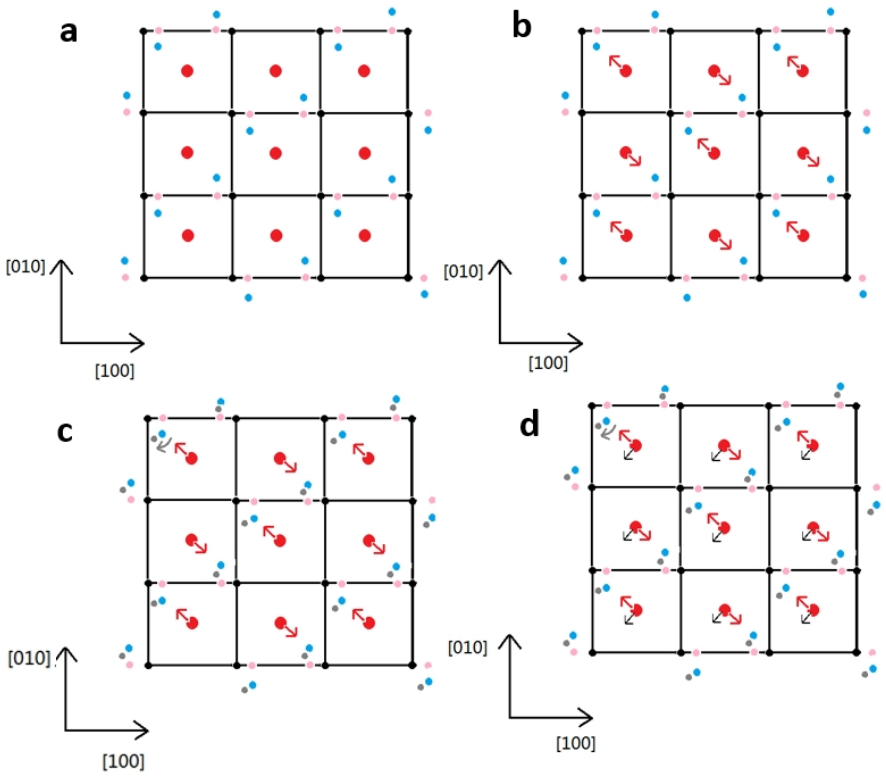

Figure 1.8: **Octahedral rotations induced atom movements in the AO layer**. The red dots indicate the A-site cation, while other color dots refer to the position of oxygen atoms, which lay on the same layer with A-cite cation, after different lattice distortions. (a) Black dots represent the position of oxygen when there is no tilting. They move to the pink position when each BO_6 octahedron rotates under $a^-a^0a^0$ mode. They continue moving to blue positions when each B_6 octahedron rotates in $a^-a^-a^0$ mode. (b) Red arrows indicate the moving direction of A-site cation resulting from the symmetry breaking. (c) Gray dots denote the final position of oxygen after all $a^-a^-c^+$ rotation. (d) Black arrows indicate another moving of the A-site cation after the BO_6 octahedron's rotation along the [001] direction.

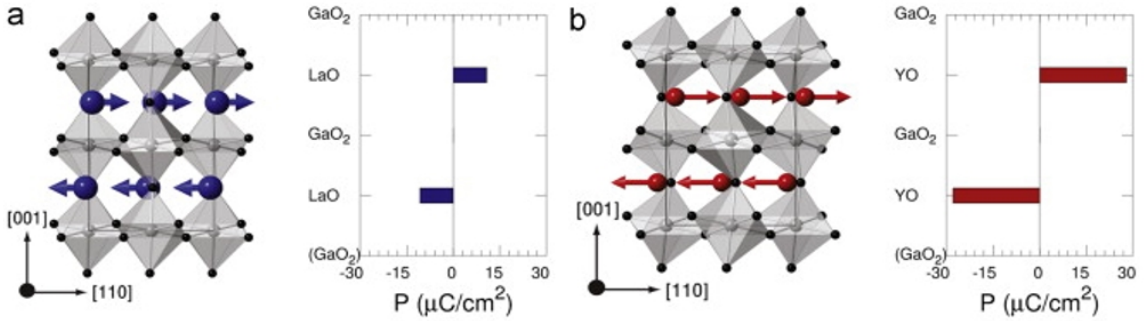

Figure 1.9: **The intralayer polarization of (a)** $LaGaO_3$ **and (b)** $YGaO_3$ **in the** $Pnma$ **ground state.** The right of each figure represents the amplitude of the layer-resolved polarization from first-principles calculations. These figures are taken from reference [7]

the X_5^+ antipolar A-site atoms' displacement. The A-site cations' displacement resulting from the breaking of neighboring oxygen atoms' symmetry in Figure 1.8(B) corresponds to that in Figure 1.7(b), while the displacements in Figure 1.8(d) corresponds to that in Figure 1.7(c). Apparently, the induced polarization along the $[1\bar{1}0]$ shown in Figure 1.8(b) is canceled out. As a result, the layered net polarization is attributed to the A-site cations' displacement along the [110] direction, as shown in Figure 1.8(d).

Unfortunately, such well-polarized AO layers cannot generate non-zero net polarization since octahedral rotations can never by themselves remove the inversion center at the B-site atoms. Note that such opposite polarization structure is not antiferroelectric because the opposite polarizations are determined by the octahedral structure, which cannot be switched by external electric field without changing the lattice structure.

Figure 1.9 shows the first-principles calculated intralayer polarization in $LaGaO_3$ and $YGaO_3$ [7]. Although octahedral rotations and cations' displacements in ABO_3 perovskites can induce intralayer polarization, the net polarization is zero since B-site cation is sitting on the inversion center.

1.3.3 Ferroelectric $(AA')B_2O_6$ double perovskites

As we discussed before, in bulk ABO_3 perovskites inversion centers are found on both A- and B-sites, which prevents the generation of net polarization. If one can find a way to break the inversion symmetry, we might have ferroelectric phase. From symmetry analysis,

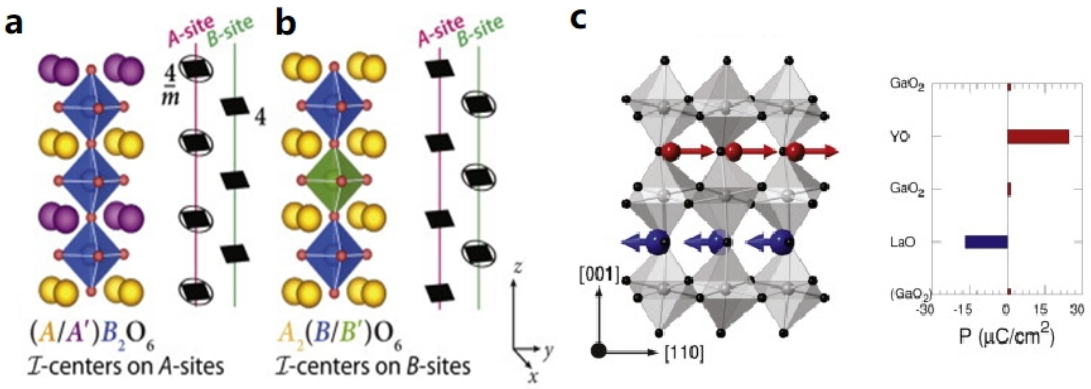

Figure 1.10: **Net electric polarization in $(A/A')B_2O_6$ double perovskites** (a) In $(A/A')B_2O_6$, cation ordering lifts the inversion centers on the B-site, which supports the form of hybrid improper ferroelectricity. (b) In $A_2(B/B')_2O_6$, net polarization is still zero due to the same amplitude and opposite direction intralayer polarization in the nearby AO layers. (c) Intralayer polarization in $LaYGa_2O_6$ from first principles calculation. Figures are taken from reference [7].

only A/A' layered double perovskites which lifts the inversion center on the B-site can produce net polarization, as shown in Figure 1.10(a). On the contrary, figure 1.10(b) shows the B/B' layered double perovskites will remain $4/m$ symmetry on the B-site. In this case, the intralayer polarization in nearby AO layers will keep being the same amplitude and opposite direction resulting zero net polarization in bulk. Figure 1.10(c) shows the calculated intralayer polarization in $LaYGa_2O_6$, a kind of A site ordered double perovskites.

Furthermore, Andrew T. Mulder [47] performed the calculation of polarization as a function of the tolerance factor:

$$P \propto \Delta\tau f(1-\tau_{avg}) \approx \Delta\tau(1-\tau_{avg}) \propto (r_A - r_{A'})[c-(r_A+r_{A'})] \tag{1.3}$$

Here $\tau \equiv \frac{r_A+r_O}{\sqrt{2}(r_B+r_O)}$ is the tolerance factor of ABO_3 perovskite, which correlates to the stability toward orctahedral rotations. r_A, r_B, r_O imply the radii of A-site cation, B-site cation and oxygen, respectively. $\tau_{avg} = \frac{\tau_{ABO_3}+\tau_{A'BO_3}}{2}$ and $\Delta\tau = \frac{\tau_{ABO_3}-\tau_{A'BO_3}}{2}$.

Besides these theoretical calculation, there are some experimental realizations on this idea. In 2007, M. Dawberetal [8] prepared $PbTiO_3/SrTiO_3$ superlattice on 0.5% Nb doped STO (001) substrates using off-axis radio-frequency magnetron sputtering to fulfill the double perovskites property at the interface. Figure 1.11(a) shows the 3/3 PTO/STO superlattice structure. The polarization vs. electric field hysteresis loop measured using PUND

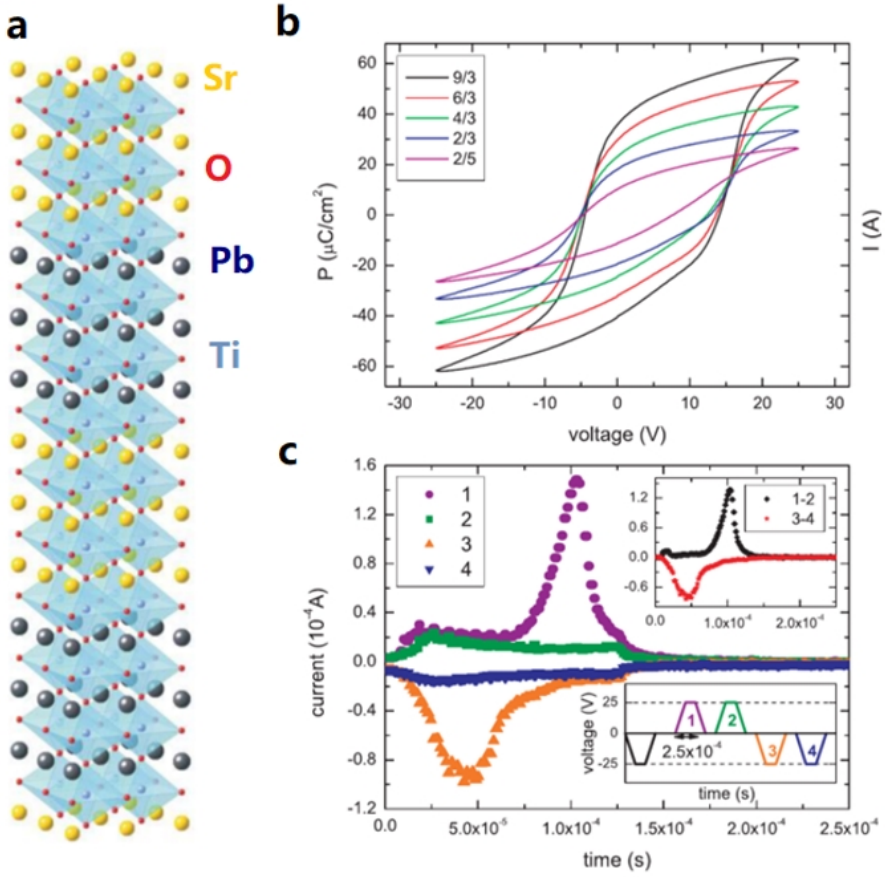

Figure 1.11: **Polarization hysteresis loop of 3/3** PTO/STO **superlattice** (a) Schematic of the 3/3 PTO/STO superlattice structure. (b) Polarization vs. electric field hysteresis loop. (c) Current as a function of time for different sequences in the PUND measurements. Figures are taken from reference [8].

(positive up and negative down) method [48] is a good indication of the ferroelectric property as shown in Figure 1.11(b). The detailed current curves as a function of time for different sequences during the PUND measurements, shown in Figure 1.11(c) demonstrate the reliability of the remanent polarization's amplitude.

1.3.4 Ferroelectric $(ABO_3)_2/AO$ Ruddlesden-Popper phase

In this section, we talk about another strategy to generate electric polarization based on the ABO_3 building block. In this method, we utilize the Ruddlesden-Popper (RP) phase [49], a homologous series of structures with formula $A_{n+1}B_nO_{3n+1}$. It can also be expressed as $(ABO_3)_n/AO$, which suggests the perovskite blocks are stacked along the [001] direction

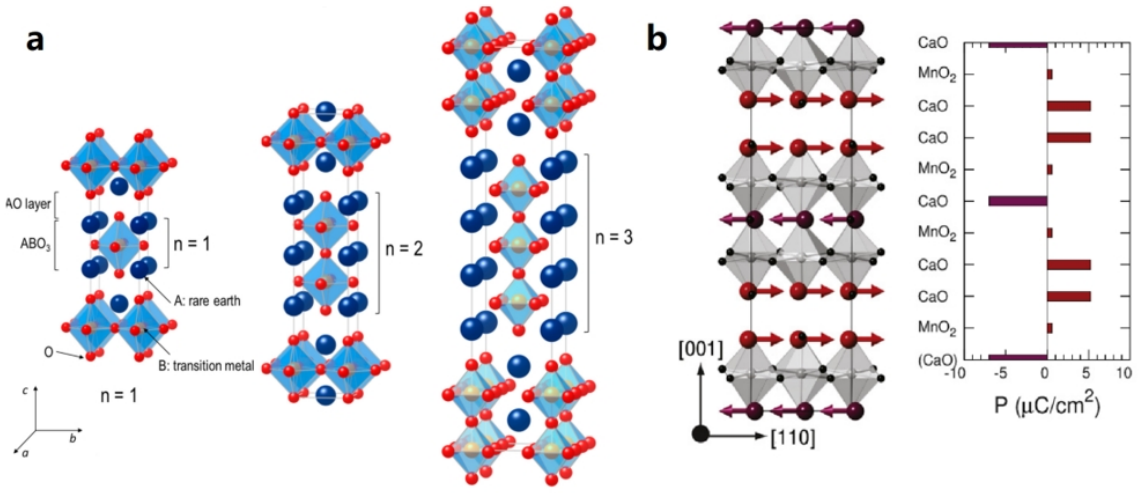

Figure 1.12: **Schematic structure of $(ABO_3)_nAO$ RP phase and calculated polarization in $(CaMnO_3)_2CaO$.** (a) Crystal Structure of $(ABO_3)_nAO$, n=1, 2, 3. (b) Intralayer polarization in $(CaMnO_3)_2CaO$ from first principles calculation. Figures are from reference [7] and [9].

with an extra AO sheet inserted every n perovskite layers as shown in Figure 1.12(a). In the n=2 case, within the perovskite block, there are three AO layers. So the layered polarization induced by antipolar AO motion will not cancel out with each other, resulting in a net polarization in the bulk system. Using first principles calculation, N.A. Benedek studied the lattice dynamical properties of $Ca_3Ti_2O_7$ and $Ca_3Mn_2O_7$ [7]. Figure 1.12(b) clearly shows how layered $CaMnO_3$ creates a net polarization in $Ca_3Mn_2O_7$ system. The bulk polarization is parallel with the [110] direction in the high-symmetry cubic coordinates, which is along the [001] direction in the low symmetry orthorhombic unit cell.

1.3.5 Ferroelectric $A'(AB_2O_7)$ Dion-Jacobson phase

The Dion-Jacobson (DJ) compounds (general formula $A'[A_{n-1}B_nO_{3n+1}]$) [50, 51] have recently attracted lots of attention as hybrid improper ferroelectrics with much larger electric polarizations. It has $[A_{n-1}B_nO_{3n+1}]$ blocks of 'perovskite' structure, n octahedral thick, stacking along the c axis. These 'perovskite' blocks are separated by layers containing cations A' only. As the same as in the RP compounds, the polarization is also driven by in-phase rotation of adjacent octahedrons around the $c-axis$ and out-of-phase rotation around the $a/b-axis$ ($a^-a^-c^+$ in Glazer notation). Nevertheless, the A-site atomic

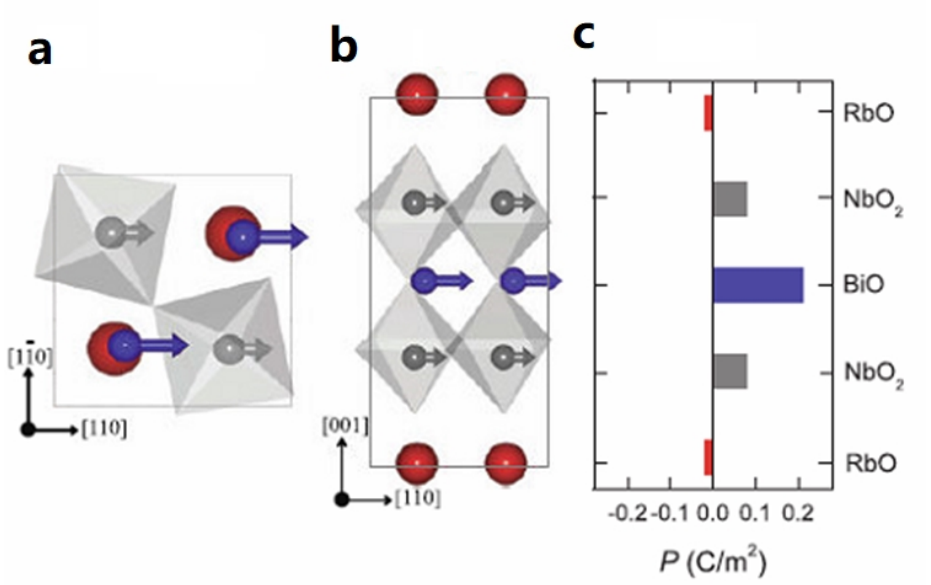

Figure 1.13: **Crystallographic structure and intralayer polarization of $RbBiNb_2O_7$.** Top view (a) and side view (b) of the polar displacement from each cation shown by arrows. (c) Estimated intralayer polarization from first principles calculations. Figures are from reference [10].

displacements comprising the polar mode are ferro- in DJ compounds rather than anti-distortive, resulting in much larger electric polarization [52], as shown in Figure 1.13. For instance, $CsBiNb_2O_7$ [52], $RbBiNb_2O_7$ [53] and $RbNdNb_2O_7$ [54] (n=2 DJ compounds) have been predicted to have spontaneous polarization of 40, 36 and 24 $\mu C/cm^2$ from first principles calculation, respectively.

1.4 Polar magnets

As we discussed in section 1, out of a total of 32 crystal point groups, 10 are polar *i.e.* crystals which possess a unique polar axis showing different properties at the two ends as shown in Figure 1.1. Although multiferroics have attracted lots of attention, finding real materials consisting the ferroelectricity, magnetism and magnetoelectric coupling is not easy due to the contradiction between the origin of the magnetism and ferroelectricity. Due to the intrinsic property of polar materials, if we could dope magnetic ions inside we will get the coexistence of ferroelectricity and magnetism, which offers a great opportunity for the existence of magnetoelectric coupling. Here, in chapter 4, we will discuss the $M_2Mo_3O_8$

(M=Fe, Mn, Ni, Co, Zn) system, which has the largest ME coefficient in all discovered polar magnets.

Chapter 2

First room temperature ferroelectric Sn insulator ($Sr_3Sn_2O_7$; n=2 RP phase) and its polarization switching kinetics

2.1 Introduction: importance of finding ferroelectric Sn materials

Ferroelectric materials offer a wide range of useful properties. These include ferroelectric hysteresis (used in nonvolatile memories), high permittivity (used in capacitors), high piezoelectric effects (used in sensors, actuators and resonant wave devices such as radio-frequency filters), high pyroelectric coefficient (used in infra-red detectors), strong electro-optic effects (used in optical switches) and anomalous temperature coefficients of resistivity (used in electric-motor overload protections circuits). Among ferroelectric materials, ABO_3 perovskites have been the choice of materials for both fundamental interest and technological importance due to the large magnitude of polarization and strong response of their polarization to electric or stress fields [27, 28, 37, 55, 56]. Up to today, the most widely used ferroelectric ceramics are those based on the $PbTiO_3 - PbZrO_3$ solid solutions, generically called PZT. The PZT is composed of about 60 wt.% of lead, which rises ecological concerns: thus, some countries have legislated to replace these materials by lead-free ceramics since lead is a toxic element that affects the human health and the environment [57–59].

There has been some success in find new Pb-free ferroelectrics, such as $BiFeO_3$ [27], $(K_{0.5}Na_{0.5})NbO_3$ [60], $Bi_{2.5}Na_{3.5}Nb_5O_{18}$ [61], etc. However, few reports on the success of compounds containing Hf^{4+}, Zr^{4+}, Ge^{4+} or Sn^{4+}, which belong to the same group with Pb in the periodic table. Being tetravalent ions, they can form in perovskite structure, but these perovskites are not ferroelectric, presumably due to broad bandwidth or poor hybridization with anions, which are related to their inappropriate ionic size. For example, $Pb(Ge, Sn)O_3$ and $(Ba, Sr)(Zr, Hf, Ge, Sn)O_3$ are all centrosymmetric [62–65]. $PbHfO_3$ and $PbZrO_3$ are both antiferroelectric at room temperature [66, 67]. Thus, finding new

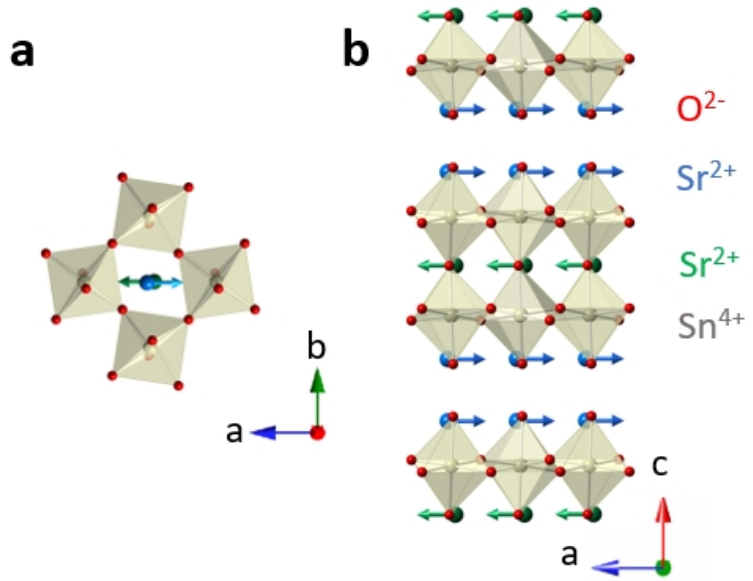

Figure 2.1: **The proposed ferroelectric $a^-a^-c^+$ distortions and intralayer polarization in $Sr_3Sn_2O_7$.** (a) The c-direction view. (b) The b-direction view. The blue and green arrows indicate the Sr displacements along the a-direction.

ferroelectric compounds with Sn, which belongs to the same group with Pb in the periodic table, can be ground-breaking in ferroelectric research.

2.2 Debate on the ground state of $Sr_3Sn_2O_7$

Finding ferroelectric materials containing Sn is crucially important. However, the synthesis of materials containing Sn is always challenging, primarily due to the poor chemical reactivity of, e.g., SnO_2. To overcome the refractory nature of SnO_2, very high-temperature treatments are required, while raw materials tend to evaporate at these temperatures. In fact, only limited Sn ferroelectrics have been experimentally discovered. Theoretically, $SnTiO_3$ with Sn^{2+} was predicted to be ferroelectric [68], but no experimental confirmation has been reported. $Sn_2P_2(S_{1-x}Se_x)_6$ with formal valence of 2+ for Sn has the highest Curie temperature 337 K when x=0 [69, 70]. However, $Sn_2P_2(S_{1-x}Se_x)_6$ compounds are ferroelectric semiconductors or photoconductors and their Curie temperature is too close to room temperature, limiting their usage[71]. To the best of our knowledge, there isn't any room temperature ferroelectric Sn insulator before our study on $Sr_3Sn_2O_7$.

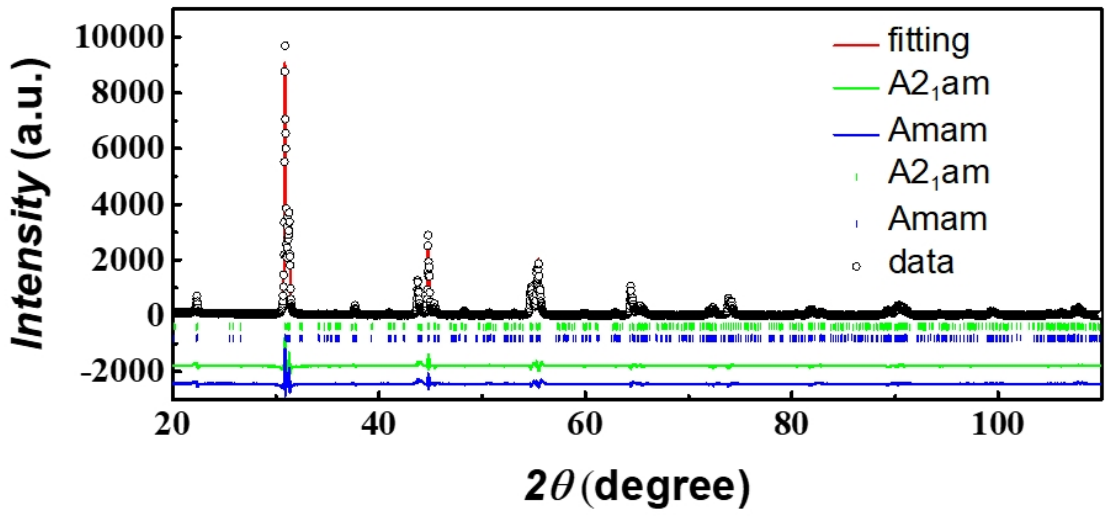

Figure 2.2: **X-ray powder diffraction pattern of $Sr_3Sn_2O_7$ at 285 K.** Crosses represent experimental data points. The calculated ($A2_1am$) and difference intensities are shown as red, and green ($A2_1am$)/ blue ($Amam$) curves, respectively. The two sets of vertical bars indicate the Bragg conditions for $A2_1am$ (green) and $Amam$ (blue) space groups.

$Sr_3Sn_2O_7$ with Sn^{4+}, consisting of stacked perovskite double layers, belongs to RP phase ($(ABO_3)_nAO$, n=2; lattice parameter a = 5.710, b = 5.736, c = 20.688 Å). Sm^{3+} doped $Sr_3Sn_2O_7$ has attracted a significant attention as a promising candidate for stress sensors showing impressive mechanoluminescence [2, 72]. An early result of powder neutron diffraction experiments indicated that $Sr_3Sn_2O_7$ adopts a C-centered orthorhombic structure (space group $Cmcm$) [73]. However, recent theoretical results have proposed a noncentrosymmetric structure ($A2_1am$) originating from hybrid improper ferroelectricity, which results from the condensation of complex lattice distortions [46, 47] as shown in Figure 2.1. Furthermore, there are few studies on this material due to the difficulty in synthesizing high-quality samples coming from the poor chemical reaction. Therefore, preparing high-quality $Sr_3Sn_2O_7$ materials and studying the property using more robust techniques become crucially important.

2.3 Sample Growth and XRD results

Polycrystalline $Sr_3Sn_2O_7$ was synthesized using a conventional solid-state reaction method. The stoichiometric mixture of $SrSnO_3$ (99.995%) and SnO_2 (99.95%) powders was pelletized, and sintered at 1300, 1400, and 1500 $^\circ C$ in air with intermediate grinding. In order to suppress evaporation of raw materials during the solid-sate reaction at high temperatures, we embed a polycrystalline pellet with its own powders, which was sintered in an alumina crucible sealed with high-temperature cement. Using this method, we synthesize successfully a polycrystalline single-phase pellet of orthorhombic $Sr_3Sn_2O_7$ with large grains (20-100 μm in size).

Figure 2.2 represents the XRD results of $Sr_3Sn_2O_7$ poly sample at 285 K. The splitting of a number of reflections indicates a reduced orthorhombic symmetry from paraelectric tetragonal phase ($I4/mmm$, # 139). However, the same extinction rules in both polar $A2_1am$ and nonpolar $Amam$ provide difficulties to distinguish them from X-ray structural refinements. Indeed, our structural refinements of the XRD data, as shown in Figure 2.2, give similar adequate fits for both structural models. The refined atomic coordinates are shown in Table 2.1 for $A2_1am$ and Table 2.2 for $Amam$. A similar dilemma has been reported in hexagonal manganite [74]. Therefore, it is imperative to use more robust techniques to explore the correct crystallographic structure.

$A2_1am$ (# 36) a=5.7333(1)Å, b=5.7057(1)Å, c=20.6637(1)Å					
Atom	Wyckoff position	x	y	z	U_{iso} ($10^2 \times Å^2$)
Sr1	4a	0.0004(12)	0.2512(14)	0	1.6
Sr2	8b	0.4819(20)	0.7457(7)	0.18769(4)	1.5
Sn	8b	0.4943(18)	0.2492(9)	0.09839(4)	1.5
O1	4a	0.0058(36)	0.7835(32)	0	2.1
O2	8b	0.0054(21)	0.6924(20)	0.1980(3)	2.1
O3	8b	0.2856(31)	0.5371(34)	0.0886(4)	1.9
O4	8b	0.2292(36)	0.0240(34)	0.1066(4)	1.9

Table 2.1: The refinement result of $Sr_3Sn_2O_7$ using the structural model of $A2_1am$ (# 36), obtained using powder XRD. Amam structural adopts from reference [2].

Amam (# 63) a=5.7059(1)Å, b=5.7335(1)Å, c=20.6643(1)Å					
Atom	Wyckoff position	x	y	z	U_{iso} ($10^2 \times Å^2$)
Sr1	4c	0.75	0.259	0.5	2
Sr2	8g	0.75	0.261	0.6879	1.3
Sn	8g	0.75	0.749	0.5973	1.3
O1	4c	0.75	0.805	0.5	3.2
O2	8g	0.75	0.712	0.6967	3.2
O3	8e	0	0	0.3939	2.1
O4	8e	0.5	0.5	0.5873	2.1

Table 2.2: The refinement result of $Sr_3Sn_2O_7$ using the structural model of *Amam* (# 63), obtained using powder XRD. Amam structural adopts from reference [2].

2.4 Ferroelastic twin structure

In the study of hybrid improper ferroelectricity, the existence of orthorhombic twin structure in the optical image is a robust evidence of orthorhombic structure. Here, we do well poling on $Sr_3Sn_2O_7$ poly sample and could get a thin transparent piece, which is consistent with the reported large magnitude (4.13 eV) of optical gap [2]. Figure 2.3 represents the transmission polarized optical microscope (POM) images of a polished polycrystalline $Sr_3Sn_2O_7$ specimen. The dark-bright contrast is due to orthorhombic twin domains. These contrasts reverse when the analyzer change between $\psi = 90° + \theta$ and $\psi = 90° + \theta$ (here, ψ is the angle between the polarizer and analyzer and $\theta \approx 5°$ is a small rotation angle). The width of each twin domain is around $5\mu m$. Although the polished surface of each domain is random in general, the almost 90° angle between two straight domain sets in the largest grain in Figure 2.3 indicates the polished surface of the largest grain is close to the $a - b$ plane. Note that the two highly possible structural candidates of polar ($A2_1am$, # 36) and nonpolar (*Amam*, #63) space groups can both give orthorhombic twins as discussed above. And the nonpolar *Amam* structure results from octahedral tilting ($a^-a^-c^0$ or the X_3^- mode) without octahedral rotation ($a^0a^0c^+$ or the X_2^+ mode) [47].

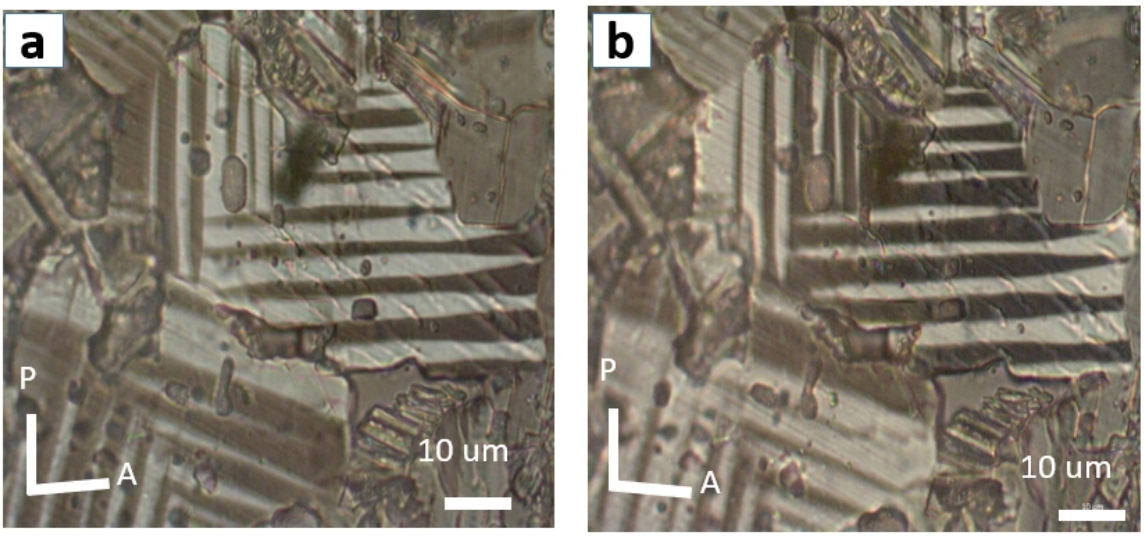

Figure 2.3: **Orthorhombic twin domains in $Sr_3Sn_2O_7$.** (a) and (b) are both POM images of the polished surface of a polycrystalline of $Sr_3Sn_2O_7$ specimen in a transmission mode. The white bar with P (A) represents the direction of the polarizer (analyzer).

2.5 Unveiling ferroelectricity from $P(E)$ loop and TEM images

As we discussed before, utilizing X-Ray and optical observation could not help us demonstrate the existence of ferroelectricity. We need more robust techniques, like polarization switching ($P(E)$) measurements and dark-field transmission electron microscopy (DF-TEM). DF-TEM is an ideal and well-known technique to distinguish polar versus nonpolar phase because of its high spatial resolution and ability to light up specific types of domains using a selected Bragg spot. $P(E)$ hysteresis loop is the most straightforward way to demonstrate the existing of ferroelectricity in a system. We can clearly find the amplitude of remanent polarization and coercive field from the $P(E)$ loop.

Here, Figure 2.4 (a, b) shows typical DF-TEM images on an $a-b$ plane $Sr_3Sn_2O_7$ single grain using the superlattice spots $g+ = (120)$ and $g- = (\bar{1}\bar{2}0)$ for imaging. In Figure 2.4 (a, b), there is a straight boundary between twin A and twin B and a curved wall inside twin B. The electron diffraction patterns, insert of Figure 2.4 (a, b), can demonstrate the 90° orientational relation of orthorhombic twins. The reversed dark-bright domain contrast between Figure 2.4 (a) and (b) indicates unambiguously Friedel's pair breaking owing to a noncentrosymmetric nature of $Sr_3Sn_2O_7$. Electric polarization, shown by red arrows, are along the $a-axis$ based on the polar $A2_1am$ space group. These DF-TEM images

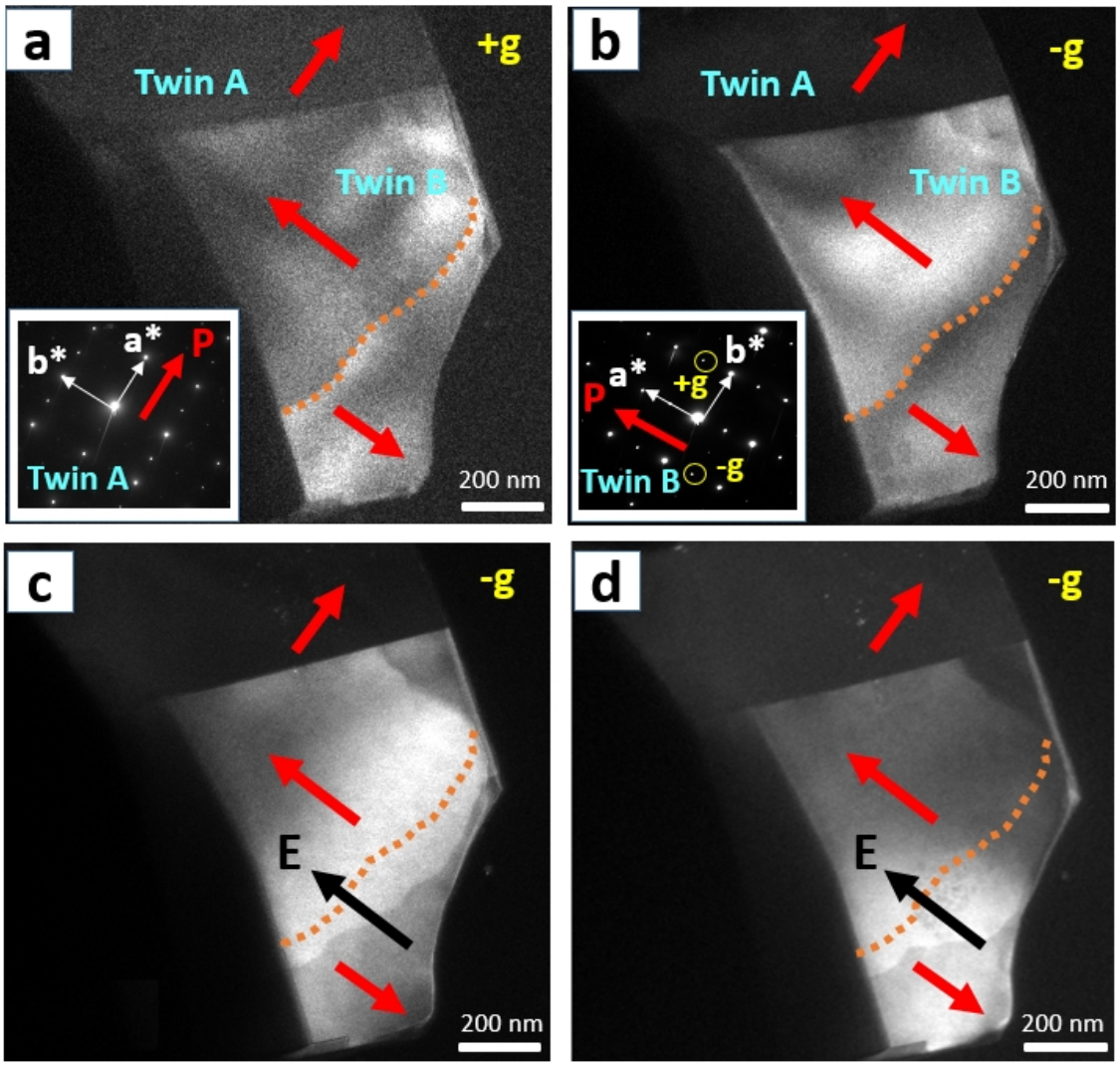

Figure 2.4: **Ferroelectric domains and domain wall motion with focused electron beam-induced poling in $Sr_3Sn_2O_7$.** (a) An $a-b$ plane DF-TEM image taken using the superlattice $g+ = (120)$ spot. (b) A DF-TEM image taken using the superlattice $g- = (\bar{1}\bar{2}0)$ spot. The reversed contrast in (a,b), especially near the yellow square dotted line demonstrates the presence of ferroelectric 180° domains, consistent with the $A2_1am$ space group. The electron diffraction patterns in twin A and twin B are shown by the inserts of (a) and (b), respectively. (c, d) The evolution of these ferroelectric domains under focused electron beam-induced poling. The black arrows in (c, d) depict the poling electric field induced by the focused electron beam. The yellow square dotted lines in (a)-(d) indicate the original position of FE 180° DW. A new dark circular spot around the yellow square dotted line is due to the surface damage by the focused electron beam.

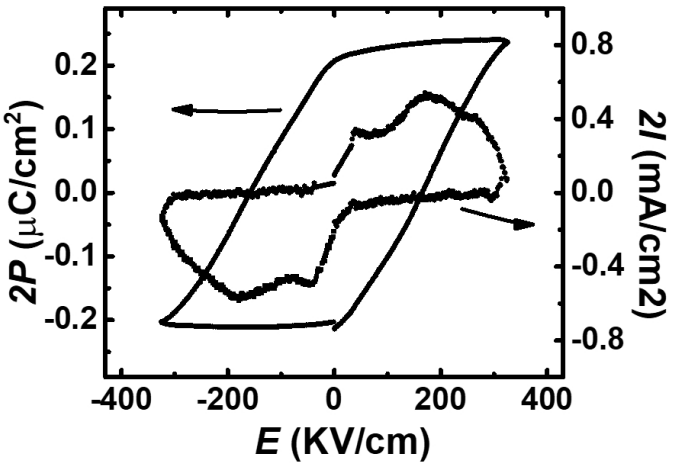

Figure 2.5: **Polarization hysteresis loop of $Sr_3Sn_2O_7$ at 285 K.** Electric polarization (P) and compensated current (I) versus electric field (E) hysteresis loop of a polycrystalline $Sr_3Sn_2O_7$ specimen, measured with a PUND method in oil at frequency $f = 270.27HZ$.

demonstrate the existence of straight ferroelectric 90° domain wall (FE 90° DW) and the tail-to-tail FE 180° DW in a curved feature, as shown by the yellow square dotted line in Figure 2.4.

Moreover, the presence of sub-micrometer size ferroelectric domains is further supported by macroscopic poling experiments. Figure 2.5 shows the electric polarization (P) and compensated current (I) versus electric field (E) hysteresis loop measured at room temperature and frequency $f = 270.27HZ$ using the positive-up-negative-down (PUND) method to get rid of the leakage and capacitance contribution [48]. The existence of clear $P(E)$ hysteresis loops in different electric fields and at different frequencies, as shown in Figure 2.6, unambiguously confirm again the ferroelectric nature of $Sr_3Sn_2O_7$.

Figure 2.5 also presents the compensated current density versus electric field, $I(E)$, curve. The electric fields corresponding to the current peak, $\pm 190KV/cm$, demonstrate the coercive field of polarization flipping. The net remanent electric polarization ($P_n = 2P_{r,exp}$, where $P_{r,exp}$ is the experimentally measured value in a polycrystalline specimen) is $\approx 0.24\mu C/cm^2$. This is small comparing to the theoretically calculated value [47] since there are lots grain boundaries in the poly ceramics. There is no indication of a phase transition from our high-temperature resistivity ($\rho(T)$) measurements up to 1035 K.

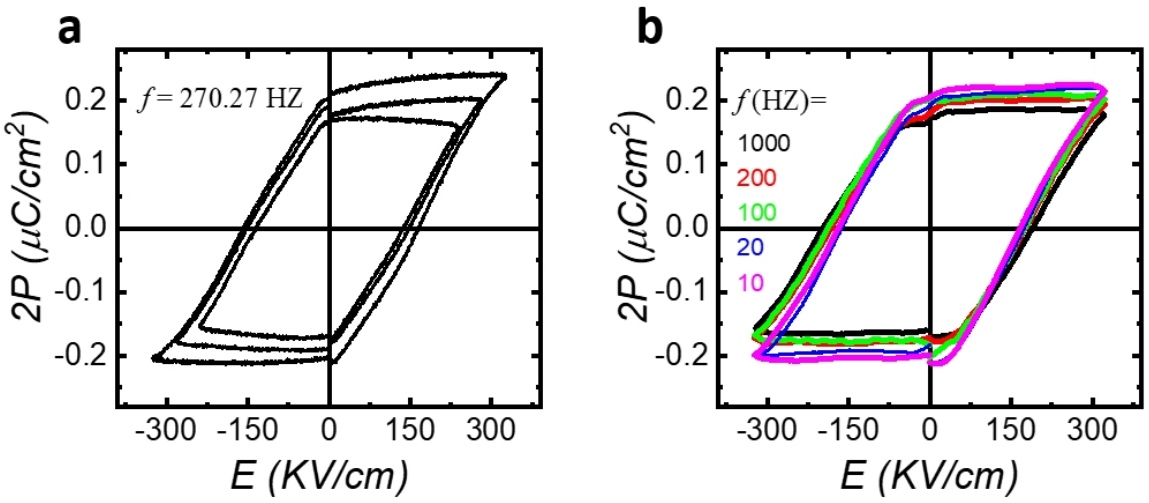

Figure 2.6: **Polarization hysteresis loops of polycrystalline $Sr_3Sn_2O_7$ measured at room temperature.** (a) In different electric fields. (b) At different frequencies.

2.6 Direct observation of domain wall movement in electric field

During the TEM measurement, we can observe the movement of the FE 180° DWs by applying an in-plane poling electric field using a focused electron beam, as shown in Figure 2.4 (c, d). In general, the domain with polarization parallel (antiparallel) with the applied electric field expands (shrinks). In order to obtain a deeper understanding and systematic study of the ferroelectric domain switching kinetics, we perform a DF-TEM experiment along the $b-axis$ as shown in Figure 2.7 (a). Along the $c-axis$, there are different regions with 180° polarization indicated by red arrows. By illuminating a focused electron beam ($\approx 300nm$ in diameter) on a specimen edge, we induce an in-plane electric field indicated by the black arrow with white edge shown in Figure 2.7 (a). Some new domains with polarization parallel with the induced electric field appear immediately, as shown in Figure 2.7 (b). At the same time, two kinds of FE 180° DWs appear: one is a FE charged DW (FE CDW) as the wall between adjacent FE domains having head-to-head electric polarization, as indicated by purple dotted lines in Figure 2.7 (b), and the other is a FE noncharged DW (FE NDW) as the wall parallel to the polarization of adjacent FE domains, as indicated by blue dotted lines in Figure 2.7 (b). Due to charge dissipation after removing the focused electron beam, we observe the evolution of FE DWs in sequential DF-TEM images taken continuously, some of them are shown in Figure 2.7 (c-f). FE NDWs in Figure 2.7 (b-f) move in such a

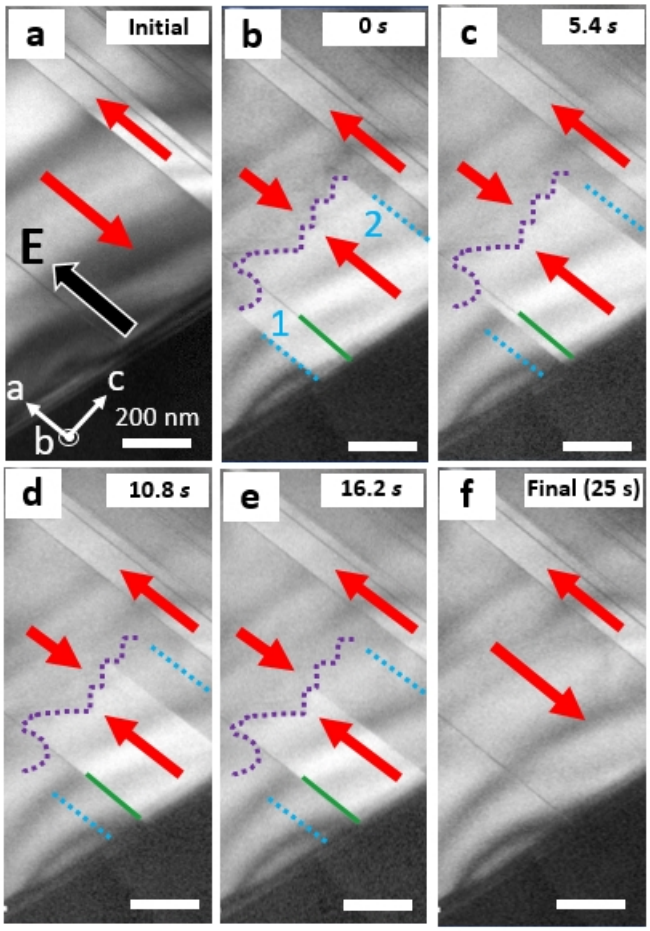

Figure 2.7: **Direct observation of domain wall movement in $Sr_3Sn_2O_7$.** (a) DF-TEM image taken in the $a-c$ plane of $Sr_3Sn_2O_7$. With a focused electron beam, an in-plane electric field is induced as shown by the black arrow with a white edge. (b-e) DF-TEM images taken 0, 5.4, 10.8 and 16.2 s after removing the focused electron beam, respectively. (f) Final state after all the induced charges dissipate away. Purple (blue) dotted line depicts a FE charged DW (FE noncharged DW). Green solid line indicates a disordered region.

way to decrease the newly created domain region, FE NDW 1 and 2 disappear fast with the speed of $\approx 24.6 and 15.0 nm/s$, as shown in Figure 2.8 (b). FE NDWs stop at a disordered region (a kind of stacking fault), shown with a green solid line in Figure 2.7 (b-e). During this process, the FE CDW does not move. Figure 2.7 (f) presents the final image when the nearly created domains disappear completely, which is basically identical with the initial image.

2.7 The polarization switching kinetics and 3D FE domain configuration

The FE NDWs are straight along the $a-b$ plane and perpendicular to the $c-axis$ while the FE CDW is highly curved as shown in Figure 2.7. The local octahedral distortions near a FE CDW and a FE NDW were shown in Figure 2.8 (a). The octahedral tilting ($a^-a^-c^0$) remains intact, while the rotation ($a^0a^0c^+$) directions are opposite across a FE CDW and a FE NDW. Naturally, it is energetically favored to change the rotation direction along the $c-axis$, compared with that along other directions in the $a-b$ plane.

2.8 Summary and outlook

In summary, we discover that layered $Sr_3Sn_2O_7$ with large a optical gap (4.13 eV) exhibits switchable polarization at room temperature, demonstrating that $Sr_3Sn_2O_7$ is the first room-temperature insulating ferroelectric containing Sn^{4+}. From comprehensive characterizations of well-controlled $Sr_3Sn_2O_7$ specimens, we identify that the ground state of $Sr_3Sn_2O_7$ is $A2_1am$, different from a previous experimental report. The net remanent electric polarization is $\approx 0.24 \mu C/cm^{-2}$ at room temperature and originates from hybrid improper ferroelectricity. DF-TEM images, combined with POM images and electron diffraction patterns, indicate the presence of 90° and 180° FE DWs, some of which are charged. Furthermore, the in situ poling results on $Sr_3Sn_2O_7$ using focused electron beams in transmission electron microscopy unveil the intriguing ferroelectric domain switching kinetics: FE non-charged DWs move fast while FE charged DWs do not move, probably due to the octahedral rotation is easier along the $c-axis$. Our discoveries reveal the rich scientific nature of the Sn-containing ferroelectric and provide potential application opportunities of

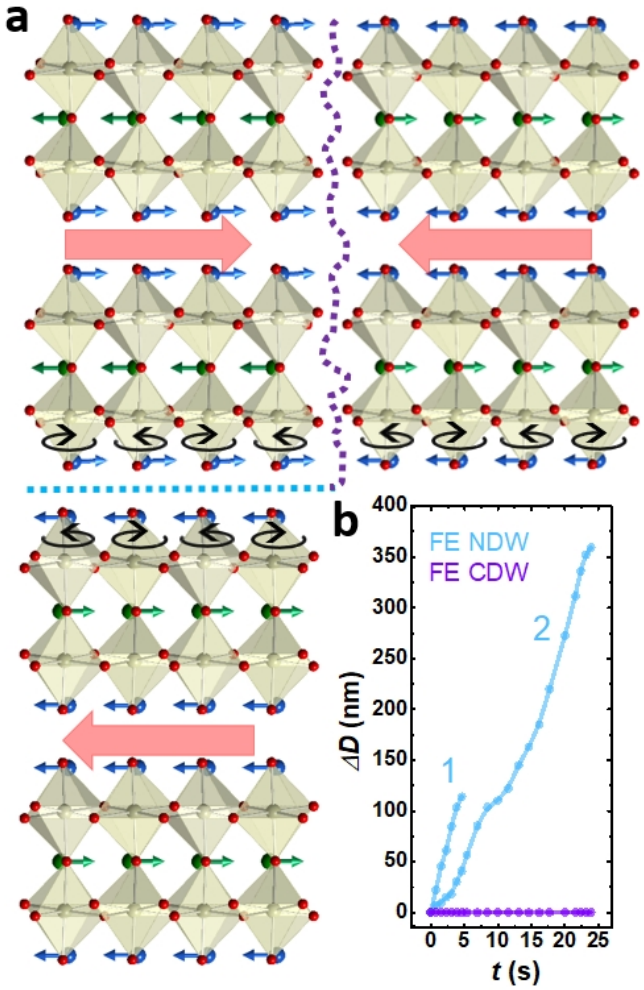

Figure 2.8: **Octahedral tilting distortions across different FE walls and the speed of FE wall moving.** (a) Octahedral tilting across the FE CDW(purple dotted line) and the FE NCW (blue dotted line). The red arrows indicate the bulk polarization in each domain. (b) Displacements of a FE CDW and 2 FE NDWs in Figure 2.7 (b-f) as a function of time after the focused beam was removed.

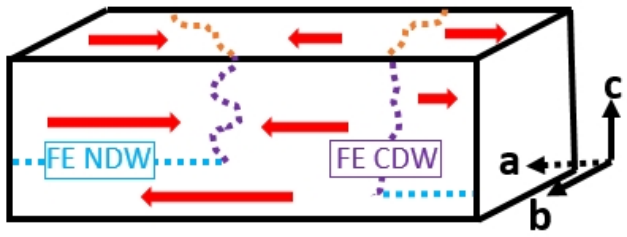

Figure 2.9: **A schematic diagram of the 3D FE domain configuration.**

it.

Chapter 3

Tunable ferroelastic domain walls in $Sr_3Sn_2O_7$ single crystals with low coercivity

3.1 Introduction

Recently, domain walls (DWs) in ferroic oxides possessing exceptional and distinct properties against the domain bulks, such as unusual electronic conductance [75–78], inseparably entangled spin and charge degrees of freedom [79–82], have attracted lots of attention. Due to these functional properties, such walls can serve as truly multifunctional quasi-2D objects, offering unprecedented degrees of freedom for the design of next-generation nanotechnology [83–87]. Comparing to the artificial interface (such as $LaAlO_3/SrTiO_3$) [88–90], which is difficult or even impossible to manipulate or alter once implemented into a material, DW in ferroic oxides is a nature type of homo-interface separating uniformly ordered crystal regions to reduce the average polarization and minimize the related depolarization field. These DWs can be modulated by external stimuli making them crucial importance for the polarization switching dynamics and the fatigue of ferroelectric devices [78, 91, 92]. Among them, charged DWs representing with emergent high conductivity has moved into focus and offers particular excitement, as new forms of devices can immediately be envisioned, in which function is entirely related to the presence or absence of conducting wall channels. Local diverging electrostatic potentials were created on the walls due to the existing of uncompensated positive or negative bound charges coming from electric polarization in different domains crossing the wall. These potentials require charge compensation that can e.g. be achieved by the redistribution of free carriers. In 1973, Vul and co-workers already discussed that a carrier density of up to $10^{14} cm^{-2}$ may emerge at head-to-head and tail-to-tail DWs in conventional ferroelectrics and enhance the conductivity [93]. The earliest experimental discoveries of charged DWs were reported in TGS (triglycine sulfate), $PbTiO_3$,

$BaTiO_3$ and $LiNbO_3$ in the 1960s and 1970s [94, 94–96], but the conductivity measurements did not provide the resolution to probe individual walls. Nowadays, the conductivity of each domain wall in these materials has been characterized using conductive atomic force microscopy (cAFM), scanning electron microscopy (SEM) and Cherenkov second harmonic generation (SHG) [43, 97–100]. Furthermore, people could successfully generate CDWs through external stimuli in $BaTiO_3$, $LiNbO_3$ and $KTiOPO_4(KTP)$, bringing us another step closer to the long-term goal of DWs based devices [101, 102]. However, all these processes include frustrated poling such as heating and applying large (long-time) voltage, which is not applicable to the real application. Moreover, the presence of CDWs is disfavored in the proper ferroelectric systems, which are driven towards a state with minimal strain mismatch between its ferroelectric/ferroelastic domains. As a result, CDWs in hybrid improper ferroelectrics, in which less rigid boundary conditions apply regarding the elastic and mechanical compatibility of DWs, has shed a light on the way. Experimental success in discovering CDWs in hybrid improper ferroelectric was achieved in $(Ca, Sr)_3Ti_2O_7$ [76], but there is no report on the modulation of these CDWs. Although the polarization switching coercive field, an important evaluation of the tunability, is 120-180 kV/cm in $Ca_{3-x}Sr_xTi_2O_7(x = 0, 0.54, 0.85)$ [76], 150 kV/cm in $Sr_3Sn_2O_7$ poly sample [103] and 75-160 kV/cm in $Ca_3(Ti_{1-x}Mn_x)_2O_7(x = 0, 0.05, 0.1, 0.15)$ [104], which is comparable to that of other proper ferroelectrics (200 kV/cm for $BaTiO_3$ films [105] and 140 kV/cm for $BiFeO_3$ films [27]), it's still difficult to be realized in applications. Therefore, finding a hybrid improper ferroelectric material with CDWs, which could be easily erased and regenerated with small coercivity, becomes of crucial importance not only for fundamental research but also for making tunable memristive devices of potential in applications.

3.2 Crystal growth

As we discussed in chapter 2, the difficulty of preparing $Sr_3Sn_2O_7$ is the evaporation of raw materials during the solid-sate reaction at very high temperatures. The embedding and sealing method was used to overcome this problem to make polycrystalline $Sr_3Sn_2O_7$ [103]. However, the growth of $Sr_3Sn_2O_7$ remains challenging and never be done before. Here, we report the first successful growth of $Sr_3Sn_2O_7$ single crystal using a laser floating zone

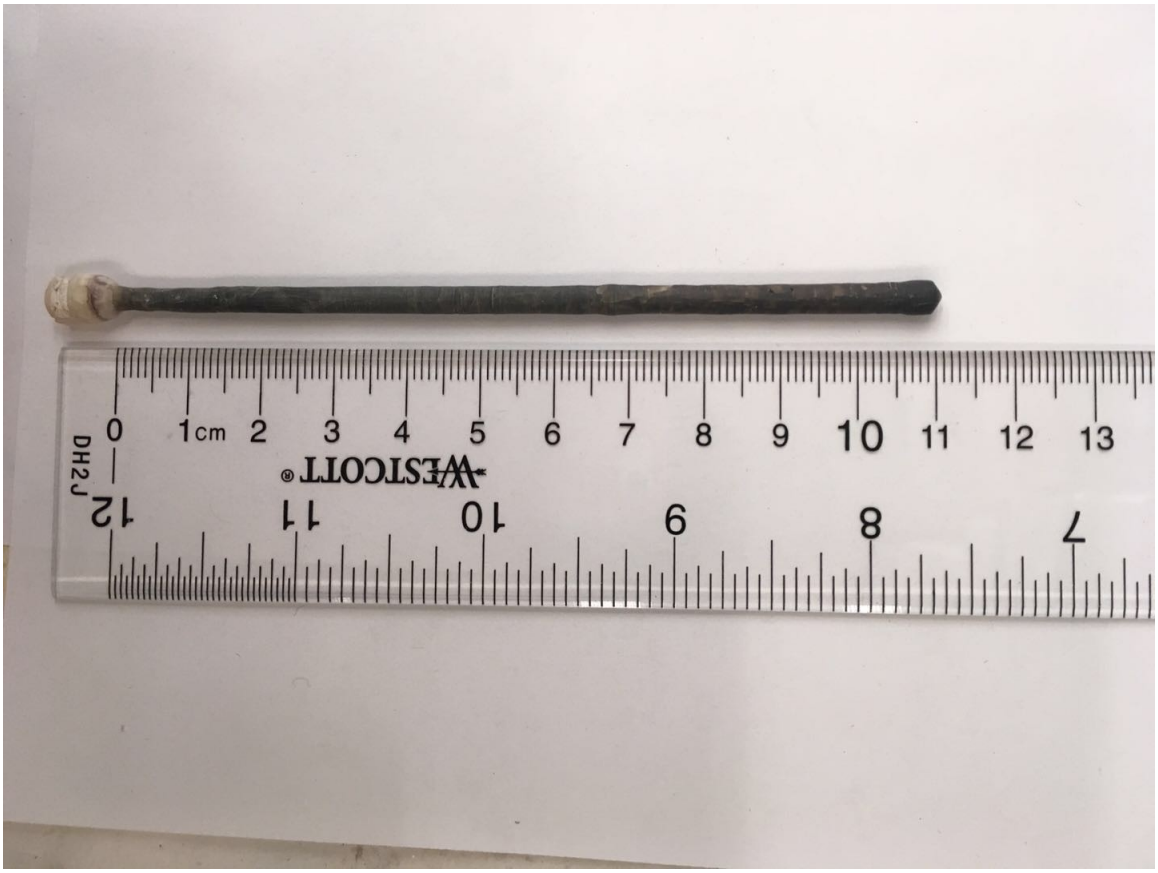

Figure 3.1: **A photograph of the as-grown $Sr_3Sn_2O_7$ single crystal boule.**

furnace, which has a well-focused laser beam on the melting zone and a steep temperature gradient at the interface between the liquid and solid. All these advantages comparing to optical floating zone furnace help to overcome the conflict between high melting temperature (over $2000°C$) and the serious evaporation of Sn. First, high-quality single phase $Sr_3Sn_2O_7$ poly samples are prepared using the method discussed in Chapter 2. For the feed rod, ground poly powders were pelletized into a uniform rod shape under 8000 PSI hydro-static pressure and sintered at $1400°C$ for 10 hours. The crystal was grown at the speed of 30 mm/hour in a 0.9 Mpa O_2 atmosphere. The as-grown single crystal boule, as shown in Figure 3.1, was annealed at $1400°C$ for 20 hours, followed by a $50°C/hour$ cooling in O_2 flow.

3.3 Polarization hysteresis loop with small coercive field

In $Sr_3Sn_2O_7$, the net bulk polarization is along the $a-axis$ which is from the Sr displacements induced by the combination of SnO_6 octahedra in-phase rotation around the $c-axis$ ($a^0a^0c^+$) and out-of-phase tilting around the orthorhombic $b-axis$ ($a^-a^-c^0$), as shown in Figure 3.2 (a) and (b). The orthorhombic structural distortions in $Sr_3Sn_2O_7$ result in orthorhombic twins. Same with previous reports on the polycrystalline $Sr_3Sn_2O_7$ specimen, these twin domains can be observed in TPOM images on a cleaved surface perpendicular to the crystallographic $c-axis$, as shown by the dark-bright contrast in Figure 3.4 (b). This cleaved thin piece is transparent, consistent with the reported large magnitude (4.13 eV) of the optical gap [2]. Two samples were prepared for the polarization (P) versus electric field (E) hysteresis loop measurements: one was polished along the twin boundaries so that the electric fields can be applied along the [110] direction; the other one was polished 45° with the twin boundaries so that the electric fields can be applied along the [100] ([010] in nearby twin domains) direction. Figure 3.2 (c) shows the room-temperature $P(E)$ loops measured in oil at frequency $f = 270HZ$ using the positive-up-negative-down (PUND) method to get rid of leakage and capacitance contribution. The net remanent electric polarization along the [100] direction is $1.53\mu C/cm^2$, which is about $\sqrt{2}$ times of that along the [110] direction ($1.15\mu C/cm^2$). This measured remanent polarization is smaller than the theoretically calculated value [47], indicating smaller Sr displacement in the real material. This is an evidence of that both 90° and 180° polarization flipping happens when the external electric field is applied along the [100] direction, which is an indication of the erase of FA DWs. The compensated current density versus electric field, $J(E)$, curves are shown in Figure 3.3. The polarization switching coercive field corresponding to the peak position of the $J(E)$ curve at room temperature is $39kV/cm$ along the [100] direction and 47 kV/cm along the [110] direction, which is the smallest among all experimental discovered bulk hybrid improper ferroelectrics to our knowledge. Figure 3.2 (f) shows the normalized $P(E)$ loops of $Sr_3Sn_2O_7$ single crystal (blue along [110] and red along [100]), $Ca_3Ti_2O_7$ single crystal (yellow, along [110]) and $Sr_3Sn_2O_7$ poly sample (black). We can clearly see how small the coercive field in $Sr_3Sn_2O_7$ single crystal comparing to other most-studied bulk

HIFs. Moreover, a weak anomaly is observed in the resistivity (ρ) vs. temperature (T) measurements shown in Figure 3.2 (e), which corresponds to a structural transition from low temperature $A2_1am$ to high temperature $I4/mmm$. The transition temperature can be identified from the peak position in the $d(log(\rho(T))/dT$ curves, shown in Figure 3.3.

3.4 Tunable ferroelastic domain walls under stress

Since the polarization switching coercive field is small in $Sr_3Sn_2O_7$ single crystal, it would be quite interesting to study the stress effect. The schematic geometry of our experiment is shown in Figure 3.4 (a). A thin $a-b$ plane cleaved piece is polished to a square shape with boundaries along the crystallographic [100] and [010] directions. Then it is annealed at 1450°C followed by 100° C/hour cooling to remove any induced strain during polishing. Four glass bars shown by grey cuboid in Figure 3.4 (a) are used to apply uniform stress along the [100] and [010] directions, respectively. The bright-dark contrasts in Figure 3.4 (b) represent the distribution of ferroelastic (FA) domains in the initial state. Figure 3.4 (c) shows the TPOM image recorded after the application of uniaxial stress along the direction 45C with the FA DWs, which is indicated by the blue arrows. During the process, the FA domains with polarization parallel to the strain, which will be proved combining with PFM images later, is shrunken and erased to get a single FA domain state. Then a 90° rotated stress is applied, as shown by the blue arrows in Figure 3.4 (d, e), the FA domains with polarization perpendicular to it can be re-generated and expanded. Figure 3.4 (f) shows crystallographic cartons of the $a-b$ plane $Sr_3Sn_2O_7$, blue (green) arrows indicate the Sr atoms' displacements along the orthorhombic [100] direction and black dotted lines represent the FA domain walls. The dark (light) yellow dotted line indicates the longer $a-axis$ (shorter $b-axis$). The FA domains with polarization perpendicular to the stress will be expanded since the shorter orthorhombic $b-axis$ is preferred along the stress direction and the electric polarization is along the longer orthorhombic $a-axis$. In a conclusion, stress can erase (shrink) FA domains with electric polarization parallel to it and re-generate (expand) FA domains with electric polarization perpendicular to it.

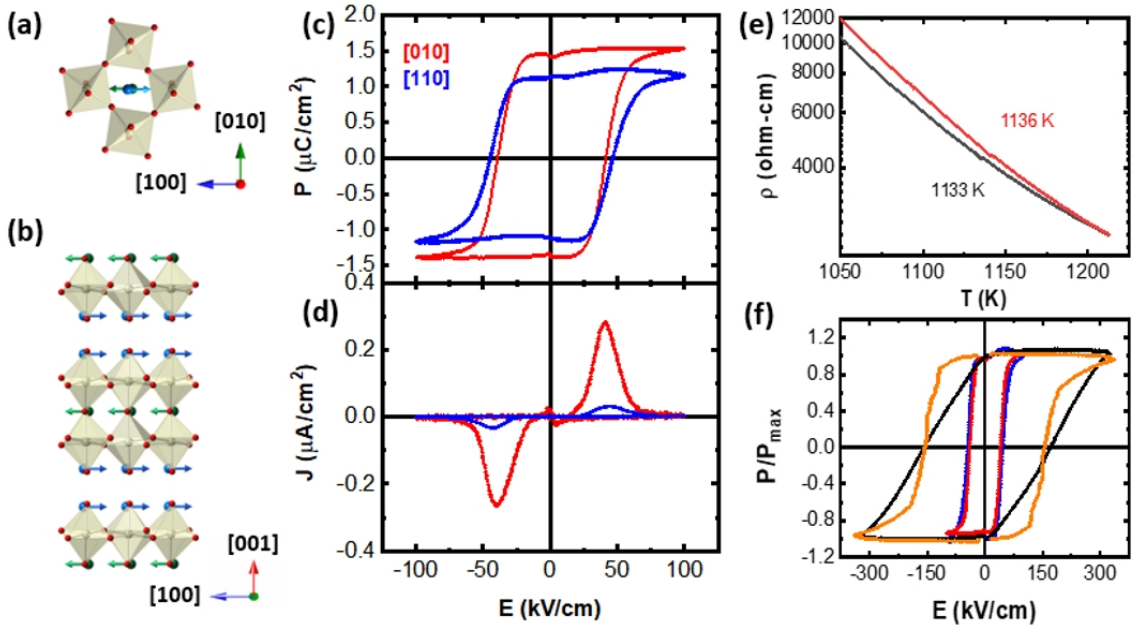

Figure 3.2: **Switchable electric polarization at room temperature with smallest coercive field among all HIF bulk materials.** (a,b) The $c-direction$ and $b-direction$ views of the ferroelectric $a^-a^-c^+$ distortions in $Sr_3Sn_2O_7$. The green and blue arrows represent Sr antipolar displacements along the $a-axis$ in the perovskite block and rocksalt block, respectively. The red (grey) dots depict oxygen (Sn) atoms. (c, d) Electric polarization (P) and compensated current density (J) versus electric field (E) hysteresis loop of a $Sr_3Sn_2O_7$ single crystal, measured along two different crystallographic directions with a PUND method in oil at frequency $f = 270HZ$. The electric field was applied parallel (45°) with the twin boundaries for the measurement represented by the blue (red) curve. (e) High-temperature resistivity (ρ) as a function of temperature (T) measured using four-probe methods. The current was applied in the $a-b$ plane along the structural twin boundaries. The red (black) curve represents the data taken during the heating (cooling) process with a sweeping rate of $5°C/minute$. (f) The normalized $P(E)$ loops of $Sr_3Sn_2O_7$ single crystal (blue along [110] and red along [100]), $Ca_3Ti_2O_7$ single crystal (yellow, along [110]) and $Sr_3Sn_2O_7$ poly sample (black).

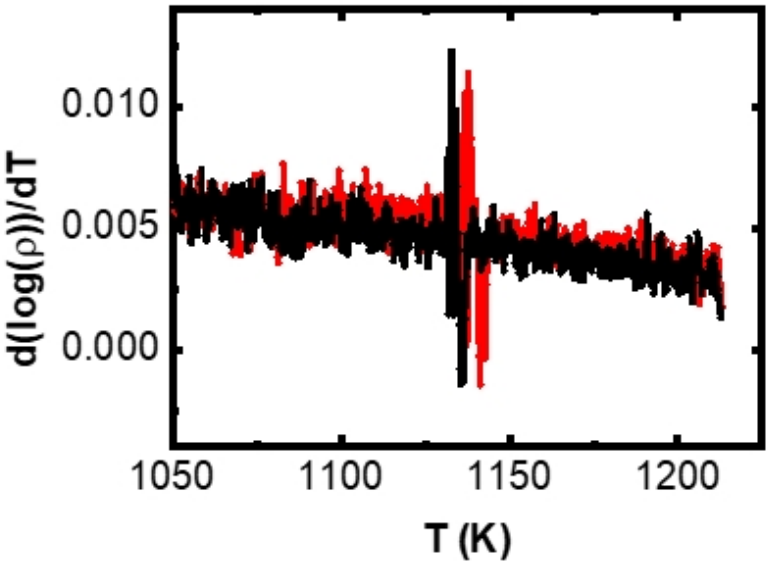

Figure 3.3: **The derivative of $log(\rho(T))$ to T.** The $\rho(T)$ was shown in Figure 3.2 (e). The red (black) curve records the data during warming (cooling). The temperature sweeping rate is $5^{\circ}/minute$.

3.5 Ferroelectric domain patterns and charged domain walls

The intriguing polarization direction in each FA domain is defined by in-plane piezo-response force microscope (IP-PFM) images. Figure 3.5 (a) and (b) present the IP-PFM images with cantilever 90° to each other of the region bounded by red rectangular in Figure 3.4 (e). The straight boundaries are FA DWs, which are identified as orthorhombic twin boundaries in the TPOM images shown in Figure 3.6 (c). The direction of planar polarization can be determined and presented by the while (black) arrows since only polarization perpendicular to the scanning cantilever can be detected. Figure 3.5 (c) shows the schematic of polarization domains obtained from both horizontal and vertical IP-PFM images.

Moreover, we want to study the effect of uniaxial stress on the ferroelectric-ferroelastic domains. Figure 3.6 (a-c) show the TPOM images taken from the squared region in Figure 3.4 (c-e). Under the stress indicated by the blue arrows, one FE domain is generated and expanded. If we apply larger stress along the same direction, this new generated FE domain will finally expand to the whole region and erase the previous dominated FE domain. Figure 3.6 (e-g) shows the IP-PFM images on the same region at different states corresponding

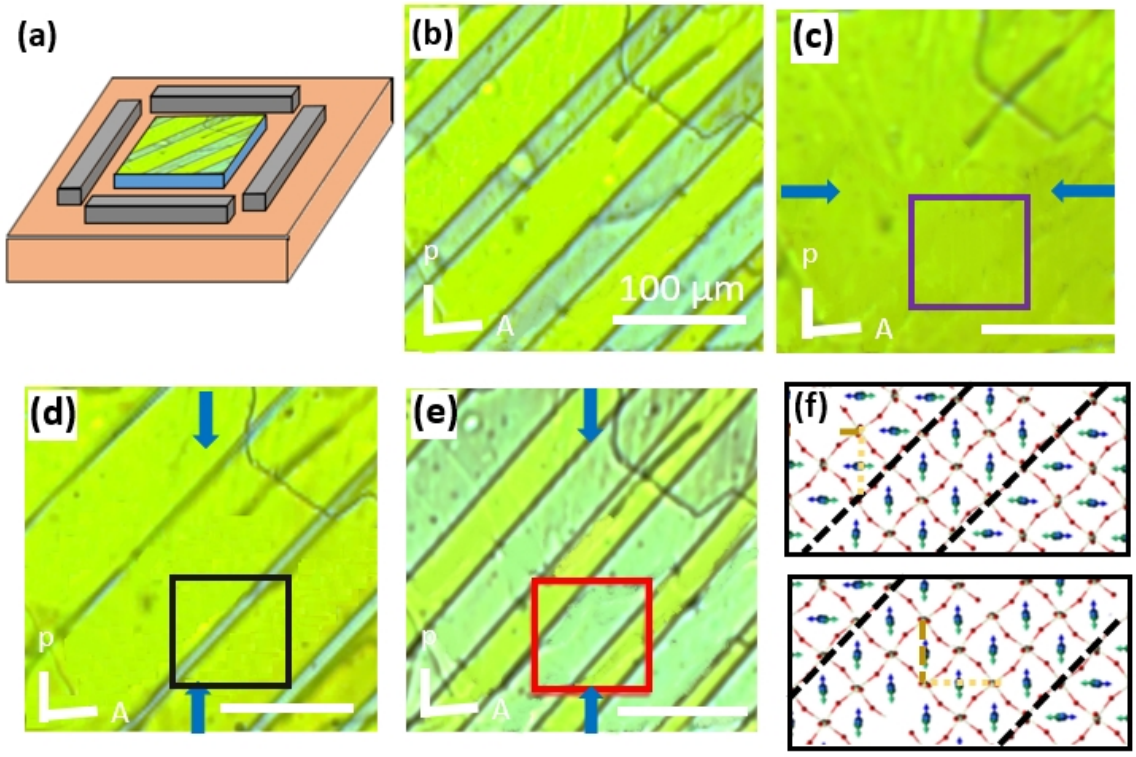

Figure 3.4: **Erase and re-generate orthorhombic twins in $Sr_3Sn_2O_7$ single crystal.** (a) A schematic geometry of the experiment. One $a-b$ plane cleaved thin piece is polished into a square shape with boundaries along the crystal [100] ([010]) directions. (b-e) Transmission polarized optical microscope (TPOM) images of it. The dark-bright contrast in (b, d, e) indicates the orthorhombic twin domains. (b) is the initial state and (c-d) present the evolution of twin domains under two different direction uniaxial stress, as shown by the blue arrows in each figure. The colorful squares in (c-e) indicate the corresponding scanned regions, whose PFM images will be shown in Figure 3.5. In (b-e), the white bar with P (A) presents the direction of the polarizer (analyzer). (f) $a-b$ plane crystallographic cartons, the black dotted lines indicate the ferroelastic domain walls. The blue (green) arrows indicate the atom displacement in different domains. The dark yellow (light yellow) dotted lines indicate the longer (shorter) orthorhombic $a-axis$ ($b-axis$).

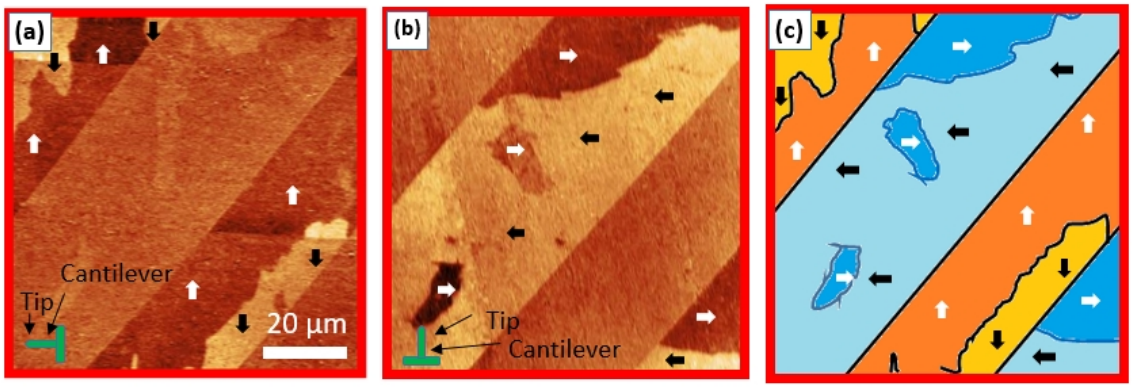

Figure 3.5: **Observation of ferroelectric-ferroelastic domains.** (a-b) In-plane piezo-response force microscope (IP-PFM) images of the cleaved (001) surface of $Sr_3Sn_2O_7$ crystal at room temperature. Orthorhombic twin boundaries are oriented along the diagonal direction of the xy scanning axes. In (a) and (b), the long axis of the AFM cantilever is oriented along the horizontal and vertical direction respectively, as shown by the carton on the left bottom corner. (c) Illustration of polar domains in $80\mu m \times 80\mu m$ area, obtained from (a) and (b). The black and white arrows in (a-b) indicate the direction of the electric polarization inside each domain.

to the TPOM images in (a-c). The white and black arrows present the polarization direction in each domain. Figure 3.6 (f-g) are from the combination of two IP-PFM images, as explained in the caption of Figure 3.5. From the evolution of ferroelectric-ferroelastic domains, we can find the major effect of the stress is to induce 90° polarization switching instead of 180° switching. This is different to that in the electric field poling process: only domains with polarization along the field direction is preferred. Furthermore, from the symmetry analysis, there is no energy difference between +90° and −90° polarization switching, which can be proved by the random distribution of FE domains in the new generated FA regions, see Figure 3.6 (e-g).

The density of bounded charges on each FE and FA DW is associated with the angle between polarization in the adjacent domains and also the normalized vector of the wall. There are four kinds of charge FA DWs, head-to-head, tail-to-tail, head-to-tail with anticlockwise rotation and head-to-tail with the clockwise rotation as shown by the carton on the top of Figure 3.6 (d). The corresponding charge densities are $\sqrt{2}P$,$-\sqrt{2}P$, 0 and 0, respectively. Since there are two island FE domains with smoothly curved boundaries in Figure 3.6 (g), the charge density on FE DWs will vary continuously from $2P$ (in red) to $-2P$ (in green) as shown in the schematic picture on the bottom of Figure 3.6 (d). The charge density of

ing

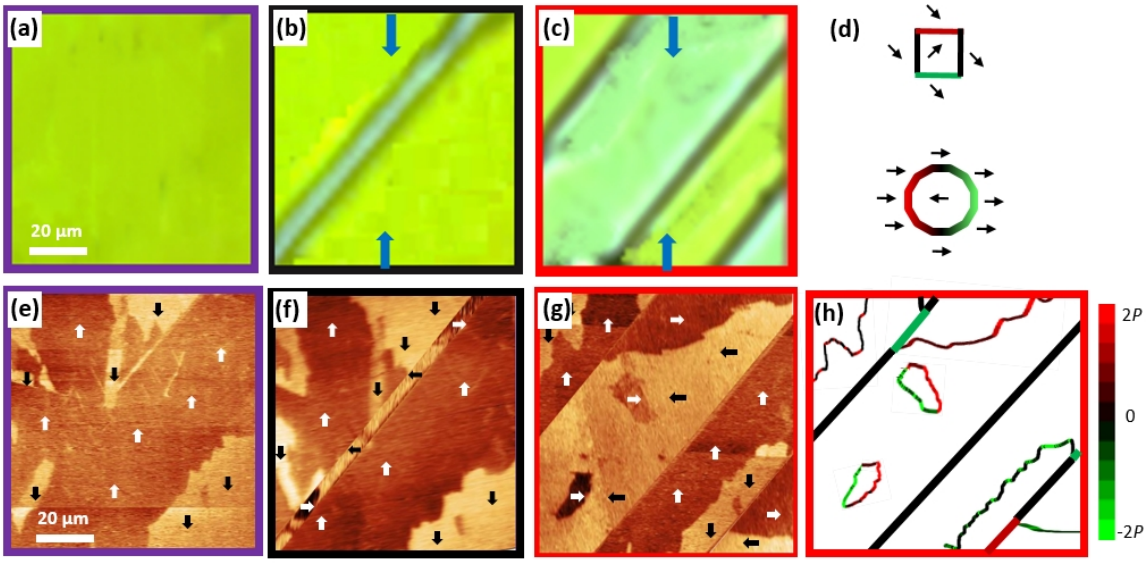

Figure 3.6: **Effect of stress on ferroelectric-ferroelastic domains and charged domain walls.** (a-c) TPOM images of the squared regions in Figure 3.5 (c-e). (e-g) The corresponding IP-PFM images with white and black arrows indicate the polarization direction in each domain. (h) A schematic picture depicts the density of bound charges of all the FA DWs and FE DWs in (g). For the FA DWs, there are found different DWs with three different charge density (0, $\pm\sqrt{2}P$) as shown by the top figure in (d). For FE DWs around the two island FE domains in (g), the charge density change continuously from $2P$ to $-2P$. The bottom picture in (d) depicts possible charge density of FE DWs with respect to the polarization direction (black arrows). The boundary color in (d) is consistent with the color bar in (h), representing the charge density from $2P$ to $-2P$.

each FA and FE DWs extracted from Figure 3.6(g) is shown in Figure 3.6(h). These various charge densities of FE DWs offer a great opportunity for application as electronic devices.

3.6 Summary and outlook

In summary, we report the first successful growth of $Sr_3Sn_2O_7$ single crystal using laser floating zone furnace representing the smallest polarization switching coercive field ($39kV/cm$ along [100] and $47kV/cm$ along [110]) at room temperature among all discovered bulk hybrid improper ferroelectrics. Due to the small switching barrier, we could observe the erasing and re-generation of ferroelastic domains. The stress can erase (shrink) FA domains with polarization parallel to it and re-generate (expand) FA domains with polarization perpendicular to it since the shorter orthorhombic $b-axis$ is preferred to be aligned along the stress while the polarization is along the longer $a-axis$. Moreover, the ferroelectric polarization direction in each FA and FE domain is determined from in-plane piezo-response microscope images. We also present the density map of bounded charge for four types of FA DWs and continuous changed FE DWs. The charge density varies from $2P$ to $-2P$. Our discoveries reveal the smallest coercive field among all bulk HIFs and reproducible erase (re-generate) of FE domains and charged FA (FE) DWs, which provides new insights and application opportunities of HIFs in functional electronic devices.

Chapter 4

Polar magnets: $M_2Mo_3O_8$ (M=Fe, Mn, Ni, Co, Zn)

4.1 Introduction

Materials belonging to the polar crystallographic symmetry groups lack the inversion symmetry at all temperatures. Many of these materials contain magnetic ions, and they often exhibit long-range magnetic order, which are called "polar magnets" [106]. The prerequisite for non-trivial magnetoelectricity is the simultaneous breaking of time reversal symmetry and space inversion symmetry. Thus, all polar magnets should exhibit non-trivial ME effects below magnetic ordering temperatures. Importantly, no poling procedures are needed to reveal the ME response on monodomain single crystals of polar magnets. While the polar magnets are numerous, the investigation of their magnetoelectricity has been extremely limited. The few examples of polar magnets whose magnetoelectricity has been studied include $GaFeO_3$ [107] and Ni_3TeO_6 [108]. In Ni_3TeO_6, people found a change of electric polarization at the onset of the AFM ordering (T_N=52 K), which was explained by the magnetic exchange striction. Moreover, they found that in the external magnetic fields along the c axis, the spin-flop is initiated at a second-order phase transition and proceeds through a narrow intermediate state, giving rise to colossal responses in ferroelectrics. This intermediate spin state in Ni_3TeO_6 results in a non-hysteresis ME effect. Furthermore, the magnetization is linearly controlled by an electric field without hysteresis in the intermediate state of a spin-flop transition. All these findings on polar magnets may open a new path to the realization of practical ME devices with high tunability and good retention. However, the strongest mutual control of magnetization and electric polarization can only be revealed after ME poling. Finding new polar magnets with colossal ME coefficients lacking this drawback is of primary importance for prospective applications.

The mixed oxides $M_2Mo_3O_8$, where M is a magnetic transition metal, were first synthesized by McCarroll et al. in 1957 [109]. They primarily studied the crystal structures. In 1972, the magnetism was introduced by Varret et al. [110] in powder samples using the Mossbauer effect. Later on, Bertrand and Kerner-Czeskleba [111] briefly showed some magnetic data and proposed the possible magnetic structures for the materials based on powder neutron diffraction data. In 1983, S.P. McAlister and P. Strobel [11] show a systematic study of the magnetic structure of this system. They pointed out the ground state of $Fe_2Mo_3O_8$ and $Co_2Mo_3O_8$ are antiferromagnetic, $Mn_2Mo_3O_8$ is ferrimagnetic, $Zn_2Mo_3O_8$ is diamagnetic and $Ni_2Mo_3O_8$ is paramagnetic.

4.2 Crystal structure and sample growth

$M_2Mo_3O_8$ (M=Fe, Mn, Ni, Co, Zn) single crystals were grown using a chemical vapor transport (CVT) method at 1000°C for 10 days, followed by furnace cooling. The single crystals are black hexagonal plates with typical size $\sim 1\times1\times0.5mm^3$, as shown in Figure 4.1(d). The flat hexagonal top surface is (001). Powder X-ray diffraction measurement was performed on crushed powders of them. Refinements show that the room-temperature space groups are all $P6_3mc$. a- and c- lattice constants are shown in Table 4.1, which is similar to the published data. [11]

M	a	c
Mn	5.794 (2)	10.256 (4)
Fe	5.773(3)	10.054(3)
Ni	5.757(2)	9.858(3)
Co	5.767(1)	9.914(3)

Table 4.1: a- and c- lattice constants in $M_2Mo_3O_8$. All distances in Å.

$M_2Mo_3O_8$, known as the mineral kamiokite, consists of honeycomb-like M-O layers separated by sheets of M^{4+}, see Figure 4.1(a). The layers are stacked along the c axis. The M-O layer is formed in the ab plane by corner-sharing MO_4 tetrahedron and MO_6 octahedron, as shown in Figure 4.1(c). In this layer, the tetrahedral(M_t) and octahedral(M_o) triangular sublattices are shifted along the $c-axis$ (0.614 Å in $Fe_2Mo_3O_8$ [112]) with respect to each other, leading to short and long interlayer M-M distances, see Figure 4.1(a). The

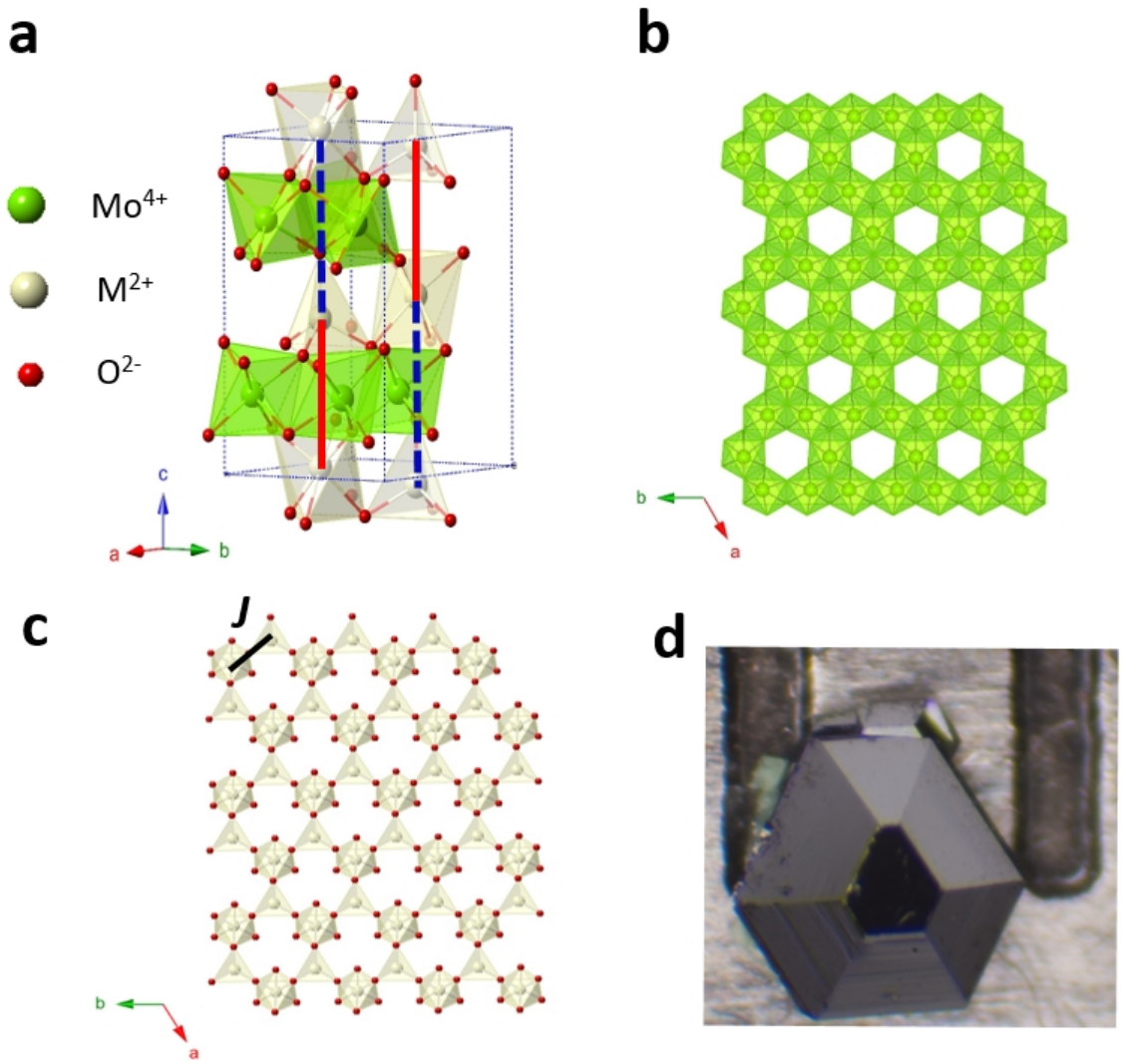

Figure 4.1: **Crystal structure and optical images of $M_2Mo_3O_8$** (a) Crystal structure of $M_2Mo_3O_8$. Vertical lines connect the nearest M ions along the c axis (blue lines are longer than the red ones). (b) The Mo-O layer in the ab crystallographic plan. This Mo kagome-like layer is trimerized. The Mo trimers are in the singlet state. (c) The M-O layer in the ab crystallographic plane. Thick line depicts the largest M-M magnetic coupling J. (d) Optical image of a piece of $Fe_2Mo_3O_8$. The distance between the two lines on the ruler is 1mm.

vertices of the MO_4 tetrahedra point along the positive c axis, reflecting the polar structure of $M_2Mo_3O_8$. [11, 112] The Mo kagome-like layer is trimerized, as shown in Figure 4.1(b). The Mo trimers are in the singlet state and do not contribute to magnetism. [11, 111, 113]. The magnetic ground state of $M_2Mo_3O_8$ are different depending on the M. S.P. McAlister and P. Strobel [11] pointed out the ground state of $Fe_2Mo_3O_8$ and $Co_2Mo_3O_8$ are antiferromagnetic, $Mn_2Mo_3O_8$ is ferrimagnetic, $Zn_2Mo_3O_8$ is diamagnetic and $Ni_2Mo_3O_8$ is paramagnetic.

4.3 Hidden ferrimagnetism and giant magnetoelectricity in $Fe_2Mo_3O_8$

For the ME device applications, ferro- or ferrimagnetic polar magnets are some of the best candidates, as the macroscopic magnetic moment is needed for their functionality. Such compounds are rare. However, in some cases macroscopic magnetic moment is "hidden" within a nominally antiferromagnetic state, and can be easily revealed in a modest applied magnetic field, thereby leading to a potentially large ME response. A well-known example of such a hidden moment is realized in Lu_2CuO_4, the parent compound of high-T_c cuprate superconductors. [114] Each Cu-O plane exhibits a weak ferromagnetic moment due to canting of the spins of the otherwise regular Neel order. The canting results from Dzyaloshinsky-Moria interaction. Weak ferromagnetism is masked in zero magnetic field because of the antiferromagnetic interplane coupling. However, spin canting is responsible for the many distinct magnetic properties of this compound, including the unusual shape of the magnetic susceptibility in the vicinity of T_N and in an applied field, and the atomic-scale giant magnetoresistance in the field-induced weakly ferromagnetic phase. Another layered magnet in which a small ferrimagnetic moment of each layer is hidden in zero field is multiferroic (but nonpolar at high T) $LuFe_2O_4$ [115]. The giant magnetic coercivity and the unusual ME relaxation properties of $LuFe_2O_4$ are related to the ferrimagnetism in its Fe-O layers. Similar to these compounds, a hidden magnetic moment in a polar magnet could result in a strongly enhanced magnetic response, which should lead to large ME effects when the magnetic moment and crystal structure are coupled.

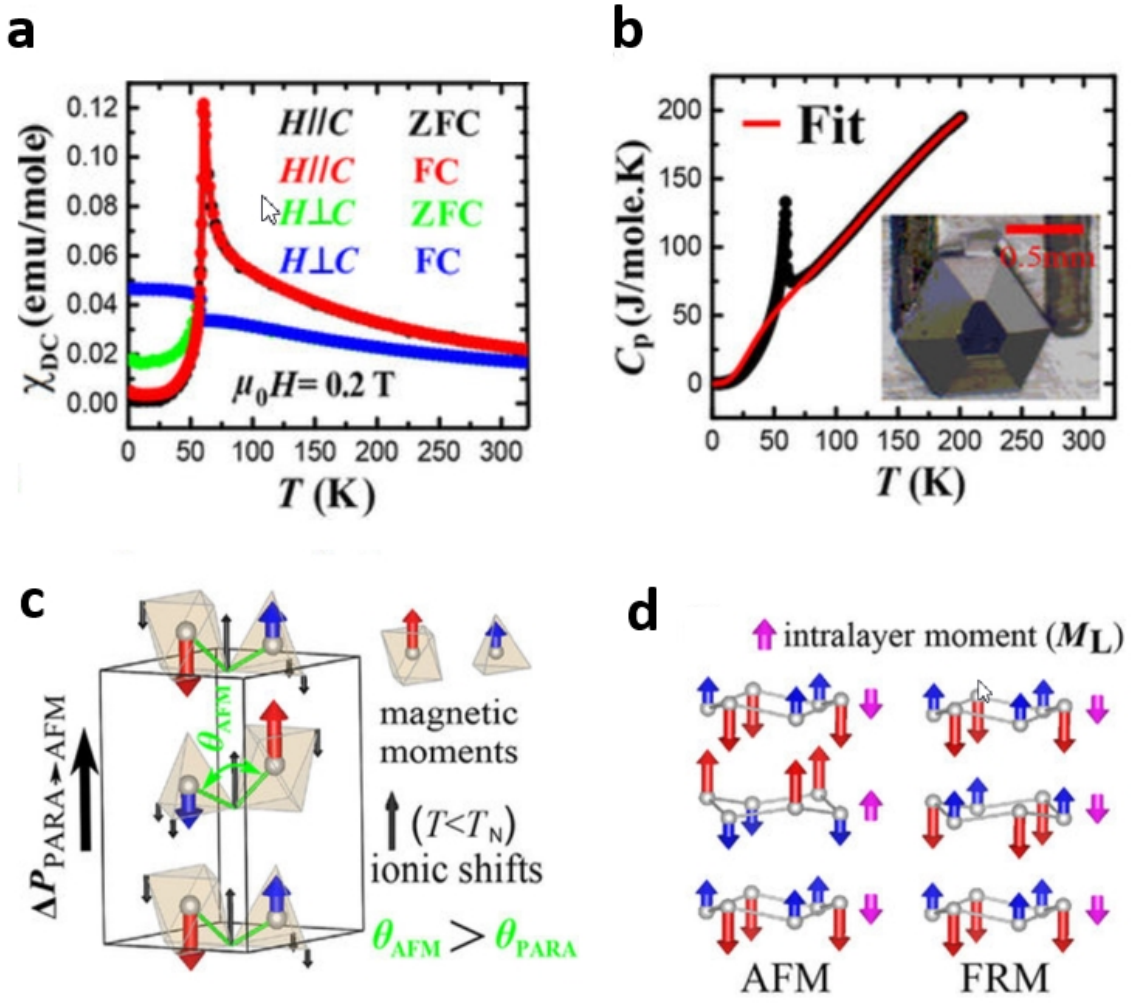

Figure 4.2: **Magnetic susceptibility, heat capacitance and spin configuration of $Fe_2Mo_3O_8$, which is from rearrangement of figures in reference [3]** (a) Temperature dependence of DC magnetic susceptibility χ_{DC} in zero field-cooled (ZFC) and field-cooled (FC) processes along two crystallographic directions, parallel and perpendicular to the c axis, in $\mu_0 H$=0.2T. (b) Specific heat anomaly at the Neel temperature. Red line represents the double Debye model fit discussed in the text. Insert: the image of as-grown Fe_2Mo_3O8 single crystal. (c) The AFM order, together with the calculated largest ionic shifts associated with the paramagnetic to AFM transition. The direction of the magnetically-induced ΔP is shown with a thick arrow. (d) Schematic view of the AFM and FRM orders. Pink arrows represent the ferrimagnetic moments of the individual Fe-O layers.

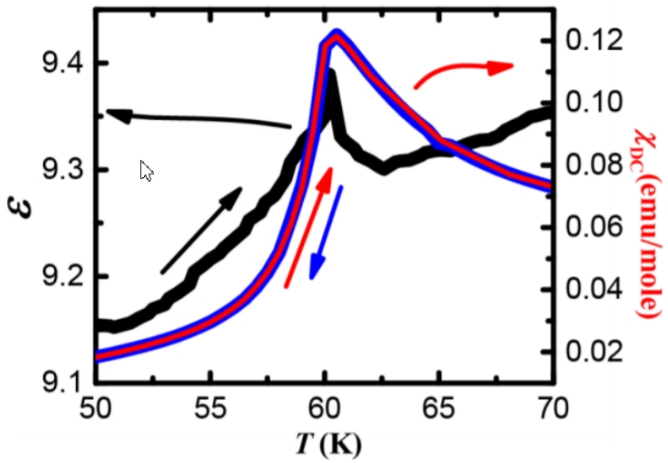

Figure 4.3: **Dielectric $\varepsilon(T)$ and magnetic $\chi_{DC}(T)$ susceptibilities in the vicinity of T_N, which is from reference [3].** The magnetic susceptibility was measured on cooling in applied magnetic field H=0.2 T(blue line), and on subsequent warming in the same field (red line).

4.3.1 Antiferromagnetic ground state

Herein, in $Fe_2Mo_3O_8$ the Fe^{2+} moments exhibit the antiferromagnetic(AFM) order in the honeycomb layers below $T_N \approx$60K. As discussed below, Fe_O has larger spin than Fe_t, and therefore each of the Fe-O layers is ferrimagnetic.[110]. Along the c axis, the nearest Fe spins are aligned in the same direction, implying ferromagnetic interlayer coupling. The resulting stacking of ferrimagnetic Fe-O layers along the c axis leads to vanishing macroscopic magnetic moment, and we call this state AFM. The temperature variation of DC magnetic susceptibility χ in zero field-cooled (ZFC) and field-cooled (FC) processes is shown in Figure 4.2(a) for the magnetic field both parallel and normal to the c axis. The shapes of the curves are consistent with the transition to the AFM order shown in Figure 4.2(d) at T_N=61K, with Fe^{2+} spins pointing along the c axis. The large difference between the c-axis and in-plane susceptibilities in the paramagnetic state demonstrates appreciable anisotropy of the Fe^{2+} spins. No thermal hysteresis is observed, see Figure 4.3.

4.3.2 Structural transition associated with the magnetic order

A large specific heat (C_p) anomaly is present at the magnetic transition, see Figure 4.2(d). To account for the phonon part, the specific heat was fit to a double Debye model for

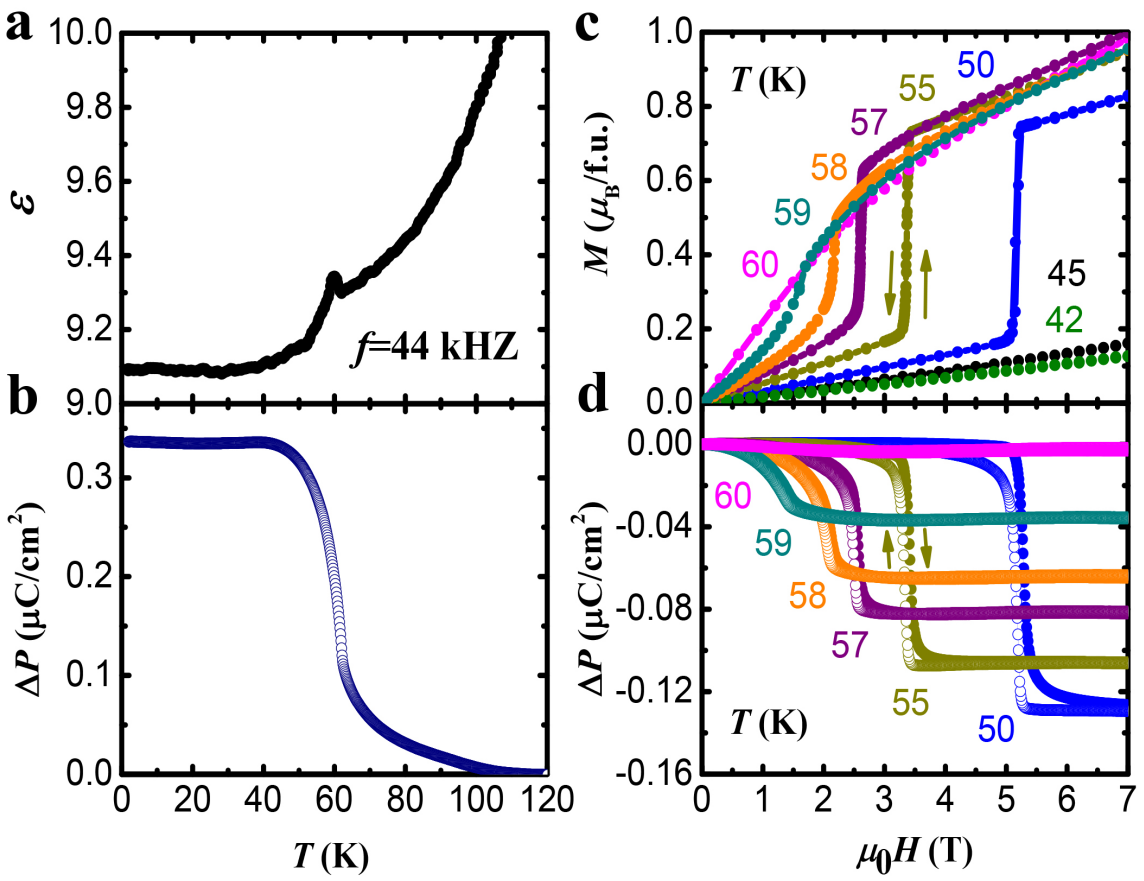

Figure 4.4: **Magnetically-induced electric polarization, and the metamagnetic transition, which is from reference [11].** (a) Temperature dependence of the c-axis dielectric constant $\varepsilon(T)$, f=44 kHZ. (b) Variation of the c-axis electric polarization ΔP with temperature. (c,d) Magnetic field dependence of magnetization $M(H)$ and polarization $\Delta P(H)$ at various temperatures. In (d), solid (open) circles depict the data obtained upon sweeping the magnetic field up (down).

$T > T_N$ (90 to 200 K). The best fit, shown in Figure 4.2(b), was obtained for the Debye temperatures $\theta_{D1} = 174$ K and $\theta_{D2} = 834$ K. It fails for $T < T_N$ as it implies a negative magnetic contribution for $T < 50$ K. This indicates an additional lattice contribution for these temperatures, suggesting a structural transition associated with the magnetic order. This suggestion is corroborated by the temperature dependence of the dielectric constant $\varepsilon(T)$ and the variation of electric polarization $\Delta P(T) = P(T) - P(T = 120K)$, both along the c axis, shown in Figure 4.4 (a,b).

In particular, the jump of ΔP at T_N clearly indicates simultaneous magnetic and structural transitions. The magnitude of this jump, $\sim$0.3 μC/cm^2, is larger than the values

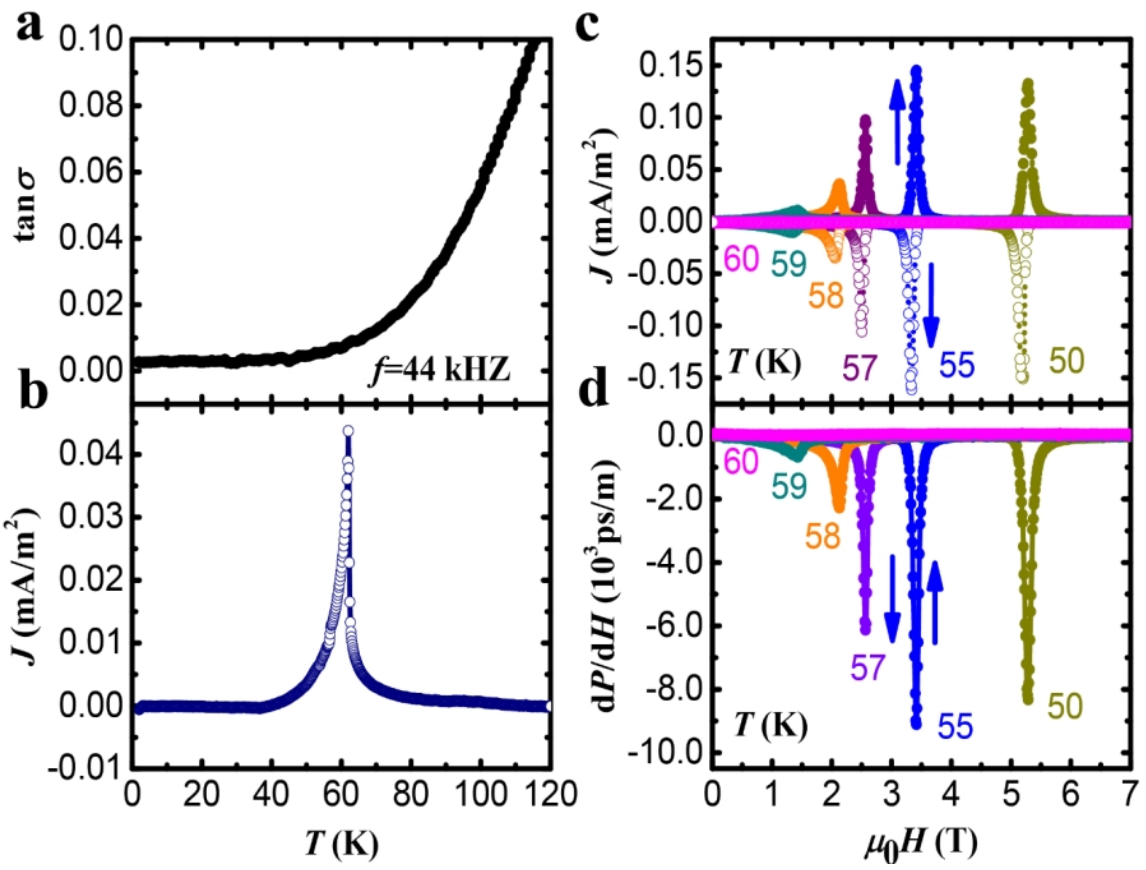

Figure 4.5: **Pyroelectric current density, magneto-current, and the differential ME coefficient dP/dH at different temperatures, which are from the supplementary information of reference [3]** (a) Loss tangent as a function of temperature. (b) Pyroelectric current density as a function of temperature, measured upon warming. (c) Isothermal magnetocurrent as a function of magnetic field. (d) Differential magnetoelectric coefficient dP/dH calculated using the data shown in panel (c). Arrows indicate the field sweeping direction. All the measurements are along the crystallographic c axis.

typically observed in multiferroics and is the largest measured value in polar magnets, to our knowledge. Importantly, no poling is needed in an already polar material to observe the change shown in Figure 4.4 (a,b). In particular, ΔP was measured by integrating the pyroelectric current on warming after cooling down to T=5 K in zero electric field. The pyroelectric current density as a function of sweeping temperature was shown in Figure 4.5(b). In our measurements, the direction of the ΔP vector (along or opposite to the positive direction of the c axis defined above) is undetermined. First-principles calculations described below indicate that ΔP points in the positive c direction, hence we adopt this convention here.

4.3.3 Magnetically-induced electric polarization and metamagnetic transition

Knowing the co-existence of magnetic ordering and structural transition at the same temperature $T = T_N$, studying the possible coupling between them becomes crucial interesting.Performing magnetoelectric measurements, it was found that magnetic field (H) induces a metamagnetic transition signaled by sharp magnetization (M) jump, see Figure 4.4(c). It is accompanied by a structural transition indicated by the corresponding jumps in the electric polarization, as shown in Figure 4.4(d). A small hysteresis is observed in the latter transition. The $\Delta P = P(H) - P(H = 0T)$ vector is in the negative c axis direction, and its value at T=50 K is roughly twice as small as the ΔP induced at T_N for H=0 T. No poling of any kind is needed. In the FRM state, the ferrimagnetic moments of the Fe-O layers are co-aligned, giving rise to a macroscopic magnetization. The extrapolation of the high-field $M(H)$ data of Figure 4.4(c) to zero field gives a positive intercept of $\approx 0.5\mu_B/f.u.$ at T=50 K, indicating the ferrimagnetic character of the high-field state, which we assume to have the same FRM structure as shown in Figure 4.2(d). This assumption is corroborated by the Fe-O net ferrimagnetic moment of $0.6\mu_B/f.u.$ for a single layer, expected from the Moessbauer measurements of the Fe_O and Fe_t moments[110] (4.83 μ_B and 4.21 μ_B, respectively), as well as by the results of the first principles calculations described below.

4.3.4 Magnetoelectric effect and the associated ionic shifts

To understand the microscopic origin of the observed ME effects, we have carried out ab-initio calculations in the framework of density functional theory adding an on-site Coulomb self-interacting potential U (DFT+U). For the DFT part, the generalized gradient approximation Perdew-Burke-Ernzerhof (GGA-PBE) functional was used. For U=0, the ground state is metallic with the FRM structure, but moderate correlation strength (U=4 eV) leads to an AFM insulating ground state. While U of the order of 4 eV is required to obtain the correct ground state, its exact value was found to be unimportant for the magnetic exchange energies relevant to this work. The details of the DFT calculations can be found in Appendix B. The ionic positions were optimized for two imposed magnetic structures,

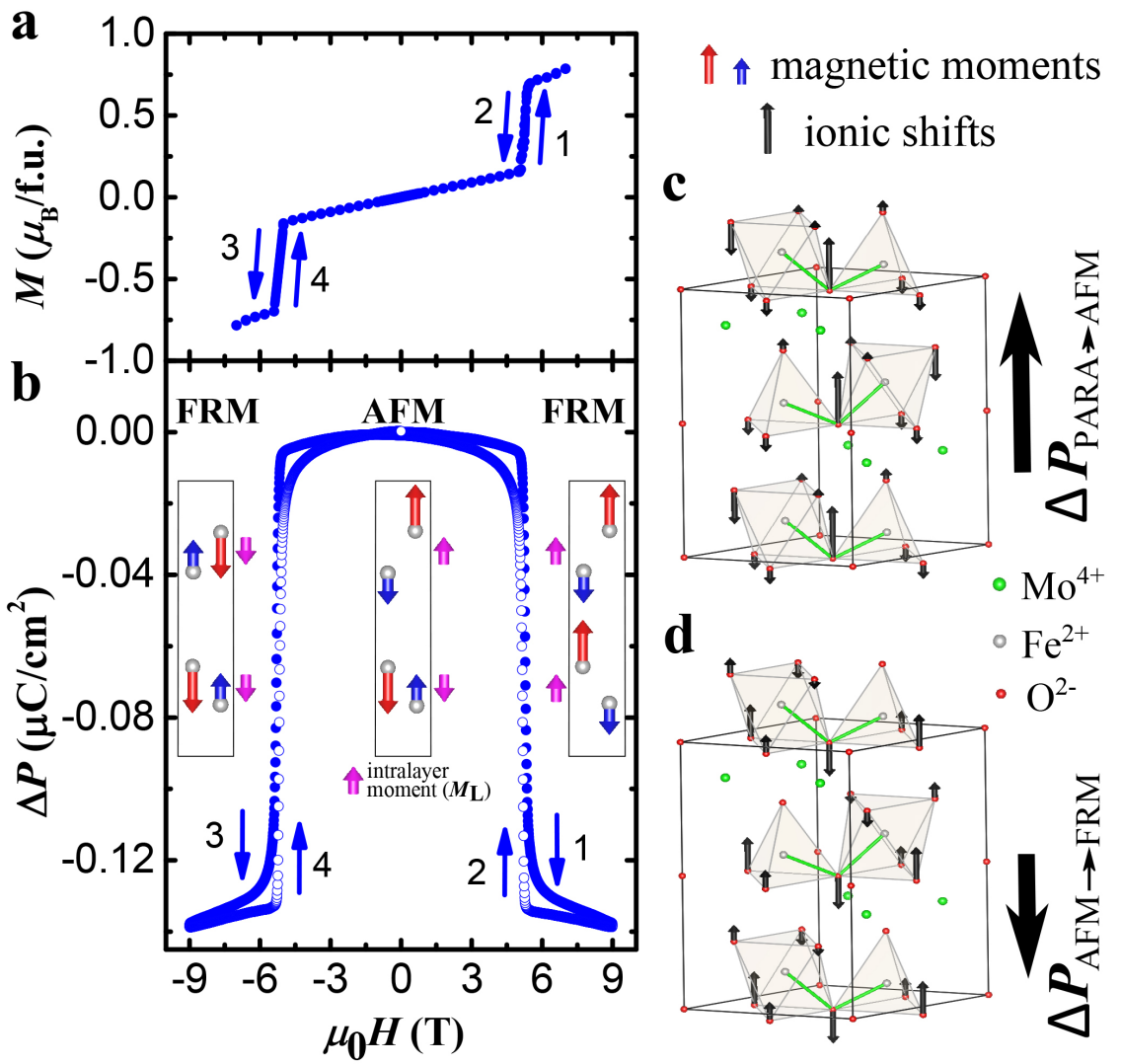

Figure 4.6: **Magnetoelectric effect, and the associated ionic shifts, which is from reference [3].** (a,b) Magnetic field dependence of magnetization $M(H)$ and polarization $\Delta P(H)$ at $T = 55K$. Numbers and arrows indicate the measurement sequence. The insert in (b) shows the magnetic orders and the ferrimagnetic moments of the Fe-O layers for the phases involved. (c) The calculated ionic shifts for the paramagnetic to AFM transition. The thick arrow represents the corresponding change of the electric polarization, ΔP. (d) the same as (c), but for the AFM to FRM transition.

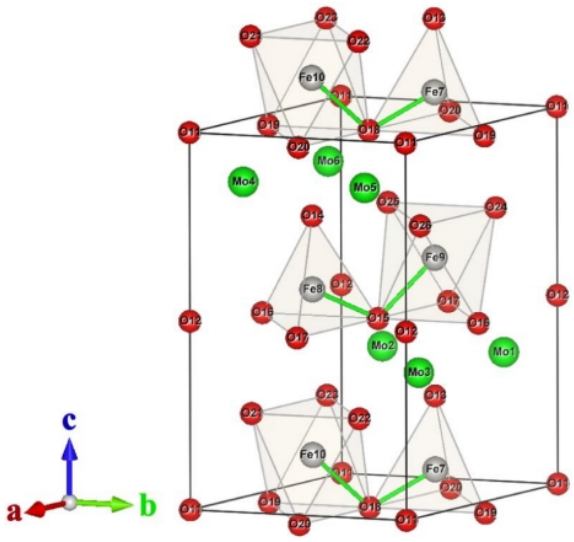

Figure 4.7: **Ionic Labels, which is from reference [3].** These labels are used in Table 4.2

the AFM and FRM. The FRM structure was found marginally higher in total energy (less than 10 meV/f.u.), indicating that this phase is expected to be induced in modest magnetic fields, consistent with our experimental data.

The calculated ionic shifts for the transition from the paramagnetic (PARA) to the AFM state, and from AFM to FRM, are shown in Figures 4.1(d) and 4.6(c,d). The ionic shifts for every ion in the unit cell are given in Table 4.2. The experimental paramagnetic structure, and calculated AFM and FRM structures were used.

The ionic shifts can be utilized for an estimate of the magnetically-induced electric polarization change ΔP. While the total polarization is a multivalued quantity, the difference ΔP between two structures is a well-defined quantity [116]. For a qualitative comparison with experiment, it is sufficient to use the ionic-like formula for ΔP given by $\frac{1}{V}\sum_j (z_j^f - z_j^i)Q_j$, where z_j^i and z_j^f are the c-axis ionic coordinates for the initial and the final structures, respectively, Q_j are the formal ionic charges, V is the unit cell volume, and the sum is taken over the unit cell. For the PARA to AFM, and AFM to FRM transitions, we obtain ΔP values of 0.60(11) $\mu C/cm^2$ and -0.55(11) $\mu C/cm^2$, respectively. The calculated magnitudes and the relative signs of ΔP are in good qualitative agreement with our experiments. The positive sign of ΔP for the PARA to AFM transition indicates that the ΔP vector points along the positive c axis, justifying the convention used in our work.

Ion	$10^3 \times (z_j^{AFM} - z_j^{PARA}) \times c$	$10^3 \times (z_j^{FRM} - z_j^{AFM}) \times c$
Mo1	2(2)	0(3)
Mo2	8(2)	-7(1)
Mo3	8(2)	-4(2)
Mo4	2(2)	0(3)
Mo5	8(2)	-7(1)
Mo6	8(2)	-4(2)
Fe7	10(2)	-5(2)
Fe8	10(2)	-5(3)
Fe9	5(2)	2(2)
Fe10	5(2)	2(2)
O11	10(2)	-3(2)
O12	10(2)	-3(2)
O13	11(2)	-3.5(1.0)
O14	11(2)	-3.5(1.0)
O15	47(10)	-30(12)
O16	-14(2)	30(4)
O17	-14(2)	17(3)
O18	47(10)	-30(12)
O19	-14(2)	30(4)
O20	-14(2)	17(3)
O21	-30(3)	15(10)
O22	6(2)	-9(2)
O23	6(2)	-15(8)
O24	-30(3)	15(10)
O25	6(2)	-9(2)
O26	6(2)	-15(8)

Table 4.2: Calculated ionic shifts (in Å) for the paramagnetic to AFM transition (2^{nd} column), and for the AFM to FRM transition (3^{rd} column). See Figure 4.7 for atomic labeling. Error bars reflect the impact of the multiple low-energy solutions characteristic to the GGA-PBE+U method. This table is from reference [3]

.

The calculated ionic shifts also allow to get an insight into the mechanism of the ME effect. The atoms shift to maximize the magnetic energy gains in the AFM and FRM states. Oxygen ions exhibit the largest shifts, and therefore the ME energy gains should be associated with the modifications of the superexchange paths between the interacting Fe^{2+} spins. Lattice structure, as well as the preservation of the in-plane magnetic order in applied magnetic field, imply that the largest magnetic coupling (J) is between the nearest Fe^{2+} ions, see Figure 4.1(c). The calculations show that upon the transition from the paramagnetic to the AFM state, the Fe-O-Fe angle (θ) between the nearest Fe^{2+} increases

from 109° to ∼111°, mostly due to the oxygen shifts, see Figure 4.1(c). The in-plane antiferromagnetic J increases with increasing θ due to the more favorable Fe-O-Fe orbital overlap, resulting in the magnetic energy gain. Thus, we ascribe the ionic shifts, as well as the accompanying ΔP, to the exchange restriction in the AFM state.

The FRM state can be induced both by a positive and a negative magnetic field along the c axis. The two states differ only by 180° rotation of every spin in the system. While the field-induced magnetizations should be opposite for the opposite fields, ΔP induced by exchange striction should be identical. This prediction is clearly confirmed by the data of Figure 4.6(a,b). The calculated ionic shifts for the AFM to the FRM transitions, shown in Figure 4.6(d), are opposite (but smaller) to those occurring at the PARA to the AFM transition, see Figure 4.6(c). In other words, the lattice partially relaxes towards the paramagnetic structure in the FRM state. This is consistent with the magnetic energy loss due to the interlayer interactions in the FRM phase, and a corresponding relaxation of the lattice distortion realized in the AFM state. As a result, ΔP is negative in the AFM to FRM transition. Thus the data of Figure 4.6(b), in combination with our first-principles calculations, show that exchange striction underlies the ME effect in the transition to the FRM state, as in the AFM transition discussed above.

4.3.5 Reproducible magnetoelectric control of the electric polarization and magnetization

The sharpness of the field-induced transitions shown in Figure 4.4(d) and 4.6(a,b) gives rise to giant values of the differential ME coefficient dP/dH in the vicinity of the transition field, reaching almost $\sim 10^4$ ps/m for T=55 K. (Consult Figure 4.5(d) for the field-dependent dP/dH at different temperatures). Combined with the absence of poling requirements and small hysteresis (0.02 T at 55 K, 0.007 T at 58 K), it leads to giant, reproducible, and almost linear variation of P with H, as shown in Figure 4.8(a) for T=55 K. In the range shown, ΔP oscillates, varying by 0.08 $\mu C/cm^2$ as H goes from 3.25 to 3.5 T and back. The inverse effect, in which an applied electric field (E) changes the magnetization is also giant, reproducible, and linear, as shown in Figure 4.8(b). At T=55 K and $\mu_0 H$=3.345 T, the magnetization varies by 0.35 μ_B/f.u. in the field oscillating between ± 16.6 KV/cm,

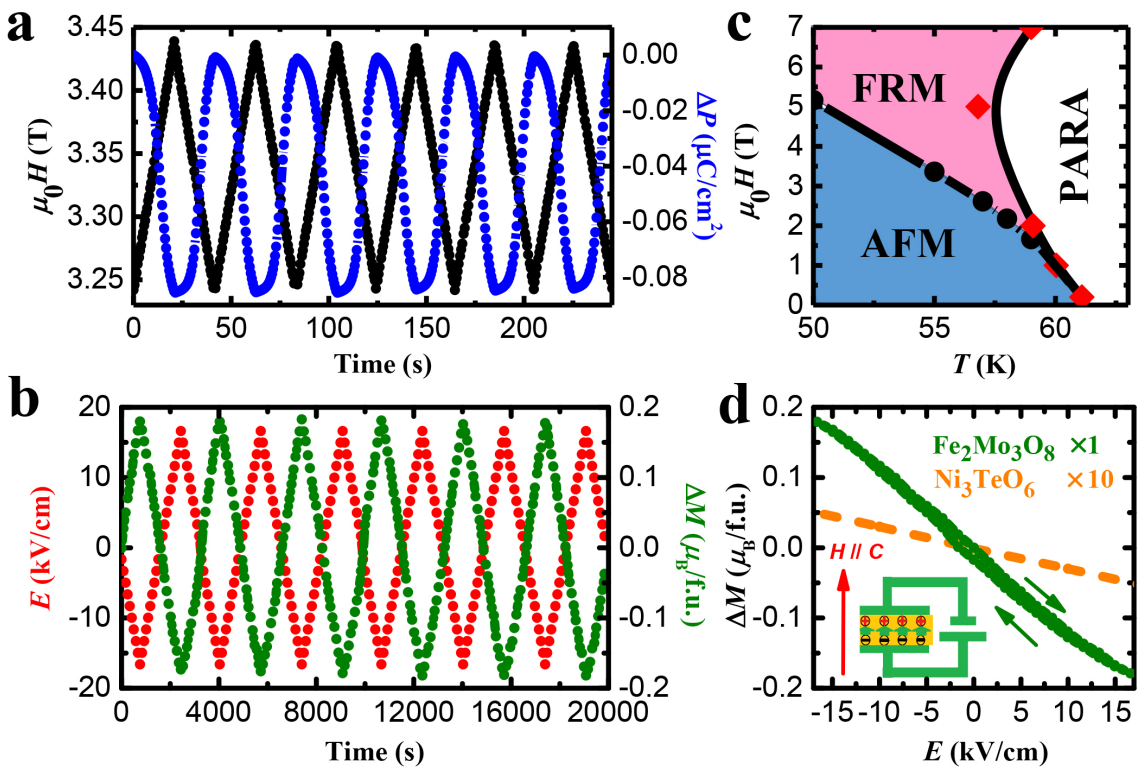

Figure 4.8: **Reproducible magnetoelectric control of the electric polarization and magnetization with giant ME coefficients, which is from reference [3].** (a) Periodic modulation of electric polarization (blue) induced by a magnetic field linearly varying between 3.25 T and 3.5 T (black) at 55 K. (b) Periodic modulation of magnetization (green) induced by an electric field (red) linearly varying between ±16.6 KV/cm, for T=55 K and $\mu_0 H$=3.345 T. (c) Phase diagram of $Fe_2Mo_3O_8$. Black dots determined from $M(H)$, and red diamonds - from $\chi(T)$ curves. (d) Electric field dependence of magnetization for $Fe_2Mo_3O_8$ (from panel (b), averaged), and for Ni_3TeO_6 (×10). The insert illustrates the experimental setup, with directions of the applied fields shown. In all figures, the magnetization, polarization, and the applied fields are along the c axis.

resulting in the dM/dE of -5700 ps/m. Similarly, large differential ME coefficients dP/dH and dM/dE are observed at other points on the AFM-FRM transition boundary shown in Figure 4.8(c). These coefficients are more than an order of magnitude larger than those reported for the polar magnet Ni_3TeO_6 (ref. [117]), see Figure 4.8(d).

When both external fields H and E are collinear and their direction coincides with the positive c axis of the crystal, both ΔP and ΔM are negative in applied positive H and E, respectively. Thus, both dP/dH and dM/dE are negative. The data of Figure 4.6(a,b) show that, consistent with exchange striction mechanism, ΔM changes sign in negative H, while ΔP does not. As a result, both dP/dH and dM/dE change their sign and become positive

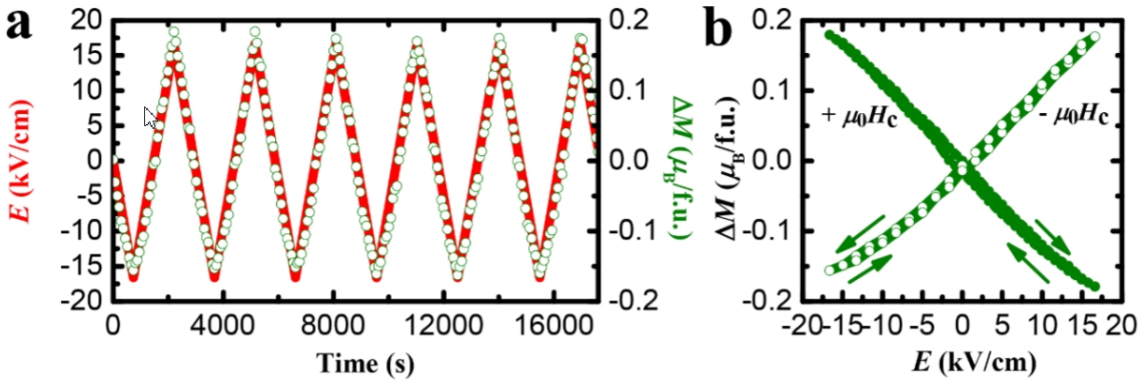

Figure 4.9: **Reversal of the differential magnetoelectric coefficient in $Fe_2Mo_3O_8$ by changing the direction of the bias magnetic field, which is from the supplementary of reference [3].** (a) Periodic modulation of magnetization (green) induced by an electric field (red) linearly varying between ±16.6 KV/cm, for T= 55K and $\mu_0 H$=-3.345 T. These data differ from those shown in Figure 4.8(b) only by the direction of the applied magnetic field. Note the change of the sign of dM/dE. (b) Electric field dependence of magnetization for two opposite bias magnetic fields, +3.345 T, and -3.345 T. All the measurements are along the c axis.

in negative H and E, while retaining the same magnitudes. This sign reversal is illustrated in Figure 4.9.

4.4 Ferromagnetism in $(Fe, Zn)_2Mo_3O_8$

Ferrimagnetism ground state is found to be stabilized in $(Fe, Zn)_2Mo_3O_8$ samples with Zn substituting more than 15% of Fe. The doped Zn atoms prefer to occupy the tetrahedrally coordinated sites in $Fe_2Mo_3O_8$, since the excess octahedral stabilization energy of Fe^{2+} and Zn^{2+} is 17 KJ/mol and 0 KJ/mol, respectively [110]. Figure 4.10 (a) shows the temperature dependence of magnetization for $(Fe_{1-x}Zn_x)_2Mo_3O_8$ (x=0.125, 0.25, 0.5), which show clear ferromagnetic behaviors. The magnetic ordering temperature decreases while more Zn substitution. The magnetic coercive field of $FeZnMo_3O_8$ at 2K is 0.8 T as shown in Figure 4.10 (b). The almost linear behavior of x=0.125 suggests the transition field is higher than 7 T (the maximum field of our MPMS), which was confirmed by published data in reference [118].

T. Kurumaji reports that only AFM ordering exists in $(Fe_{1-x}Zn_x)_2Mo_3O_8$ when $x \leq$ 0.1 and the magnetization peak upon the AFM transition becomes sharper by increasing

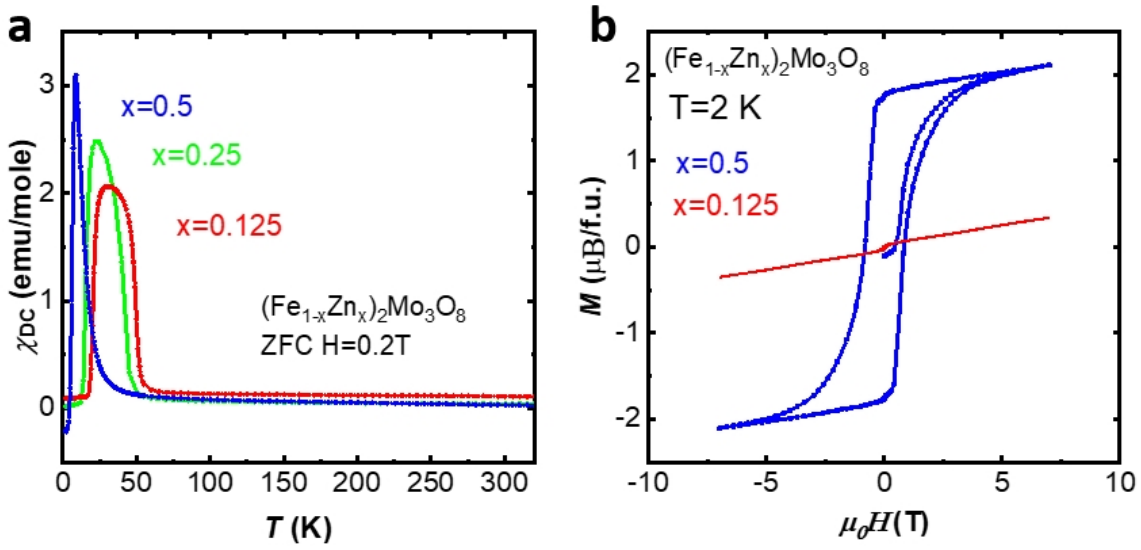

Figure 4.10: **Magnetic properties of** $(Fe_{1-x}Zn_x)_2Mo_3O_8$ **(x=0.125, 0.25, 0.5) poly samples.** (a) Temperature dependence of DC magnetic susceptibility in zero field cooled process. (b) Magnetic field dependence of magnetization at 2K.

x suggesting incipient ferrimagnetism [118]. Here, in our single crystals, we found the co-existence of the 54 K antiferromagnetic ordering and the 42 K ferromagnetic ordering in x=0.07 and 0.09 single crystals, as shown in Figure 4.11. For example, in Figure 4.11 (c) the peaks at 54 K after the ZFC and FC processes overlap with each other indicating an antiferromagnetic transition and the peaks at 42 K after the ZFC and FC processes split indicating a ferromagnetic transition. This sample offers an impressive research opportunity to study the evolution of magnetic domains at these transitions.

For x=0.1, the $M(H)$ curves measured in field parallel and perpendicular to the $c-axis$, shown in Figure 4.12 (b) confirm the ferromagnetic behavior. This is different with the published data, which shows only the antiferromagnetic ordering in x=0.1 sample [118]. This difference can be induced by the mismatch between the real Zn concentration and the nominal one. From the saturated moment along $c-axis$ ($1.65\mu_B/f.u.$) extracted from the $M(H)$ curve, we can estimate the real Fe concentration, assuming the moment for Fe in the octahedral and tetrahedral site is $4\mu_B$ and $3.8\mu_B$, respectively. This calculation gives x=0.19 instead of x=0.1. A more accurate result from Energy-dispersive X-ray spectroscopy (EDX) is x=0.1895, which is consistent with our calculation from saturated moment but different from nominal x=0.1. Then all these behaviors could be explained since only ferromagnetic

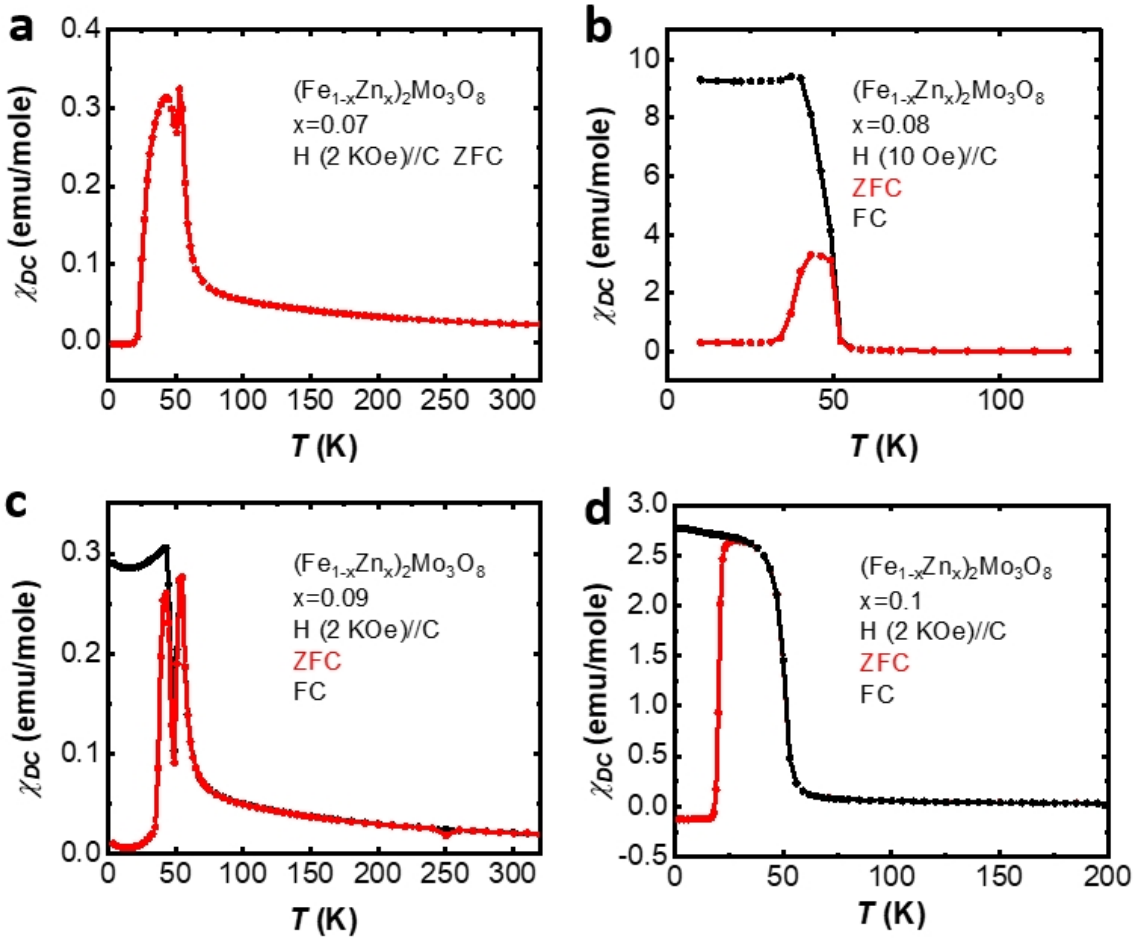

Figure 4.11: **Temperature dependence of DC magnetic susceptibility of $(Fe_{1-x}Zn_x)_2Mo_3O_8$ (x=0.07, 0.08, 0.09, 0.1) single crystals.** $\chi_{DC}(T)$ in zero field-cooled (ZFC) and field-cooled (FC) processes along the crystallographic c-axis of $(Fe_{1-x}Zn_x)_2Mo_3O_8$ (x=0.07 in (a), 0.08 in (b), 0.09 in (c), 0.1 in (d)) single crystals. All these measurements are done on hexagonal shape single crystals, similar to the one shown in Figure 4.2 (b).

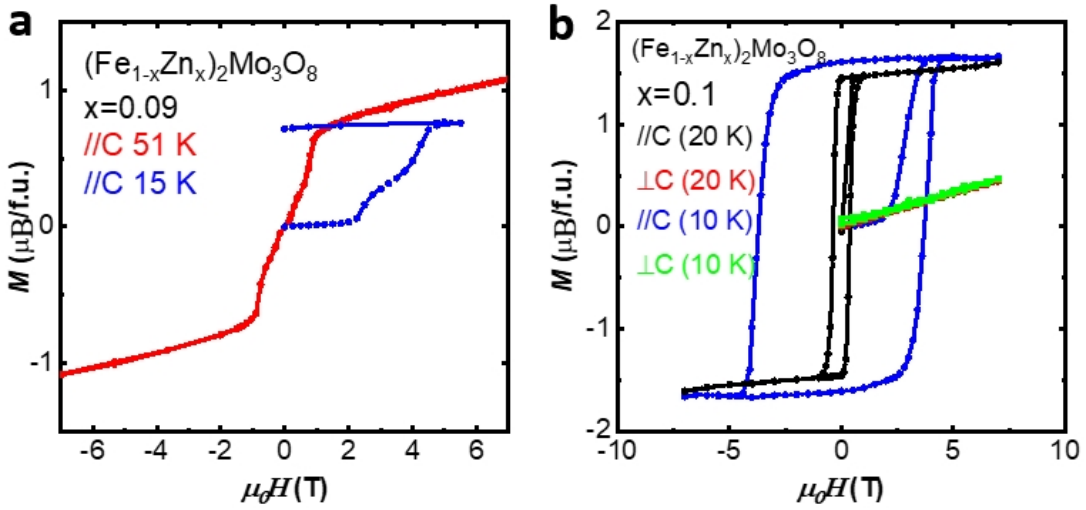

Figure 4.12: **Magnetic field (H) dependence of magnetization (M) for $(Fe_{1-x}Zn_x)_2MO_3O_8$ (x=0.09 and 0.1) single crystals.** (a) $M(H)$ curves measured at 15 K and 51 K in a field along the $c-axis$ for x=0.09 single crystal. (b) Anisotropic $M(H)$ curves measured at 10 K and 20 K for x=0.1 single crystal.

ordering exists in $x \leq 0.125$ samples [118, 119].

4.5 Ferrimagnetism in $Mn_2Mo_3O_8$

Same with $Fe_2Mo_3O_8$, the structure of $Mn_2Mo_3O_8$ is composed of the alternating stacking of the $Mn-O$ layer and the nonmagnetic $Mo-O$ layer, belonging to the polar space group $P6_3mc$ as shown in Figure 4.1. Figure 4.13 (a) shows the anisotropic variation of magnetization with temperature in a single crystal $Mn_2Mo_3O_8$. The larger amplitude along the c axis suggests the moments must be preferentially oriented along the c-axis, which is consistent with the previous reports [11]. Below $T_c = 42K$, the configuration of the magnetic moment of Mn^{2+} is the same as the high field FRM sate in $Fe_2Mo_3O_8$ [120], as shown in Figure 4.2(d). Below the T_c, there is an increment of the electric polarization as shown in Figure 4.13 (c,d). As we discussed in $Fe_2Mo_3O_8$, electric polarization increases 0.34 $\mu C/cm^2$ from the high temperature PARA state to the low temperature AFM sate and decreases 0-0.15 $\mu C/cm^2$ at temperatures lower than T_N from the AFM to the high field ferrimagnetic (FRM) state, which are all correlated to the ionic shifts. From here, we can infer that in $Mn_2Mo_3O_3$, whose ground state is FRM below $Tc = 42K$, the electric polarization will increase when the spins start to become ordered. In $Mn_2Mo_3O_8$, the

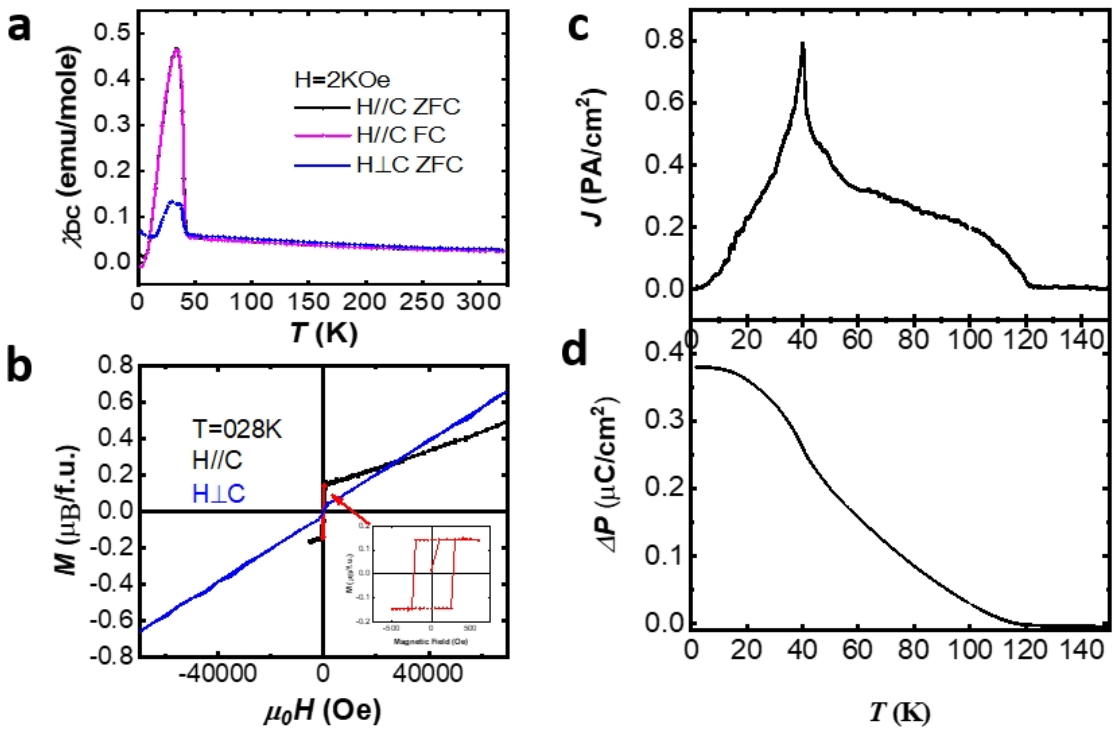

Figure 4.13: **Magnetic and electric property of $Mn_2Mo_3O_8$ single crystal** (a) Temperature dependence of magnetization for $Mn_2Mo_3O_8$ in field H parallel and perpendicular to the c axis, respectively. (b) Magnetic field dependence of magnetization at 28 K in field parallel and perpendicular to the c axis, respectively. The insert of (b) is the zoom in view of the red curve. (c)The pyroelectric current density (J) and the integrated electric polarization (ΔP) as a function of temperature. The current was measured during warming along the $c-axis$ at a sweeping rate of 5K/min.

ME effect is studied and governed by a nonrelativistic exchange striction mechanism [120]. Molecular field theory is used to explain the observed effect, especially for a critical divergence around the transition temperature [120]. T. Kurumaji also observed the enhancement of the ME coefficient's divergence behavior in $MnFe_2Mo_3O_8$, which possibly due to the steeper divergence of sublattice magnetic susceptibility of the doped Fe ion with strong anisotropy [120].

4.6 Antiferromagnetism in $Co_2Mo_3O_8$

For $Co_2Mo_3O_8$, there is a debate on the magnetic ground state: Bertrand and Kerner-Czeskleba conclude from powder neutron data that the magnetic structure is the same as $Fe_2Mo_3O_8$ [111], while S.P. Mcalister and P. Strobel do not see the type of antiferromagnetic

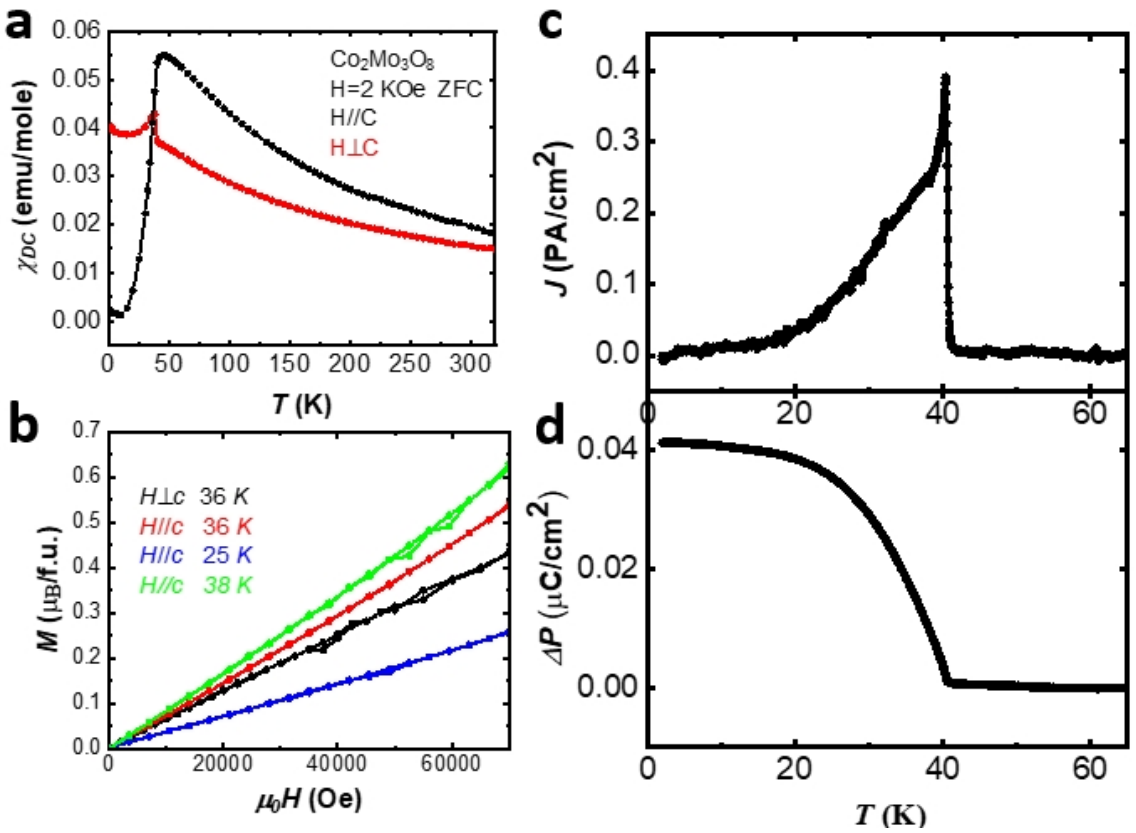

Figure 4.14: **Magnetic properties and the change of electric polarization of $Co_2Mo_3O_8$ single crystal.** (a) Temperature dependence of magnetization in field parallel and perpendicular to the $c-axis$ after zero field cooling process. (b) Magnetic field dependence of magnetization in field parallel to the $c-axis$ at 25 K, 36 K, 38 K and field perpendicular to the $c-axis$ at 36 K.

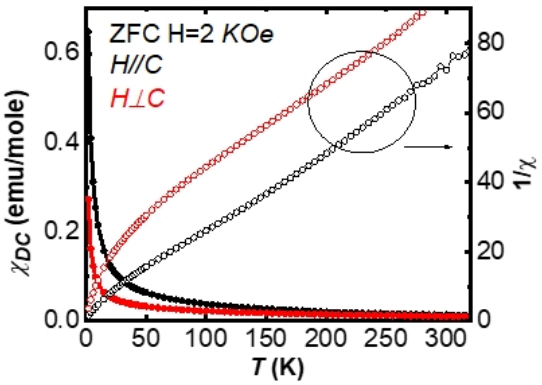

Figure 4.15: **The variance of DC magnetization as a function of temperature of $CoZnMo_3O_8$ single crystal in fields along two different directions, parallel and perpendicular to the $c-axis$.**

arrangement from magnetic measurements [11]. Here, we grow $Co_2Mo_3O_8$ single crystals using a chemical vapor transport method. The as-grown single crystals are black hexagonal plates with typical size $\sim 1 \times 1 \times 1 \times 0.5mm^3$. Figure 4.14 (a) shows the $\chi_{DC}(T)$ curves along two crystallographic directions, parallel and perpendicular to the $c-axis$, which are similar to S.P. Mcalister and P. Strobel's results [11]. The magnetization for $H//C$ does not show the enhancement around T_N as it does in $Fe_2Mo_3O_8$. Furthermore, the $M(H)$ curves in Figure 4.14 (b) measured at temperatures below the transition (39 K) does not show the sharp metamagnetic transition as it does in $Fe_2Mo_3O_8$. Pyroelectric current along the crystal $c-axis$ is measured during warming after zero-field cooling down to 2 K. There is a sharp peak at the magnetic ordering temperature (39 K), as shown in Figure 4.14 (c). The integrated change of polarization is 0.04 $\mu C/cm^2$ shown in Figure 4.14 (d). No change of electric polarization is observed in magnetic fields at various temperatures below 39 K up to 9T, which is consistent with the featureless behavior of the $M(H)$ curves.

In order to have a deeper understanding of the magnetic ground state, we grow and measure the $\chi_{DC}(T)$ of $CoZnMo_3O_8$ single crystal (Figure 4.15) since all the tetrahedral sites will be occupied by non-magnetic Zn. Larger magnetic moment along the $c-axis$ comparing to that perpendicular to the $c-axis$ suggests the spins are aligned along the $c-axis$. Our EDX results also confirm the real ratio between Co and Zn is 1:1 in our hexagonal shape single crystal. From the intersection between the T and the extension

of $\frac{1}{\chi_{DC}}$, we can infer that the antiferromagnetic coupling between two nearest Co_o (Co in octahedral sites) in nearby $a-b$ layers is strong in $CoZnMo_3O_8$.

4.7 Antiferromagnetism in $Ni_2Mo_3O_8$

$Ni_2Mo_3O_8$ single crystals were successfully synthesized and studied by S.P. Mcalister in 1983 [11]. No magnetic ordering was found from $\chi_{DC}(T)$ data down to 2K [11]. Nevertheless the sample did show anisotropy in the temperature dependence of M for an applied field of 10 KOe. Here, we report the growth of high-quality hexagonal shape $(Ni,Zn)_2Mo_3O_8$ single crystals and the existence of a magnetic ordering at 5.75 K and 3.8 K for $Ni_2Mo_3O_8$ and $NiZnMo_3O_8$, respectively. As shown in Figure 4.16 (a), the magnetic susceptibility is larger along the direction perpendicular to the $c-axis$ comparing to that along the $c-axis$ in both $Ni_2Mo_3O_8$ and $NiZnMo_3O_8$, which suggests an in-plane spin configuration different with other $M_2Mo_3O_8$ (M=Fe, Co, Mn) system. An obvious specific heat (C_p) anomaly is present at the magnetic transition, see Figure 4.16 (b). No thermal hysteresis is observed in this specific heat measurement, see the insert of Figure 4.16 (b). To account for the phonon part, the specific heat was fit to a double Debye model as shown by the red line in Figure 4.16 (b). The mismatch at low temperature indicates an additional lattice contribution for these temperatures, suggesting a structural transition associated with the magnetic order. This suggestion is corroborated by the temperature dependence of the dielectric constant $\epsilon(T)$ and the variation of the electric polarization shown in Figure 4.17. Especially, the sharp peak of the pyroelectric current density at the magnetic ordering temperature indicates simultaneous magnetic and structural transitions. Similar to that in $Fe_2Mo_3O_8$ system, no polling is needed in the already polar $Ni_2Mo_3O_8$ to observe the ΔP ($300\mu C/m^2$).

Figure 4.18 (c) shows the $M(H)$ of $Ni_2Mo_3O_8$ single crystal along two different directions at 2K. From the derivative shown in Figure 4.18 (d), we can see there is a transition at 3.8 T in field along the $c-axis$ and a transition at 1.8 T in field perpendicular to the $c-axis$. There might be another phase transition just above 7 T (over the field capability of our MPMS) in field perpendicular to the $c-axis$, which is suggested by the peak in the pyroelectric current density measurement shown in Figure 4.18 (a). In order to find the real correlation, we increase the temperature to 4.5 K, which will decrease the magnetic

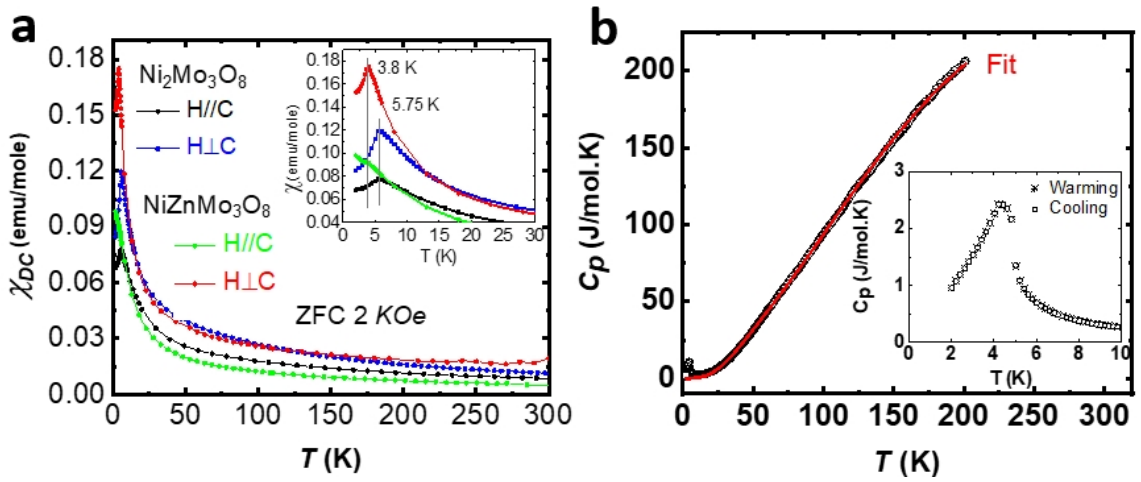

Figure 4.16: **Magnetic transitions in $(Ni, Zn)_2Mo_3O_8$ single crystals.** (a) Temperature dependence of DC magnetic susceptibility χ_{DC} in zero field-cooled (ZFC) process along two crystallographic directions, parallel and perpendicular to the $c-axis$. The insert is the zoom-in of the low temperature part. (b) Specific heat anomaly at the Neel temperature of $Ni_2Mo_3O_8$ single crystal. Red line represents the double Debye model fit. Insert: the data during warming and cooling around the transition.

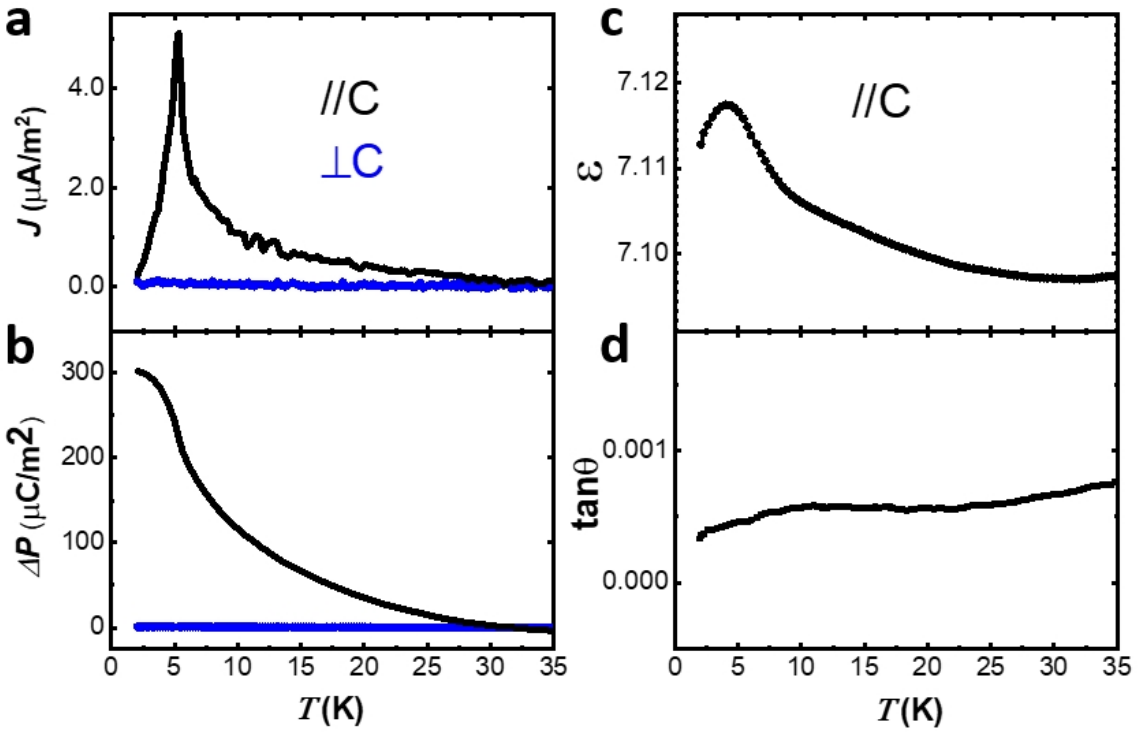

Figure 4.17: **Temperature-induced electric polarization in $Ni_2Mo_3O_8$ single crystal.** (a, b) The measured pyroelectric current density and integrated change of polarization during warming after zero field cooling along two different directions, parallel and perpendicular to the $c-axis$. (c, d) Temperature dependence of the $c-axis$ dielectric constant $\epsilon(T)$ and loss tangent, $f = 44kHZ$.

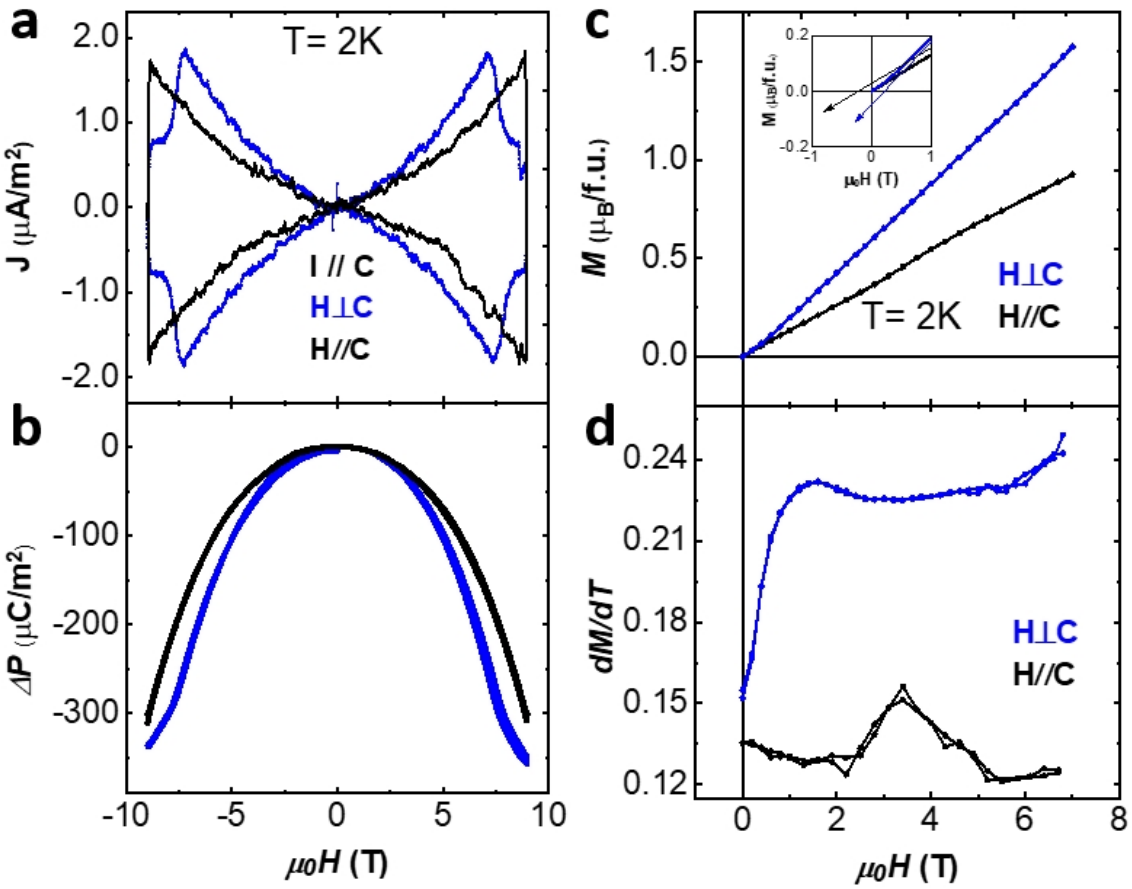

Figure 4.18: **Metamagnetic transition and magnetically-induced electric polarization in $Ni_2Mo_3O_8$ at 2K.**Magnetic field dependence of magnetization ,$M(H)$ in (c) and $dM/dH(H)$ in (d), and electric polarization, $\Delta P(H)$ in (b) and $J(H)$ in (a).

transition field. Magnetic field induces a metamagnetic transition signaled by a sharp peak in the derivative of $M(H//C)$ and $M(H\perp c)$ shown in Figure 4.19 (c). It's accompanied by a structural transition indicated by the corresponding anomaly in the pyroelectric current density, as shown in Figure 4.19 (a).

4.8 Summary and outlook

In conclusion, polar magnets clearly possess a great potential as ME materials. The absence of poling requirements makes possible utilization of giant ME coefficients associated with sharp metamagnetic transition practical, because reproducible, hysteresis-free linear

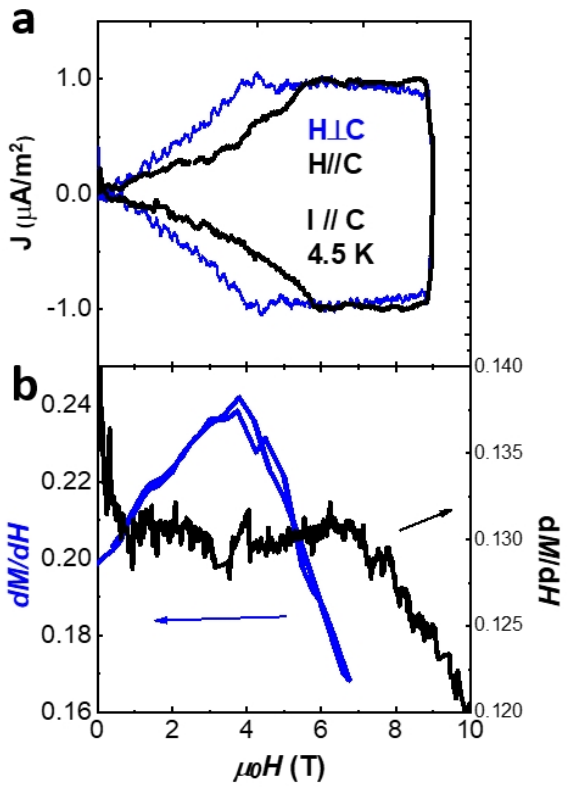

Figure 4.19: **Metemagnetic transition and magnetically-induced electric polarization in $Ni_2Mo_3O_8$ at 4.5K.** Magnetic field dependence of pyroelectric current density in (a) and derivative of magnetization in (b).

responses can be achieved, as necessary for applications. In $Fe_2Mo_3O_8$, hidden ferrimagnetic of the Fe-O layers strongly enhances the magnetic response at the transition field, providing an explanation for the observed giant differential ME coefficient. Exchange striction mechanism of the ME effect in $Fe_2Mo_3O_8$ provides an additional functional capability of controlling the sign of these coefficients by the direction of the applied "bias" magnetic field. In $(Fe, Zn)_2Mo_3O_8$ system, two different phases, antiferromagnetic and ferrimagnetic phases, are competing with each other and the balance between them is controlled by both the magnetic field and Zn doping. Increasing the doped amount of Zn, which will occupy the tetrahedral site, stabilizes the ferrimagnetic order. In $Mn_2Mo_3O_8$, ferrimagnetism is found to be the magnetic ground state below 42K. A structural transition corresponding to a change of electric polarization is observed at the magnetic ordering temperature. In $Co_2Mo_3O_8$, antiferromagnetic ordering occurs at 39 K, accompanied by a structural transition indicated by a corresponding jump in the electric polarization. From the magnetic data of $CoZnMo_3O_8$, we can infer the antiferromagnetic coupling between two nearest Co_o (Co in octahedral sites) in two nearby $a-b$ layers is strong comparing to that in $FeZnMo_3O_8$. In $Ni_2Mo_3O_8$, no magnetic ordering is found from $\chi_{DC}(T)$ data down to 2K in S.P. Mcalister's paper published in 1983 [11]. No other report on this material is published after then. Here, we successfully grow $(Ni, Zn)_2Mo_3O_8$ single crystals and discover the antiferromagnetic ordering at $5.75K$ and $3.8K$ for $Ni_2Mo_3O_8$ and $NiZnMo_3O_8$, respectively. The anomaly at the magnetic ordering temperature in the heat capacitance and dielectric constant measurements indicates a corresponding structural transition. The ME effect is observed through $P(H)$ and $M(H)$ curves below T_N. All these discoveries shed a light on the way to study polar magnets, especially with exchange striction ME mechanism and local ferrimagnetism.

Chapter 5

Epilogue

This thesis presents a systematic study of the hybrid improper ferroelectricity in $Sr_3Sn_2O_7$, the first room-temperature ferroelectric Sn insulator, as well as the giant ME coefficient in $M_2Mo_3O_8$ (M=Fe, Mn, Ni, Zn, Co) polar magnets. In this chapter, I will summarize the results of all discussed projects and give a future research direction.

5.1 Review of results

Chapter 1 focuses on the historical review of ferroelectricity and multiferroicity, which has attracted and keep attracting attention not only due to the research interest also the potential for application in new-generation electronic devices. Comparing with proper and improper ferroelectricity, hybrid improper ferroelectricity is introduced in detail. The origin of electric polarization is explained in several most-attractive hybrid improper ferroelectrics including $(AA')B_2O_6$ double perovskites, $(ABO_3)_2/AO$ Ruddlesden-Popper phase and $A'(AB_2O_7)$ Dion-Jacobson Phase. In the end, a review of polar magnets is done to unveil the great potential for large ME coefficient.

Our works of $(Ca, Sr)_3Ti_2O_7$ (n=2 RP phase) and $Ca_3(Ti, Mn)_2O_7$ (n=2 RP phase) are published [76, 121, 121]: *Yoon Seok Oh, Xuan Luo, Fei-Ting Huang, Yazhong Wang and Sang-Wook Cheong*, **Experimental demonstration of hybrid improper ferroelectricity and the presence of abundant charged walls in $(Ca, Sr)_3Ti_2O_7$ crystals**, Nature Materials, 14, 407-413, 2015; *Fei-Ting Huang, Bin Gao, Jae-Wook Kim, Xuan Luo, Yazhong Wang, Ming-Wen Chu, Chung-Kai Chang, Hwo-Shuenn Sheu and Sang-Wook Cheong*, **Topological defects at octahedral tilting plethora in bi-layered perovskites**, npj Quantum Materials, 1, 16017, 2016 and *Bin Gao, Fei-Ting Huang, Yazhong Wang, Jae-Wook Kim, Lihai Wang, Seong-Joon Lim and Sang-Wook Cheong*,

Interrelation between domain structures and polarization switching in hybrid improper ferroelectric $Ca_3(Mn,Ti)_2O_7$, Applied Physics Letter, 110, 22, 2017.

Chapter 2 focuses on the discovery of hybrid improper ferroelectricity in $Sr_3Sn_2O_7$ (n=2 RP phase). $Pb(Zr_xTi_{1-x})O_3$ (PZT) has been the most successful commercialized ferroelectric material for decades, but the presence of Pb in PZT has been a key issue for the stringent global environmental requirements. Ferroelectrics containing Sn, which belongs to the same group with Pb in the periodic table, could be good candidates. However, there is no room-temperature Sn insulator before our study presumably due to broad bandwidth or poor hybridization with anions, which are related to the inappropriate ionic size. Moreover, there was a debate on the ground state before our work: a result of powder neutron diffraction experiments indicated $Sr_3Sn_2O_7$ adopts a C-centered orthorhombic structure (space group Cmcm) [73], while recent theoretical results have proposed a non-centrosymmetric structure originating from hybrid improper ferroelectricity [46]. Our results including $P(E)$ loops and in situ poling experiments using a dark-field transmission electron microscopy not only demonstrate $Sr_3Sn_2O_7$ being the first room-temperature insulating ferroelectric containing Sn^{4+} also unveil the intriguing polarization switching kinetics.

The relative work in Chapter 2 is published [103]: *Yazhong Wang, Fei-Ting Huang, Xuan Luo, Bin Gao and Sang-Wook Cheong*, **The First Room-Temperature Ferroelectric Sn Insulator and Its Polarization Switching Kinetics**, Advanced Materials, 29, 2, 2017.

Following the discoveries of ferroelectricity in $Sr_3Sn_2O_7$, in chapter 4, we focus on the smallest electric coercive field of $Sr_3Sn_2O_7$ single crystal among all discovered bulk hybrid improper ferroelectrics. The orthorhombic twin domains can be erased and re-generated using small strains, which offers a great opportunity to control functional ferroelastic and ferroelectric domains walls.

In chapter 4, we introduce our systematic study of polar magnets $M_2Mo_3O_8$ (M=Fe, Mn, Zn, Ni, Co). The largest ME coefficient among all discovered polar magnets is found in $Fe_2Mo_3O_8$ single crystal. The absence of poling requirements due to the polar nature makes possible utilization of this giant ME coefficient as necessary for applications. Exchange striction mechanism of the ME effect in $Fe_2Mo_3O_8$ provides an additional functional

capability of controlling the sign of these coefficients by the direction of applied "bias" magnetic field. Other impressive results come from $Ni_2Mo_3O_8$, in which no magnetic ordering was observed in previous studies. Here, our magnetic and dielectric data demonstrate an in-plane magnetic ordering associated with a structural transition occurred at 5.75 K offering more interesting features to this $M_2Mo_3O_8$ system.

The $Fe_2Mo_3O_8$ relative part in Chapter 4 is published [3]: *Yazhong Wang, Gheorghe L Pascut, Bin Gao, Trevor A Tyson, Kristjan Haule, Valery Kiryukhin and Sang-Wook Cheong*, **Unveiling hidden ferrimagnetism and giant magnetoelectricity in polar magnet** $Fe_2Mo_3O_8$, Scientific Reports, 5, 12268, 2015.

5.2 Future research

Starting from the scope of this work, there still exists problems requiring more research as discussed below:

(1)In $Sr_3Sn_2O_7$ system, although we define the charged ferroelastic (ferroelectric) walls based on the polarization directions in two domains crossing the walls, we do not have direct experimental data demonstrating the conduction improvement. cAFM does not show anything since the sample is too insulating. More works, such as gas annealing or p (n) type doping, should be done to improve the conductivity of the bulk sample in order to get meaningful cAFM images. On the other hand, more works should be done to study the tunability of the electric coercive field as a function of different atom doping.

(2)In $Ni_2Mo_3O_8$, we discover the in-plane magnetic ordering associated with a structural transition at 5.75 K. However, there is no direct evidence of the spin configuration at low temperature or the high field state after the metamagnetic transition. More works, like neutron diffraction, should be done to demonstrate the alignment of spins. In $Co_2Mo_3O_8$, magnetic susceptibility suggests an antiferromagnetic ordering, which looks quite different with that in $Fe_2Mo_3O_8$. This probably means the interaction path among magnetic ions is quite different in these two systems, which needs more studies from both experiments and theoretical calculations.

Appendix A

Measurement Method

A.1 Dielectric properties

Dielectric properties are very important in the study of polar magnet and/or multiferroics. In this thesis, the mentioned dielectric measurements including: Dielectric Constant vs. Temperature ($\varepsilon(T)$), Dielectric Constant vs. Magnetic field ($\varepsilon(H)$), Pyroelectric Current Density vs. Temperature ($J(T)$), Pyroelectric Current Density vs. Magnetic Field ($J(H)$), Electric Polarization vs. Temperature ($P(T)$ and $\Delta P(T)$), Electric Polarization vs. Magnetic field ($P(H)$ and $\Delta P(H)$) were performed using similar preparation process, as discussed below.

For all these measurements, we first polish our sample down to 50 μm using the M-PREP 5^{TM} polishing machine from Allied High Tech Products. Inc. Depending on the sample properties, such as oxidation and survivability, we do appropriate high-temperature annealing in different gas flow to release the strain generated during the polishing process. Then, we use either gold paste or silver epoxy to make electrical contacts with gold wire. The control of temperature above room temperature was done inside a high-temperature tube furnace with our homemade measurement probes. And the control of temperature below room temperature was done inside Physical Property Measurement System ($PPMS^{®}$) from Quantum Design.

A.2 Polarization hysteresis loop

Polarization (P) vs. Electric field (E) loop is an important characteristic of the ferroelectricity of a material. The loop shows the nonlinear polarization response of the ferroelectric memory sample to a bipolar triangular voltage stimulus waveform, where polarization is the

nonvolatile memory property of a ferroelectric sample. The hysteresis measurement normally captures the superpositive response of all of the linear and non-linear components, which can be represented by: Hysteresis Response= Resistance + Linear Capacitance + Diode Effects + Remanent Polarization + Non-Remanent Polarization ≈ Remanent Polarization + Non-Remanent Polarization. The remanent-only polarization hysteresis loop is derived by the combination of two hysteresis loops know as Logic 1 and Logic 0, as shown in Figure A.1 and Figure A.2. The Logic 1 loop represents a Hysteresis measurement in which both legs are switching the sample. For each leg, it contains both remanent and non-remanent component. On the contrary, Logic 0 loop represents a Hysteresis measurement in which neither leg switches polarization. It contains only non-remanent polarization. The remanent-only loop is achieved by subtracting Logic 0 from Logic 1. This method, known as positive-up-negative-down (PUND) method, is firstly discussed by Scott, JF in 1988 [48].

All these $P(E)$ measurements are done using the "Piezoelectric Tester" from Radiant Technologies. Inc. All samples are polished down to $20 - 30\mu m$ using the M-PREP 5^{TM} polishing machine from Allied High Tech Products. Inc in order to apply large enough electric field. On the other hand, thinner samples have less change including defects between two electrodes, which may reduce the possibility to break down sample during the measurement.

A.3 Magnetic properties

All measurements of magnetic properties $M(H)$, $\chi_{DC}(T)$ and $M(E)$ are performed in a Quantum Design MPMS-XL7. The electric polarization $P(T)$ and $P(H)$ are performed using Quantum Design PPMS-9.

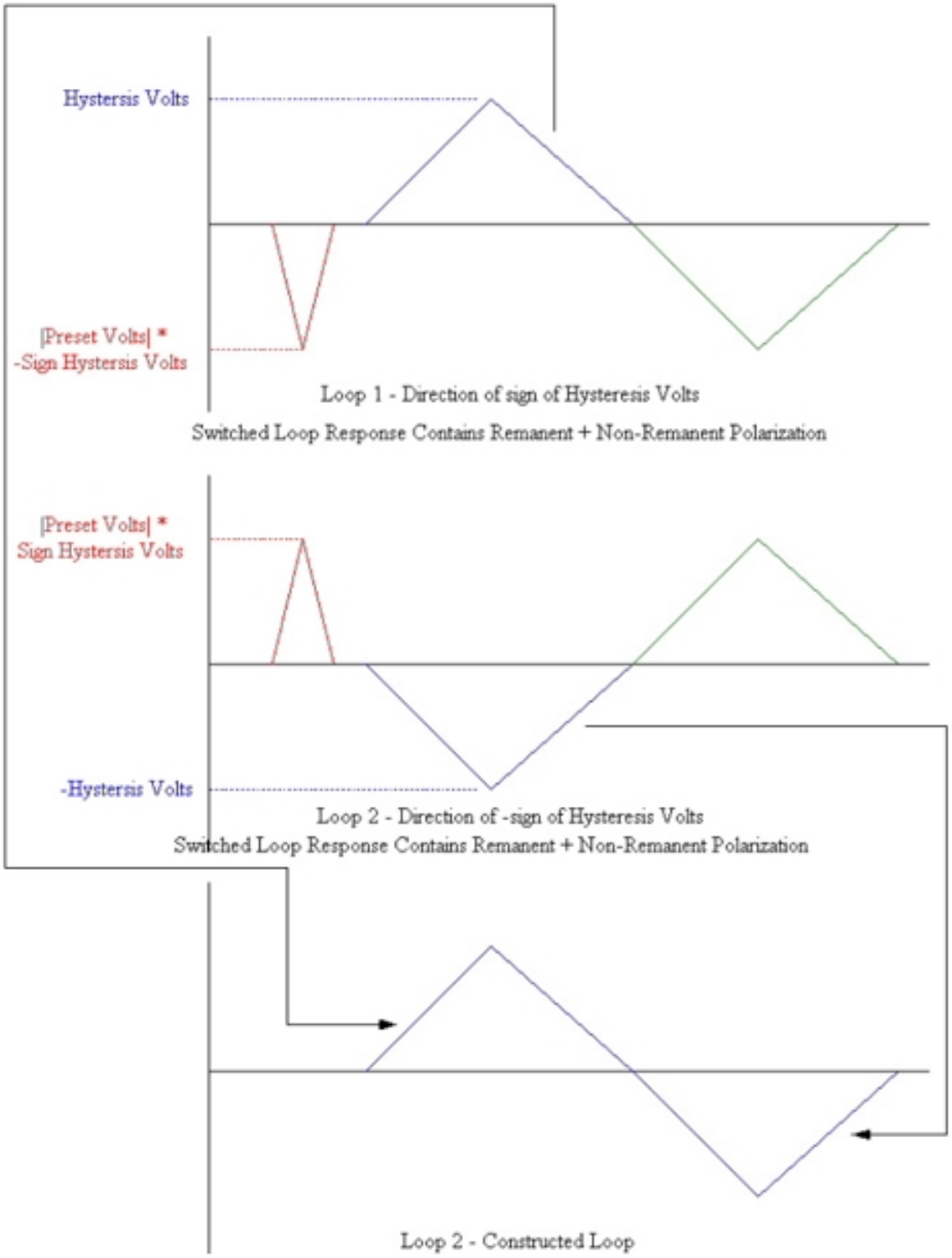

Figure A.1: **Logic 1 Loop Construction** Logic 1 Hysteresis Loop Construction: Response Contains Remanent + Non-Remanent Polarization Components

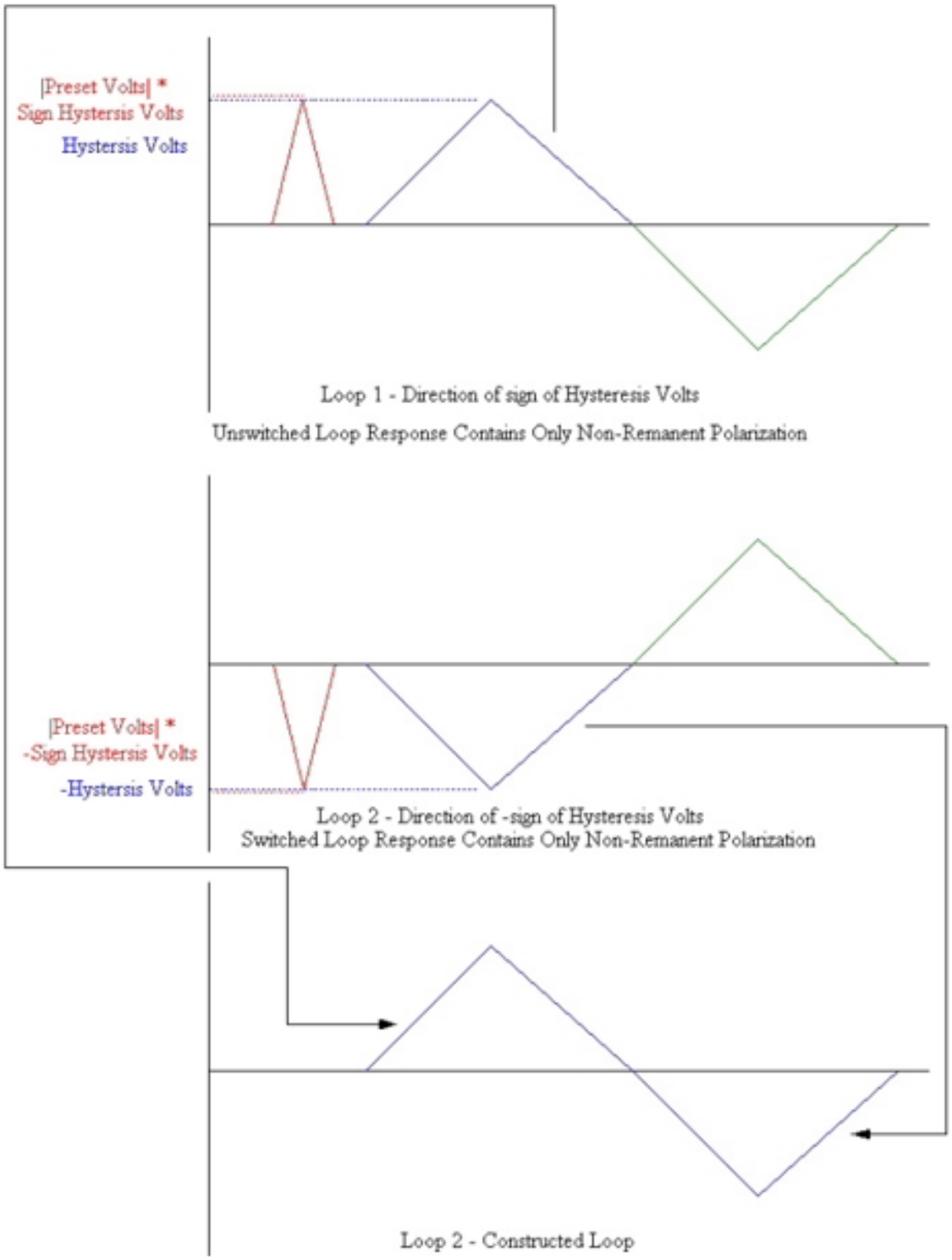

Figure A.2: **Logic 0 Loop Construction** Logic 0 Hysteresis Loop Construction: Response Contains Only Non-Remanent Polarization Components

Appendix B

First principles calculation

In section 2.3, we implemented first principles calculation to study the microscopic properties associated with the structural and magnetic transitions. Ab-initio calculations were performed using the full-potential linearized augmented plan wave (FP-LAPW) method as implemented in the WIEN2K code [122] within the framework of density functional theory [123, 124]. The electronic, magnetic and structural properties of $Fe_2Mo_3O_8$ were calculated using the generalized gradient approximation (GGA) for the exchange-correlation potential, in the form of Perdew, Burke and Ernzerhof [125, 126] (PBE) plus an on-site Coulomb self-interaction correction potential (U) treated by DFT+U, and the double-counting in the fully localized limit [127]. Since the symmetry of low temperature crystal structure is not known, the point group symmetry of the hexagonal paramagnetic space group $P6_3mc$ (reference [112]) was artificially reduced for the purpose of optimizations of internal parameters (OIP). All the calculations were done in the triclinic space group P1, with the lattice parameters kept fixed to a=b=5.773 Å, c=10.054 Å, $\alpha = 90°$, $\beta = 90°$, $\gamma = 120°$. OIP were performed with imposed AFM and FRM magnetic configurations, using as the initial guess the experimentally determined internal parameters of the paramagnetic phase [112]. The search for equilibrium ionic positions was carried out by means of the PORT method with a force tolerance $\leq$ 0.5 mRy/Bohr. The calculations were performed with more than 200 K-points in the irreducible edge of the Brillouin zone ($10 \times 10 \times 4$ mesh). The total energy, charge and force convergence criteria were $\sim 10^{-4}$ Ry, $\sim 10^{-4}$ electrons and 0.25 mRy/Bohr, respectively. The muffin-tin radii R_{MT} were chosen as 1.90, 1.93 and 1.66 Bohr for Mo, Fe and O, respectively. To ensure that no charge leaks outside the core and the valence states to be -10 Ry, thus treating the Mo(4s, 4p, 4d, 5s), Fe(3s, sp, 3d, 4s) and O(2s, 2p) electrons as valence states. All other input parameters were used with their

default values.

Bibliography

[1] S.-W. Cheong and M. Mostovoy, "Multiferroics: a magnetic twist for ferroelectricity," *NATURE MATERIALS*, vol. 6, pp. 13–20, JAN 2007.

[2] S. Kamimura, H. Yamada, and C.-N. Xu, "Strong reddish-orange light emission from stress-activated Sr(n+1)Sn(n)O3(n+1):Sm3+ (n=1, 2, infinity) with perovskite-related structures," *APPLIED PHYSICS LETTERS*, vol. 101, AUG 27 2012.

[3] Y. Wang, G. L. Pascut, B. Gao, T. A. Tyson, K. Haule, V. Kiryukhin, and S.-W. Cheong, "Unveiling hidden ferrimagnetism and giant magnetoelectricity in polar magnet Fe2Mo3O8," *SCIENTIFIC REPORTS*, vol. 5, JUL 21 2015.

[4] N. A. Benedek, A. T. Mulder, and C. J. Fennie, "Polar octahedral rotations: A path to new multifunctional materials," *Journal of Solid State Chemistry*, vol. 195, pp. 11 – 20, 2012.

[5] M. A. Islam, J. M. Rondinelli, and J. E. Spanier, "Normal mode determination of perovskite crystal structures with octahedral rotations: theory and applications," *JOURNAL OF PHYSICS-CONDENSED MATTER*, vol. 25, MAY 1 2013.

[6] S. Amisi, E. Bousquet, K. Katcho, and P. Ghosez, "First-principles study of structural and vibrational properties of srzro$_3$," *Phys. Rev. B*, vol. 85, p. 064112, Feb 2012.

[7] N. A. Benedek, A. T. Mulder, and C. J. Fennie, "Polar octahedral rotations: A path to new multifunctional materials," *Journal of Solid State Chemistry*, vol. 195, pp. 11 – 20, 2012. Polar Inorganic Materials: Design Strategies and Functional Properties.

[8] M. Dawber, N. Stucki, C. Lichtensteiger, S. Gariglio, P. Ghosez, and J.-M. Triscone, "Tailoring the properties of artificially layered ferroelectric superlattices," *Advanced Materials*, vol. 19, no. 23, pp. 4153–4159, 2007.

[9] D. Lee and H. N. Lee, "Controlling oxygen mobility in ruddlesdenpopper oxides," *Materials*, vol. 10, no. 4, 2017.

[10] G. Gou and J. Shi, "Piezoelectricity enhancement in dion-jacobson rbbinb 2 o 7 via negative pressure," *EPL (Europhysics Letters)*, vol. 108, no. 6, p. 67006, 2014.

[11] S. MCALISTER and P. STROBEL, "MAGNETIC ORDER IN M2MO3O8 SINGLE-CRYSTALS (M=MN,FE,CO,NI)," *JOURNAL OF MAGNETISM AND MAGNETIC MATERIALS*, vol. 30, no. 3, pp. 340–348, 1983.

[12] K. A. Rabe, M. Dawber, C. Lichtensteiger, C. H. Ahn, and J.-M. Triscone, "Modern physics of ferroelectrics: Essential background," in *PHYSICS OF FERROELECTRICS: A MODERN PERSPECTIVE* (Rabe, KM and Ahn, CH and Triscone, JM, ed.), vol. 105 of *Topics in Applied Physics*, pp. 1–30, 2007.

[13] D. Fong, G. Stephenson, S. Streiffer, J. Eastman, O. Auciello, P. Fuoss, and C. Thompson, "Ferroelectricity in ultrathin perovskite films," *SCIENCE*, vol. 304, pp. 1650–1653, JUN 11 2004.

[14] J. Haeni, P. Irvin, W. Chang, R. Uecker, P. Reiche, Y. Li, S. Choudhury, W. Tian, M. Hawley, B. Craigo, A. Tagantsev, X. Pan, S. Streiffer, L. Chen, S. Kirchoefer, J. Levy, and D. Schlom, "Room-temperature ferroelectricity in strained SrTiO3," *NATURE*, vol. 430, pp. 758–761, AUG 12 2004.

[15] M. Mostovoy, "Ferroelectricity in spiral magnets," *PHYSICAL REVIEW LETTERS*, vol. 96, FEB 17 2006.

[16] T. Goto, T. Kimura, G. Lawes, A. Ramirez, and Y. Tokura, "Ferroelectricity and giant magnetocapacitance in perovskite rare-earth manganites," *PHYSICAL REVIEW LETTERS*, vol. 92, JUN 25 2004.

[17] F. Pockel *Abh. Gottinger Ges. d Wiss*, vol. 39, 1894.

[18] H. Wieder *Phys. Rev.*, vol. 99, 1955.

[19] W. Cochran, "Crystal stability and the theory of ferroelectricity," *Advances in Physics*, vol. 9, pp. 387–423, Oct. 1960.

[20] G. Shirane and A. Takeda, "Phase transitions in solid solutions of pbzro3 and pbtio3 (i) small concentrations of pbtio3," *Journal of the Physical Society of Japan*, vol. 7, no. 1, pp. 5–11, 1952.

[21] G. Shirane, K. Suzuki, and A. Takeda, "Phase transitions in solid solutions of pbzro3 and pbtio3 (ii) x-ray study," *Journal of the Physical Society of Japan*, vol. 7, no. 1, pp. 12–18, 1952.

[22] E. Sawaguchi, "Ferroelectricity versus antiferroelectricity in the solid solutions of pbzro3 and pbtio3," *Journal of the Physical Society of Japan*, vol. 8, no. 5, pp. 615–629, 1953.

[23] B. Jaffe, R. S. Roth, and S. Marzullo, "Piezoelectric properties of lead zirconatelead titanate solidsolution ceramics," *Journal of Applied Physics*, vol. 25, no. 6, pp. 809–810, 1954.

[24] H. Schmid, "Multi-ferroic magnetoelectrics," *Ferroelectrics*, vol. 162, no. 1, pp. 317–338, 1994.

[25] J. Ma, J. Hu, Z. Li, and C.-W. Nan, "Recent Progress in Multiferroic Magnetoelectric Composites: from Bulk to Thin Films," *ADVANCED MATERIALS*, vol. 23, pp. 1062–1087, MAR 4 2011.

[26] W. Eerenstein, N. D. Mathur, and J. F. Scott, "Multiferroic and magnetoelectric materials," *NATURE*, vol. 442, pp. 759–765, AUG 17 2006.

[27] J. Wang, J. B. Neaton, H. Zheng, V. Nagarajan, S. B. Ogale, B. Liu, D. Viehland, V. Vaithyanathan, D. G. Schlom, U. V. Waghmare, N. A. Spaldin, K. M. Rabe, M. Wuttig, and R. Ramesh, "Epitaxial bifeo3 multiferroic thin film heterostructures," *Science*, vol. 299, no. 5613, pp. 1719–1722, 2003.

[28] N. Hill, "Why are there so few magnetic ferroelectrics?," *JOURNAL OF PHYSICAL CHEMISTRY B*, vol. 104, pp. 6694–6709, JUL 27 2000.

[29] N. A. Spaldin, S.-W. Cheong, and R. Ramesh, "Multiferroics: Past, present, and future," *Physics Today*, vol. 63, no. 10, pp. 38–43, 2010.

[30] R. Ramesh and N. A. Spaldin, "Multiferroics: progress and prospects in thin films," *NATURE MATERIALS*, vol. 6, pp. 21–29, JAN 2007.

[31] S. M. Disseler, X. Luo, B. Gao, Y. S. Oh, R. Hu, Y. Wang, D. Quintana, A. Zhang, Q. Huang, J. Lau, R. Paul, J. W. Lynn, S.-W. Cheong, and W. Ratcliff, "Multiferroicity in doped hexagonal $LuFeo_3$," *Phys. Rev. B*, vol. 92, p. 054435, Aug 2015.

[32] T. N. Stanislavchuk, Y. Wang, Y. Janssen, G. L. Carr, S.-W. Cheong, and A. A. Sirenko, "Magnon and electromagnon excitations in multiferroic $DyFeo_3$," *Phys. Rev. B*, vol. 93, p. 094403, Mar 2016.

[33] T. N. Stanislavchuk, Y. Wang, S.-W. Cheong, and A. A. Sirenko, "Far-ir magnetospectroscopy of magnons and electromagnons in $TbFeo_3$ single crystals at low temperatures," *Phys. Rev. B*, vol. 95, p. 054427, Feb 2017.

[34] P. Ghosez and J.-M. Triscone, "MULTIFERROICS Coupling of three lattice instabilities," *NATURE MATERIALS*, vol. 10, pp. 269–270, APR 2011.

[35] A. Ankudinov, B. Ravel, J. Rehr, and S. Conradson, "Real-space multiple-scattering calculation and interpretation of x-ray-absorption near-edge structure," *PHYSICAL REVIEW B*, vol. 58, pp. 7565–7576, SEP 15 1998.

[36] S. Park and T. Shrout, "Ultrahigh strain and piezoelectric behavior in relaxor based ferroelectric single crystals," *JOURNAL OF APPLIED PHYSICS*, vol. 82, pp. 1804–1811, AUG 15 1997.

[37] R. COHEN, "ORIGIN OF FERROELECTRICITY IN PEROVSKITE OXIDES," *NATURE*, vol. 358, pp. 136–138, JUL 9 1992.

[38] R. E. Cohen, "Origin of ferroelectricity in perovskite oxides," *Nature*, vol. 358, pp. 136–138, July 1992.

[39] H. Fu and R. Cohen, "Polarization rotation mechanism for ultrahigh electromechanical response in single-crystal piezoelectrics," *NATURE*, vol. 403, pp. 281–283, JAN 20 2000.

[40] C.-W. Nan, M. I. Bichurin, S. Dong, D. Viehland, and G. Srinivasan, "Multiferroic magnetoelectric composites: Historical perspective, status, and future directions," *JOURNAL OF APPLIED PHYSICS*, vol. 103, FEB 1 2008.

[41] M. Dawber, K. Rabe, and J. Scott, "Physics of thin-film ferroelectric oxides," *REVIEWS OF MODERN PHYSICS*, vol. 77, pp. 1083–1130, OCT 2005.

[42] A. P. Levanyuk and D. G. Sannikov, "Improper ferroelectrics," *Soviet Physics Uspekhi*, vol. 17, no. 2, p. 199, 1974.

[43] T. Choi, Y. Horibe, H. T. Yi, Y. J. Choi, W. Wu, and S. W. Cheong, "Insulating interlocked ferroelectric and structural antiphase domain walls in multiferroic YMnO3," *NATURE MATERIALS*, vol. 9, pp. 253–258, MAR 2010.

[44] B. Van Aken, T. Palstra, A. Filippetti, and N. Spaldin, "The origin of ferroelectricity in magnetoelectric YMnO3," *NATURE MATERIALS*, vol. 3, pp. 164–170, MAR 2004.

[45] Z. Huang, Y. Cao, Y. Sun, Y. Xue, and C. Chu, "Coupling between the ferroelectric and antiferromagnetic orders in YMnO3," *PHYSICAL REVIEW B*, vol. 56, pp. 2623–2626, AUG 1 1997.

[46] N. A. Benedek and C. J. Fennie, "Hybrid improper ferroelectricity: A mechanism for controllable polarization-magnetization coupling," *Phys. Rev. Lett.*, vol. 106, p. 107204, Mar 2011.

[47] A. Mulder, N. Benedek, J. Rondinelli, and C. Fennie, "Turning abo3 antiferroelectrics into ferroelectrics: Design rules for practical rotation-driven ferroelectricity in double perovskites and a3b2o7 ruddlesden-popper compounds," *Advanced Functional Materials*, vol. 23, pp. 4810–4820, 5 2013.

[48] J. SCOTT, L. KAMMERDINER, M. PARRIS, S. TRAYNOR, V. OTTENBACHER, A. SHAWABKEH, and W. OLIVER, "SWITCHING KINETICS OF LEAD ZIRCONATE TITANATE SUB-MICRON THIN-FILM MEMORIES," *JOURNAL OF APPLIED PHYSICS*, vol. 64, pp. 787–792, JUL 15 1988.

[49] A. B. Harris, "Symmetry analysis for the ruddlesden-popper systems $ca_3mn_2o_7$ and $ca_3ti_2o_7$," *Physical Review B*, vol. 84, p. 064116, Aug. 2011.

[50] T. M. Dion. M, Ganne. M, "New families of phases mm2nb3o10 consisting of "perovskite" sheets," *Material Research Bulletin*, vol. 16, pp. 1429–1435, 1981.

[51] A. JACOBSON, J. JOHNSON, and J. LEWANDOWSKI, "INTERLAYER CHEMISTRY BETWEEN THICK TRANSITION-METAL OXIDE LAYERS - SYNTHESIS AND INTERCALATION REACTIONS OF K[CA2NAN-3NBNO3N+1] (3 LESS-THAN-OR-EQUAL-TO N LESS-THAN-OR-EQUAL-TO 7)," *INORGANIC CHEMISTRY*, vol. 24, no. 23, pp. 3727–3729, 1985.

[52] C. J. Fennie and K. M. Rabe, "Ferroelectricity in the Dion-Jacobson CsBiNb2O7 from first principles," *APPLIED PHYSICS LETTERS*, vol. 88, JUN 26 2006.

[53] B.-W. Li, M. Osada, T. C. Ozawa, and T. Sasaki, "Rbbinb2o7: A new lead-free high-tc ferroelectric," *Chemistry of Materials*, vol. 24, no. 16, pp. 3111–3113, 2012.

[54] H. Sim and B. G. Kim, "Octahedral tilting and ferroelectricity in $rba nb_2o_7$ (a = bi, nd) from first principles," *Phys. Rev. B*, vol. 89, p. 144114, Apr 2014.

[55] L. Bellaiche, A. Garcia, and D. Vanderbilt, "Low-temperature properties of Pb(Zr1-xTix)O-3 solid solutions near the morphotropic phase boundary," *FERROELECTRICS*, vol. 266, pp. 41–56, 2002.

[56] W. Cao, "Ferroelectrics - The strain limits on switching," *NATURE MATERIALS*, vol. 4, pp. 727–728, OCT 2005.

[57] E. A. Neppiras, "Book Review: Piezoelectric ceramics 1971. B. Jaffe, W. R. Cook Jr and H. Jaffe.," *Journal of Sound Vibration*, vol. 20, pp. 562–563, Feb. 1972.

[58] A. Toprak and O. Tigli, "Piezoelectric energy harvesting: State-of-the-art and challenges," *APPLIED PHYSICS REVIEWS*, vol. 1, SEP 2014.

[59] M. S. Jaffe B, Roth R.S, "Properties of piezoelectric ceramics in the solid-solution

series lead titanate-lead zirconate-lead oxide: Thin oxide and lead titanate-lead hafnate," *Journal of Research of the National Bureau of Standards*, vol. 55, no. 5, p. 239, 1955.

[60] H. Du, Z. Li, F. Tang, S. Qu, Z. Pei, and W. Zhou, "Preparation and piezoelectric properties of (k0.5na0.5)nbo3 lead-free piezoelectric ceramics with pressure-less sintering," *Materials Science and Engineering: B*, vol. 131, no. 1, pp. 83 – 87, 2006.

[61] H. T. Y. Saito, T. N. T. Tani, T. H. K. Takatori, and M. N. T. Nagaya, "Lead-free piezoceramics," *Nature*, vol. 432, pp. 84 – 87, 2004.

[62] D. Chen, S. Ouyang, and J. Ye, "Photocatalytic Degradation of Isopropanol Over PbSnO3 Nanostructures Under Visible Light Irradiation," *NANOSCALE RESEARCH LETTERS*, vol. 4, pp. 274–280, MAR 2009.

[63] W. Xiao, D. Tan, W. Zhou, M. Chen, X. Xiong, M. Song, J. Liu, H.-K. Ma, and J. Xu, "A new cubic perovskite in PbGeO3 at high pressures," *AMERICAN MINERALOGIST*, vol. 97, pp. 1193–1198, JUL 2012.

[64] Y. ZHAO and D. WEIDNER, "THERMAL-EXPANSION OF SRZRO3 AND BAZRO3 PEROVSKITES," *PHYSICS AND CHEMISTRY OF MINERALS*, vol. 18, no. 5, pp. 294–301, 1991.

[65] D. M. Toebbens, V. Kahlenberg, C. Gspan, and G. Kothleitner, "Atomic and domain structure of the low-temperature phase of barium metagermanate (BaGeO3)," *ACTA CRYSTALLOGRAPHICA SECTION B-STRUCTURAL SCIENCE*, vol. 62, pp. 1002–1009, DEC 2006.

[66] G. Shirane and R. Pepinsky, "Phase transitions in antiferroelectric $pbhfo_3$," *Phys. Rev.*, vol. 91, pp. 812–815, Aug 1953.

[67] G. A. Samara, "Pressure and temperature dependence of the dielectric properties and phase transitions of the antiferroelectric perovskites: $Pbzro_3$ and $pbhfo_3$," *Phys. Rev. B*, vol. 1, pp. 3777–3786, May 1970.

[68] S. F. Matar, I. Baraille, and M. A. Subramanian, "First principles studies of SnTiO3 perovskite as potential environmentally benign ferroelectric material," *CHEMICAL PHYSICS*, vol. 355, pp. 43–49, JAN 7 2009.

[69] S. Eijt, R. Currat, J. Lorenzo, P. Saint-Gregoire, S. Katano, T. Janssen, B. Hennion, and Y. Vysochanskii, "Soft modes and phonon interactions in Sn2P2Se6 studied by means of neutron scattering," *JOURNAL OF PHYSICS-CONDENSED MATTER*, vol. 10, pp. 4811–4844, JUN 8 1998.

[70] K. Moriya, H. Kuniyoshi, K. Tashita, Y. Ozaki, S. Yano, and T. Matsuo, "Ferroelectric phase transitions in Sn2P2S6 and Sn2P2Se6 crystals," *JOURNAL OF THE PHYSICAL SOCIETY OF JAPAN*, vol. 67, pp. 3505–3511, OCT 1998.

[71] C. Carpentier and R. Nitsche, "Ferroelectricity in sn2p2s6," *Materials Research Bulletin*, vol. 9, no. 8, pp. 1097 – 1100, 1974.

[72] B. Lei, S.-Q. Man, Y. Du, and S. Yue, "Luminescence properties of Sm3+-doped Sr3Sn2O7 phosphor," *MATERIALS CHEMISTRY AND PHYSICS*, vol. 124, pp. 912–915, DEC 1 2010.

[73] M. Green, K. Prassides, P. Day, and D. Neumann, "Structure of the n=2 and n=infinity member of the Ruddlesden-Popper series, Sr(n+1)Sn(n)O3(n+1)," *INTERNATIONAL JOURNAL OF INORGANIC MATERIALS*, vol. 2, pp. 35–41, FEB 2000.

[74] F. T. Huang, X. Wang, Y. S. Oh, K. Kurushima, S. Mori, Y. Horibe, and S. W. Cheong, "Delicate balance between ferroelectricity and antiferroelectricity in hexagonal InMnO3," *PHYSICAL REVIEW B*, vol. 87, MAY 13 2013.

[75] P. S. Bednyakov, T. Sluka, A. K. Tagantsev, D. Damjanovic, and N. Setter, "Formation of charged ferroelectric domain walls with controlled periodicity," *SCIENTIFIC REPORTS*, vol. 5, OCT 30 2015.

[76] Y. S. Oh, X. Luo, F.-T. Huang, Y. Wang, and S.-W. Cheong, "Experimental demonstration of hybrid improper ferroelectricity and the presence of abundant charged

walls in (Ca, Sr)(3)Ti2O7 crystals," *NATURE MATERIALS*, vol. 14, pp. 407–413, APR 2015.

[77] T. Rojac, A. Bencan, G. Drazic, N. Sakamoto, H. Ursic, B. Jancar, G. Tavcar, M. Makarovic, J. Walker, B. Malic, and D. Damjanovic, "Domain-wall conduction in ferroelectric BiFeO3 controlled by accumulation of charged defects," *NATURE MATERIALS*, vol. 16, pp. 322+, MAR 2017.

[78] T. Sluka, A. K. Tagantsev, P. Bednyakov, and N. Setter, "Free-electron gas at charged domain walls in insulating BaTiO3," *NATURE COMMUNICATIONS*, vol. 4, MAY 2013.

[79] D. Meier, "Functional domain walls in multiferroics," *JOURNAL OF PHYSICS-CONDENSED MATTER*, vol. 27, NOV 25 2015.

[80] J. Grollier, D. Lacour, V. Cros, A. Hamzic, A. Vaures, A. Fert, D. Adam, and G. Faini, "Switching the magnetic configuration of a spin valve by current-induced domain wall motion," *JOURNAL OF APPLIED PHYSICS*, vol. 92, pp. 4825–4827, OCT 15 2002.

[81] D.-S. Han, S.-K. Kim, J.-Y. Lee, S. J. Hermsdoerfer, H. Schultheiss, B. Leven, and B. Hillebrands, "Magnetic domain-wall motion by propagating spin waves," *APPLIED PHYSICS LETTERS*, vol. 94, MAR 16 2009.

[82] J. Grollier, A. Chanthbouala, R. Matsumoto, A. Anane, V. Cros, F. N. van Dau, and A. Fert, "Magnetic domain wall motion by spin transfer," *COMPTES RENDUS PHYSIQUE*, vol. 12, pp. 309–317, APR 2011.

[83] Y. Zhou and M. Ezawa, "A reversible conversion between a skyrmion and a domain-wall pair in a junction geometry," *NATURE COMMUNICATIONS*, vol. 5, AUG 2014.

[84] Y. P. Ivanov, A. Chuvilin, S. Lopatin, and J. Kosel, "Modulated Magnetic Nanowires for Controlling Domain Wall Motion: Toward 3D Magnetic Memories," *ACS NANO*, vol. 10, pp. 5326–5332, MAY 2016.

[85] J. A. Mundy, J. Schaab, Y. Kumagai, A. Cano, M. Stengel, I. P. Krug, D. M. Gottlob, H. Doganay, M. E. Holtz, R. Held, Z. Yan, E. Bourret, C. M. Schneider, D. G. Schlom, D. A. Muller, R. Ramesh, N. A. Spaldin, and D. Meier, "Functional electronic inversion layers at ferroelectric domain walls," *NATURE MATERIALS*, vol. 16, pp. 622+, JUN 2017.

[86] P. Sharma, Q. Zhang, D. Sando, C. H. Lei, Y. Liu, J. Li, V. Nagarajan, and J. Seidel, "Nonvolatile ferroelectric domain wall memory," *SCIENCE ADVANCES*, vol. 3, JUN 2017.

[87] M. R. Lukatskaya, B. Dunn, and Y. Gogotsi, "Multidimensional materials and device architectures for future hybrid energy storage," *NATURE COMMUNICATIONS*, vol. 7, SEP 2016.

[88] A. Ohtomo and H. Hwang, "A high-mobility electron gas at the LaAlO3/SrTiO3 heterointerface," *NATURE*, vol. 427, pp. 423–426, JAN 29 2004.

[89] H. Y. Hwang, Y. Iwasa, M. Kawasaki, B. Keimer, N. Nagaosa, and Y. Tokura, "Emergent phenomena at oxide interfaces," *NATURE MATERIALS*, vol. 11, pp. 103–113, FEB 2012.

[90] P. Zubko, S. Gariglio, M. Gabay, P. Ghosez, and J.-M. Triscone, "Interface Physics in Complex Oxide Heterostructures," in *ANNUAL REVIEW OF CONDENSED MATTER PHYSICS, VOL 2* (Langer, JS, ed.), vol. 2 of *Annual Review of Condensed Matter Physics*, pp. 141–165, 2011.

[91] G. Catalan, J. Seidel, R. Ramesh, and J. F. Scott, "Domain wall nanoelectronics," *REVIEWS OF MODERN PHYSICS*, vol. 84, pp. 119–156, FEB 3 2012.

[92] P. Maksymovych, J. Seidel, Y. H. Chu, P. Wu, A. P. Baddorf, L.-Q. Chen, S. V. Kalinin, and R. Ramesh, "Dynamic Conductivity of Ferroelectric Domain Walls in BiFeO3," *NANO LETTERS*, vol. 11, pp. 1906–1912, MAY 2011.

[93] B. M. Vul, G. M. Guro, and I. I. Ivanchik, "Encountering domains in ferroelectrics," *Ferroelectrics*, vol. 6, no. 1, pp. 29–31, 1973.

[94] E. G. Fesenko, V. G. Gavrilyatchenko, M. A. Martinenko, A. F. Semenchov, and I. P. Lapin, "Domain structure peculiarities of lead-titanate crystals," *Ferroelectrics*, vol. 6, no. 1, pp. 61–65, 1973.

[95] Z. Surowiak, J. Dec, R. Skulski, E. G. Fesenko, V. G. Gavrilyatchenko, and A. F. Semenchev, "The domain structure formation at phase transitions," *Ferroelectrics*, vol. 20, no. 1, pp. 277–279, 1978.

[96] A. A. Grekov, A. A. Adonin, and N. P. Protsenko, "Encountering domains in sbsl," *Ferroelectrics*, vol. 13, no. 1, pp. 483–485, 1976.

[97] T. Kämpfe, P. Reichenbach, M. Schröder, A. Haußmann, L. M. Eng, T. Woike, and E. Soergel, "Optical three-dimensional profiling of charged domain walls in ferroelectrics by cherenkov second-harmonic generation," *Phys. Rev. B*, vol. 89, p. 035314, Jan 2014.

[98] J. Seidel, L. W. Martin, Q. He, Q. Zhan, Y. H. Chu, A. Rother, M. E. Hawkridge, P. Maksymovych, P. Yu, M. Gajek, N. Balke, S. V. Kalinin, S. Gemming, F. Wang, G. Catalan, J. F. Scott, N. A. Spaldin, J. Orenstein, and R. Ramesh, "Conduction at domain walls in oxide multiferroics," *NATURE MATERIALS*, vol. 8, pp. 229–234, MAR 2009.

[99] J. Li, H. X. Yang, H. F. Tian, C. Ma, S. Zhang, Y. G. Zhao, and J. Q. Li, "Scanning secondary-electron microscopy on ferroelectric domains and domain walls in ymno3," *Applied Physics Letters*, vol. 100, no. 15, p. 152903, 2012.

[100] M. Schroeder, A. Haussmann, A. Thiessen, E. Soergel, T. Woike, and L. M. Eng, "Conducting Domain Walls in Lithium Niobate Single Crystals," *ADVANCED FUNCTIONAL MATERIALS*, vol. 22, pp. 3936–3944, SEP 25 2012.

[101] J. R. Whyte, R. G. P. McQuaid, P. Sharma, C. Canalias, J. F. Scott, A. Gruverman, and J. M. Gregg, "Ferroelectric Domain Wall Injection," *ADVANCED MATERIALS*, vol. 26, pp. 293–298, JAN 15 2014.

[102] J. R. Whyte, R. G. P. McQuaid, C. M. Ashcroft, J. F. Einsle, C. Canalias, A. Gruverman, and J. M. Gregg, "Sequential injection of domain walls into ferroelectrics at different bias voltages: Paving the way for domain wall memristors," *Journal of Applied Physics*, vol. 116, no. 6, p. 066813, 2014.

[103] W. Yazhong, F.-T. Huang, X. Luo, B. Gao, and S.-W. Cheong, "The first room-temperature ferroelectric sn insulator and its polarization switching kinetics," *Advanced Materials*, vol. 29, no. 2, pp. 1601288–n/a, 2017. 1601288.

[104] X. Q. Liu, J. W. Wu, X. X. Shi, H. J. Zhao, H. Y. Zhou, R. H. Qiu, W. Q. Zhang, and X. M. Chen, "Hybrid improper ferroelectricity in ruddlesden-popper ca3(ti,mn)2o7 ceramics," *Applied Physics Letters*, vol. 106, no. 20, p. 202903, 2015.

[105] J. Y. Jo, Y. S. Kim, T. W. Noh, J.-G. Yoon, and T. K. Song, "Coercive fields in ultrathin batio3 capacitors," *Applied Physics Letters*, vol. 89, no. 23, p. 232909, 2006.

[106] P. S. Halasyamani and K. R. Poeppelmeier, "Noncentrosymmetric oxides," *Chemistry of Materials*, vol. 10, no. 10, pp. 2753–2769, 1998.

[107] J.-Y. Kim, T. Y. Koo, and J.-H. Park, "Orbital and bonding anisotropy in a half-filled $gafeo_3$ magnetoelectric ferrimagnet," *Phys. Rev. Lett.*, vol. 96, p. 047205, Jan 2006.

[108] Y. S. Oh, S. Artyukhin, J. J. Yang, V. Zapf, J. W. Kim, D. Vanderbilt, and S.-W. Cheong, "Non-hysteretic colossal magnetoelectricity in a collinear antiferromagnet," *Nature communications*, vol. 5, p. 3201, 2014.

[109] W. H. McCarroll, L. Katz, and R. Ward, "Some ternary oxides of tetravalent molybdenum1,2," *Journal of the American Chemical Society*, vol. 79, no. 20, pp. 5410–5414, 1957.

[110] Varret, F., Czeskleba, H., Hartmann-Boutron, F., and Imbert, P., "tude par effet mssbauer de l'ion fe2+ en symtrie trigonale dans les composs du type (fe, m)2mo3o8 (m = mg, zn, mn, co, ni) et proprits magntiques de (fe, zn) 2mo3o8," *J. Phys. France*, vol. 33, no. 5-6, pp. "549–564", 1972.

[111] Bertrand, D. and Kerner-Czeskleba, H., "tude structurale et magntique de molybdates d'lments de transition," *J. Phys. France*, vol. 36, no. 5, pp. 379–390, 1975.

[112] Y. Le Page and P. Strobel, "Structure of iron(II) molybdenum(IV) oxide $Fe_2Mo_3O_8$," *Acta Crystallographica Section B*, vol. 38, pp. 1265–1267, Apr 1982.

[113] H. Czeskleba, P. Imbert, and F. Varret, "Mössbauer Study of $Fe_2Mo_3O_8$ and $FeZnMo_3O_8$," in *American Institute of Physics Conference Series*, vol. 5 of *American Institute of Physics Conference Series*, pp. 811–815, Mar. 1972.

[114] S.-W. Cheong, J. D. Thompson, and Z. Fisk, "Metamagnetism in la_2cuo_4," *Phys. Rev. B*, vol. 39, pp. 4395–4398, Mar 1989.

[115] J. de Groot, K. Marty, M. D. Lumsden, A. D. Christianson, S. E. Nagler, S. Adiga, W. J. H. Borghols, K. Schmalzl, Z. Yamani, S. R. Bland, R. de Souza, U. Staub, W. Schweika, Y. Su, and M. Angst, "Competing ferri- and antiferromagnetic phases in geometrically frustrated $lufe_2\mathbf{o}_4$," *Phys. Rev. Lett.*, vol. 108, p. 037206, Jan 2012.

[116] R. D. King-Smith and D. Vanderbilt, "Theory of polarization of crystalline solids," *Phys. Rev. B*, vol. 47, pp. 1651–1654, Jan 1993.

[117] Y. S. Oh, S. Artyukhin, J. J. Yang, V. Zapf, J. W. Kim, D. Vanderbilt, and S.-W. Cheong, "Non-hysteretic colossal magnetoelectricity in a collinear antiferromagnet," *NATURE COMMUNICATIONS*, vol. 5, JAN 2014.

[118] T. Kurumaji, S. Ishiwata, and Y. Tokura, "Doping-tunable ferrimagnetic phase with large linear magnetoelectric effect in a polar magnet $fe_2mo_3o_8$," *Phys. Rev. X*, vol. 5, p. 031034, Sep 2015.

[119] S. Nakayama, R. Nakamura, M. Akaki, D. Akahoshi, and H. Kuwahara, "Ferromagnetic behavior of (fe1-yzny)2mo3o8 (0y1) induced by nonmagnetic zn substitution," *Journal of the Physical Society of Japan*, vol. 80, no. 10, p. 104706, 2011.

[120] T. Kurumaji, S. Ishiwata, and Y. Tokura, "Diagonal magnetoelectric susceptibility and effect of fe doping in the polar ferrimagnet $Mn_2Mo_3o_8$," *Phys. Rev. B*, vol. 95, p. 045142, Jan 2017.

[121] B. Gao, F.-T. Huang, Y. Wang, J.-W. Kim, L. Wang, S.-J. Lim, and S.-W. Cheong, "Interrelation between domain structures and polarization switching in hybrid improper ferroelectric ca3(mn,ti)2o7," *Applied Physics Letters*, vol. 110, no. 22, p. 222906, 2017.

[122] P. K. S. Blaha, K. Schwarz, G. Madsen, D. Kvasnicka, and J. Luitz, "Wien2k: An augmented plane wave plus local orbitals program for calculating crystal properties," vol. 28, 01 2001.

[123] W. Kohn and L. J. Sham, "Self-consistent equations including exchange and correlation effects," *Phys. Rev.*, vol. 140, pp. A1133–A1138, Nov 1965.

[124] P. Hohenberg and W. Kohn, "Inhomogeneous electron gas," *Phys. Rev.*, vol. 136, pp. B864–B871, Nov 1964.

[125] J. P. Perdew, K. Burke, and M. Ernzerhof, "Generalized gradient approximation made simple," *Phys. Rev. Lett.*, vol. 77, pp. 3865–3868, Oct 1996.

[126] J. P. Perdew, K. Burke, and M. Ernzerhof, "Generalized gradient approximation made simple [phys. rev. lett. 77, 3865 (1996)]," *Phys. Rev. Lett.*, vol. 78, pp. 1396–1396, Feb 1997.

[127] V. I. Anisimov, I. V. Solovyev, M. A. Korotin, M. T. Czyżyk, and G. A. Sawatzky, "Density-functional theory and nio photoemission spectra," *Phys. Rev. B*, vol. 48, pp. 16929–16934, Dec 1993.